Stress Effects on Atomistic Kinetic Transitions

by

Sabrina Lillian Ball

B.S. Mechanical Engineering, University of Arizona (2014)

Submitted to the Department of Mechanical Engineering
in partial fulfillment of the requirements for the degree of

Master of Science in Mechanical Engineering

at the

MASSACHUSETTS INSTITUTE OF TECHNOLOGY

June 2016

Author .....
Department of Mechanical Engineering
May 20, 2016

Certified by .....
Christopher Schuh
Danae and Vasilis Salapatas Professor of Metallurgy
Thesis Supervisor

Certified by .....
Ken Kamrin
Assistant Professor
Thesis Supervisor

Accepted by .....
Rohan Abeyaratne
Chairman, Committee on Graduate Students

Stress Effects on Atomistic Kinetic Transitions

by

Sabrina Lillian Ball

Submitted to the Department of Mechanical Engineering
on May 20, 2016, in partial fulfillment of the
requirements for the degree of
Master of Science in Mechanical Engineering

Abstract

In this thesis, I studied how the full tensorial stress state applied to a kinetic transition impacts the activation enthalpy. To this end, the activation energy, scalar activation volume, and tensorial activation volume were studied for several kinetic transition types. This computational study used the nudged elastic band method to find the activation state for initial and final configurations known a priori, primarily from the kinetic activation relaxation technique. The preliminary work was verified by a commonly studied and well understood vacancy generation and migration to an adjacent lattice cite in FCC copper and HCP titanium. The method was then applied to transitions of increasing complexity: point defect generation in a perfect copper crystal, and grain boundary transitions in the Σ 5 [210] grain boundary in copper.

Thesis Supervisor: Christopher Schuh
Title: Danae and Vasilis Salapatas Professor of Metallurgy

Thesis Supervisor: Ken Kamrin
Title: Assistant Professor

Acknowledgments

There are many people who have shaped my existence and experience here at MIT, for whom I am eternally grateful. I would like to start off by thanking my advisor Christopher Schuh his guidance and for teaching me how to navigate research in order to reach a better understanding and gaining new perspectives in solving problems. Though, Chris wasn't the only one in my research group who had a key role in my success. I am especially grateful for Kathleen Alexander. Her guidance and collaboration was invaluable and without her role, this thesis would likely not exist. I am also thankful for Arvind, Thomas, and the rest of the Schuh group, whose discussions and insight were invaluable to my understanding of materials science as a whole.

I would also like to thank my parents for emphasizing the importance of hard work and commitment. You always told me I could do whatever it is that I wanted. Well, I wanted to be a pokemon gym leader, but since pokemon aren't real I guess I had to settle for a Master Ball. [1] I am also thankful for my siblings Alexis and Cyd. These two have been keeping me balanced and humble for nearly 25 years (and are my primary source of pokemon knowledge). I am eternally grateful to have Alex for consistently reminding me that I am capable of anything (shy of reaching things on the top shelf without a step stool). Last, but certainly not least, I would like to thank my friends and teammates on the MIT Hyperloop team for their continual support and encouragement. We worked hard together, we played hard together, and we found a decent taco restaurant in Cambridge. If that is not what life is about, then I don't know what is.

[1] For those unfamiliar with the pokemon universe, a master ball one of the rarest pokeballs of the first generation, which guarantees the capture of a wild pokemon

Contents

List of Figures

List of Tables

Chapter 1

Introduction

Whether it is a 40 ft steel beam holding up the fiftieth floor of a high rise building or a 40 micron gear in a microelectromechanical device, nearly all materials experience stress in their final application. Applied stress affects materials in many ways; it stretches atomic bonds in the elastic regime, creates and drives dislocations motion in the plastic regime, and may lead to complete failure when the fracture strength is exceeded. Stress also affects material properties like diffusion and electric conductivity.

This work will explore the effect that an applied stress state has on kinetic transitions. I will start this work by motivating the project with the necessary background information on kinetic transitions and grain boundaries in chapters one and two, respectively. Chapter three outlines the methods for determining kinetic events, activation energy, activation volume scalars, and activation volume tensors. Chapters four through seven are case studies on different systems in order of increasing complexity from a simple vacancy migration to transitions in the Σ 5 [210] grain boundary.

1.1 Kinetics

The field of kinetics focuses on the rate at which transformations or reactions in a material or chemical process occur. A kinetic event is the progression of a system of atoms from one metastable state to an adjacent metastable state. This work will use the terms reaction, kinetic event, and kinetic transition interchangeably.

1.2 Activation Free Energy Barrier

The activation free energy barrier, G*, of a kinetic event is the energy required to get from one atomic configuration to another. It is essentially the barrier between two metastable atomic states and is important to the field of kinetics because it determines how often a kinetic event is to occur. The Arrhenius equation, equation 1.1, is one of the most fundamental equations in kinetics; it describes the temperature dependence of reaction rates. [1]

$$k = A_0 e^{-\frac{G^*}{k_B T}} \tag{1.1}$$

In this equation, k is the rate constant, A_0 is the pre-exponential factor, G* is the activation free energy barrier, k_B is the Boltzmann constant, and T is the temperature in absolute degrees.

The activation free energy barrier is a difference in the Gibbs free energy of the system in the initial and activated states as shown in figure 1-1. The Gibbs free energy is the sum of the enthalphy and the entropy of a state as shown by equation 1.2.

$$G = H - TS \tag{1.2}$$

Where H is the enthalpy given by:

$$H = E + pV \tag{1.3}$$

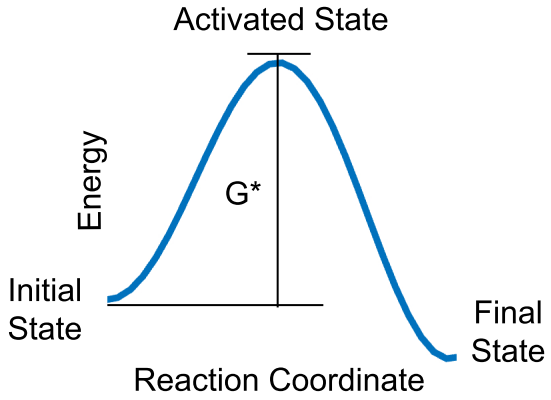

Figure 1-1: Activation Free Energy Barier

and S is the entropy, E is the internal energy, p is pressure, and V is volume.

The activation free energy barrier, G*, is the similarly defined as:

$$G^* = E^* + pV^* - TS^* \tag{1.4}$$

where E* is the activation energy, V* is the activation volume, and S* is the activation entropy.

In many studies of kinetics in metals, researchers assume that the contribution from the pV^* term in this equation is significantly smaller than the internal activation energy term, and the activation enthalpy is roughly equivalent to the activation energy [2, 3]:

$$H^* \approx E^* \tag{1.5}$$

1.3 Activation Energy

The activation energy is the energy required to go from one metastable state to another under zero applied pressure and at absolute zero temperature. The energy landscape is a mapping of the available metastable states accessable to a given initial state. Figure 1-2 shows a three-dimensional representation of an energy landscape.

The metastable states reside in the wells of the energy landscape as shown by the blue stars, and the saddle point along the purple line between them represents the activation energy.

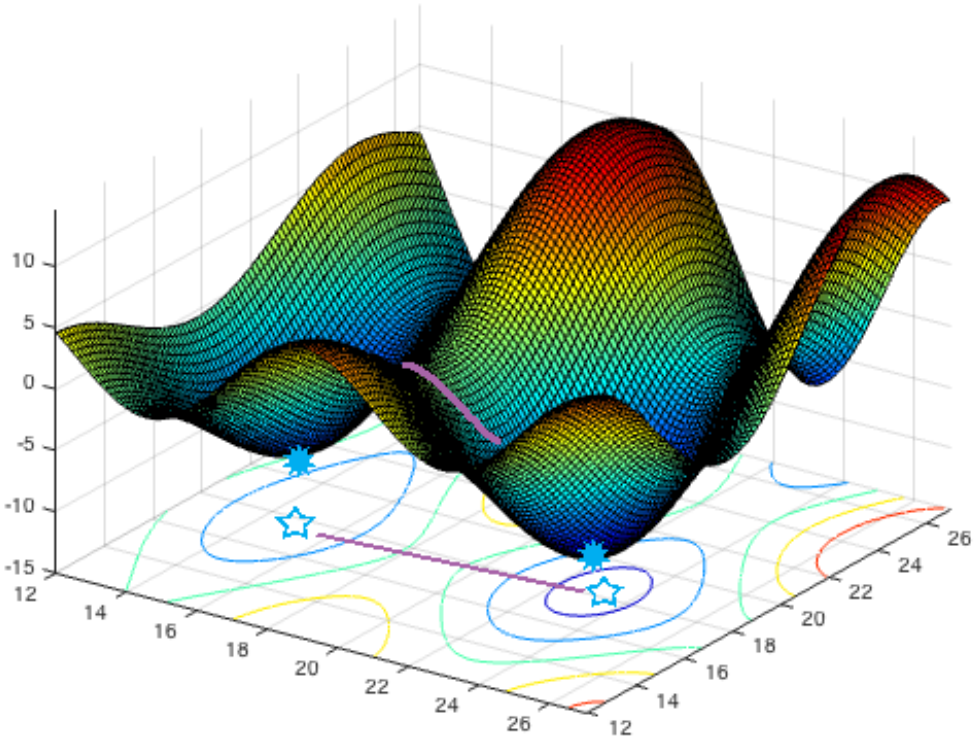

Figure 1-2: Activation Energy Landscape Contour

The activation energy can be measured experimentally from a rearrangement of the rate equation, 1.1, which can be rewritten as:

$$ln(k) = ln(A_0) - G^*(\frac{1}{k_B T}) \tag{1.6}$$

By experimentally measuring the rate at varying temperatures, the activation energy can be calculated on an Arrhenius plot from the slope of the plot of $ln(k)$ versus $\frac{1}{T}$

1.4 Activation Volume Scalar

The activation volume scalar is a single value which describes the overall dilation of a system between the initial and saddle point states during a kinetic transition. This value is commonly reported in terms of the atomic volume, Ω_0, of the material. It is an important value in kinetics because it describes the sensitivity of the activation enthalpy to a hydrostatic stress state. [4, 5, 6, 7]

Mathematically, it can be determined as the change in the activation energy of the system, E*, with a change in the hydrostatic applied pressure, P, at 0° Kelvin, as shown in equation 1.7.

$$V^* = \left.\frac{\partial E^*}{\partial P}\right|_{T=0} \tag{1.7}$$

Experimentally, the activation volume scalar, V*, for diffusion processes is determined by the pressure dependence of the diffusion coefficient at a constant temperature. This method is detailed explicitly by Mehrer et al. in the *Diffusion in Solids*, but is briefly summarized as: [2]

$$V^* = -k_B T\left(\frac{\partial ln D}{\partial P}\right)_T + \underbrace{k_B T\frac{\partial ln(fa^2\nu^0)}{\partial P}}_{correction} \tag{1.8}$$

where the first term on the right is the slope of the line of the logarithm of the diffusion coefficient with respect to the pressure, P, and the second term on the right is a correction term that can be estimated by the isothermal compressibility, κ_T, and the Gruneisen constant, γ_G as

$$correction \approx k_B T \kappa_T \gamma_G \tag{1.9}$$

The activation volume scalar is not experimentally calculated for other types of kinetic events than those found in diffusion. This is likely due to complexities in categorizing and measuring individual kinetic transitions in a bulk experimental sample.

Computationally, however, the activation volume scalar is easily measured by the change in the activation energy of a kinetic event with respect to an applied hydrostatic pressure. This can be done by calculating the activation energy at several magnitudes of hydrostatic applied stress and measuring the slope of the energy, E*, versus pressure, P, curve as described in further detail in section 3.3.

1.5 Activation Volume Tensor

The activation volume scalar, V*, is an oversimplification of the stress dependent behavior of a kinetic event. This value is only valid for a hydrostatic applied stress state. In most operating conditions, the atomic configuration in a bulk solid is not subjected to a hydrostatic state of stress and is instead subject to a 3-dimensional stress state that can be represented by a second rank tensor, $\bar{\sigma}$

$$\bar{\sigma} = \begin{pmatrix} \sigma_{11} & \sigma_{12} & \sigma_{13} \\ \sigma_{21} & \sigma_{22} & \sigma_{23} \\ \sigma_{31} & \sigma_{32} & \sigma_{33} \end{pmatrix} \tag{1.10}$$

Therefore, a symmetric, second order tensor is required to represent the stress sensitivity of the enthalpy to this 3-dimensional stress state, the activation volume tensor. Each term, Ω_{ij}, represents a strain value between the initial and saddle point states. The diagonal terms ($i = j$) represent the dilation between the two states for the three coordinate directions of the simulation cell. The off diagonal terms ($i \neq j$) represent the shearing between the initial and saddle point states. It should be noted that this is also commonly referred to as the activation strain tensor in the literature.

$$\overline{\Omega} = \left. \frac{\partial E^*}{\partial \bar{\sigma}} \right|_{T=0} \tag{1.11}$$

where $\overline{\Omega^*}$ is the activation volume tensor given by:

$$\overline{\Omega} = \begin{pmatrix} \Omega_{11} & \Omega_{12} & \Omega_{13} \\ \Omega_{12} & \Omega_{22} & \Omega_{23} \\ \Omega_{13} & \Omega_{23} & \Omega_{33} \end{pmatrix} \tag{1.12}$$

Currently, there are no known works that study the activation volume tensor experimentally. However, there are several works which study the tensor computationally. [8, 9, 10, 11, 12] Many of these works focus on calculating the activation volume tensor by directly measuring the strain between the atoms in the initial and saddle point configurations; this will be referred to as the strain measurement method.

Chapter 2

Motivation: Applications to Grain Boundary Engineering

2.1 Grain Boundaries

Grain boundaries (GBs) are interfaces between pairs of crystal grains in a polycrystalline material. These interfaces exhibit different energetics and properties as compared to the bulk material, and as such grain boundaries play a significant role in the mechanical, thermal, and electrical properties of many metal and ceramic materials. Intergranular corrosion, embrittlement, and creep are highly dependent on grain boundary diffusion characteristics [13, 14, 15, 16, 17, 18, 19]. In addition, grain boundaries play a significant role in plasticity as barriers for dislocation movement [20, 21].

2.1.1 Grain Boundary Structure and Orientation Space

The structure of grain boundaries has been studied extensively. [22, 23] Most works classify grain boundaries into two sub-categories: low angle and high angle. Low

angle grain boundaries are boundaries where the misorientation angle between the two grains is small. These GBs are often modeled as arrays of nearby screw or edge dislocations. [1, 19, 24] High-angle grain boundaries are classified as boundaries in which the misorientation from coincidence is greater than 15 degrees [25] Beyond this critical angle, the dislocation arrays making up these boundaries overlap. [1] These general grain boundaries display a wide range of energies and properties [26]

The grain boundary orientation space is a vast field that can be described by five macroscopic degrees of freedom (DOF). In the coincident site lattice (CSL) terminology which is adopted in this work, three DOFs are defined by the CSL rotation, and two DOFs are defined by the grain boundary plane. In the interface plane method, there are four DOFs to describe the grain boundary plane normals and one DOF to describe the angle of rotation [27, 28].

In the CSL notation, the sigma value, Σ, represents the reciprocal of the density of coincident sites in the grain boundary. Small sigma values correspond to high densities of coincidence [22]. CSL boundaries are often categorized as "special" GBs. "Special" boundaries are a unique category of grain boundaries consisting primarily of low angle and CSL boundaries. It was broadly defined by Randle as "an interface with at least one low-index boundary plane forming its surface" [28] This category of grain boundaries is not self-consistent within the literature, categorized by geometric considerations at times and by properties at others. [29, 30]

2.2 Motivation: What is Grain Boundary Engineering?

Materials science and engineering is a field dedicated to understanding the ties between microstructures, processing, and properties. Within this broad field of study lies the smaller field of grain boundary engineering (GBE). Grain boundary engineer-

ing focuses on controlling the populations of grain boundaries within a polycrystalline material in order to optimize material characteristics. In order to strategically design the grain boundary networks within a material, engineers require a proper understanding of the nature of grain boundaries and grain boundary transitions. This work aims to contribute to the field of grain boundary engineering in two key ways. The first goal is to improve the computational methods of studying grain boundaries by providing an improved understanding of how grain boundary transitions are affected by an applied stress state. With a more accurate representation of grain boundary kinetics, improved models of the grain boundary energy landscape can be used to study grain boundary behavior at physically realizable time scales using kinetic Monte Carlo methods. The second way this work may contribute to the field of GBE is in implementation of grain boundary engineering in practice. By understanding how the activation energy changes in response to an external stress state, engineers will have a better understanding of how to drive grain boundary kinetic transitions during materials processing.

2.2.1 Experimental Studies in GBE

Grain boundary engineering is a method of controlling a microstructure by increasing the population of "special" grain boundaries. This empirically driven field has led to order of magnitude improvements in grain boundary controlled properties including corrosion resistance, creep resistance, strength, and ductility.[16, 31, 32] Grain boundary engineering as we know it today began in the late 1980's with improvements to the corrosion resistance of nickel-based superalloys. In the 1990's thermo-mechanical processing techniques were developed which increased the proportion of low-CSL boundaries within FCC metals with low stacking fault energies.[28] The following decade had many studies on the connectivity of grain boundary networks. [33, 34, 35]

2.2.2 Computational Studies in GBE

There have been a number of computational studies on grain boundaries in order to improve the fundamental understanding of grain boundary engineering. Recent work out of Sandia National labs by Olmstead et al. consisted of the computational survey of 388 distinct grain topologies. This work focused on the grain boundary energy, grain boundary plane geometry, i.e. free volume and CSL value,[26] and grain boundary mobility [36] Extensive studies have also been performed investigating the grain boundary mobility [37, 38, 39, 40]. Understanding how applied stress influences grain boundary kinetices is an important factor in these mobility studies. [41] Very high driving forces are commonly applied to the grain boundaries. Many in the field cannot agree on the validity of these studies since they do not reproduce experimental data.

2.3 Stress Effects on Kinetic Transitions

One of the final goals of this research project was to gain insight into how the stress state within a polycrystalline material affects the activation energy for grain boundary evolution. This work is essential to understanding grain boundary migration at the high stress states seen in material processing and at materials used in very high stress states.

Chapter 3

Methods

This work focused on developing methods for determining the activation parameters for any arbitrary kinetic transition. It combines the activation relaxation technique (ART) as developed by Alexander et al. [42], the nudged elastic band method (NEB), and the weighted least squares approach to find the activation energy, E*, activation volume scalar, V*, activation volume tensor, $\overline{\Omega^*}$, and the second invariant of the activation volume, Λ.

3.1 Finding Kinetic Transitions

In order to use the nudged elastic band method (NEB), the initial and final atomic configurations of a transition must be known a priori. In this work there were two methods for finding the initial and final states. For the vacancy migration studies, the configurations were developed using LAMMPS built in functions, as shown in appendix C. With the more complicated point defects and grain boundary transitions, the final state of the kinetic transition was determined using the activation relaxation technique (ART). [43]

3.1.1 Vacancy Migration in LAMMPS

For the vacancy migration studies in FCC copper and HCP titanium, the initial and final states were created using the region, delete_atoms, and displace_atoms commands in LAMMPS. [44] In order to maintain consistent atom numbering between the configurations, the final state was first generated by removing an atom at an adjacent site to the atom located at the origin of the simulation cell. The system was relaxed using the conjugate gradient method. This file is stored as the final configuration and the atom at the origin is relocated to the vacant site using the displace_atoms command, effectively creating a vacancy at the origin of the simulation cell. This system is also relaxed using the conjugate gradient method.

3.1.2 Transitions using the Activation Relaxation Technique

ART is an eigenvector following method that can be used to map the saddle points and adjacent minima on the energy landscape of an atomic configuration. Thus, it can be used to catalog the kinetic events that a system can undergo when only an initial configuration is known. [42, 45] Starting from an energy minimized initial configuration, our implementation of ART searches the energy landscape for saddle points by systematically perturbing unique atoms in the starting configuration. Each systematic perturbation results in a configuration that is no longer in the minimum energy basin of the potential energy surface (PES). If the system is in a region of the PES with one negative curvature, then ART iteratively pushes the system in the direction corresponding to the negative curvature and relaxes the system in the hyperplane of this curvature. The method continues to evolve the system in this fashion until either a saddle point is found, the system falls back into a potential energy basin, or the maximum allowed number of convergence steps is exceeded. If a saddle point is successfully found, the system at the saddle point configuration is then relaxed away from the initial minimum structure using a conjugate gradient minimization scheme until an adjacent minimum structure is found.

In this implementation of ART, atoms in the initial structure are deemed to be unique based on the location of their nearest neighbors. The systematic perturbations that each atom is subjected to correspond to the directions of a 156 point uniform spherical mesh superimposed on concentric spheres centered on the target atom, with radii ranging from 0.75 to 2.25 Å. Kinetic events are then determined to be unique according to the displacements of each atom during the kinetic process.

Though ART allows us to investigate kinetic processes given only an initial configuration, it is not constrained to finding only minimum energy saddle points and is capable of finding high energy pathways on the energy landscape. Additionally, because the trajectory followed in the search for the saddle point follows a numerical search process, only the saddle points and adjacent minimum configurations found with this method, rather than the specific motions of the atoms during the search process, are physically meaningful. [42]

3.2 Activation Energy Using the Nudged Elastic Band Method (NEB)

ART is an effective method for determining the accessible atomic configurations for a given initial state; however it is not constrained to the minimum energy pathway between the configurations. The activation energy determined by the ART is not consistently physical under an applied stress state. Therefore, the nudged elastic band method (NEB) is used to calculate the activation energy in this work. Additionally, preliminary studies performed by K. Alexander showed that the ART method does not properly capture the behavior of kinetic events under hydrostatic applied loads; it produces a parabolic curve of activation energy versus pressures, centered about the zero-pressure state. Figure 3-1 shows the activation energy as calculated by ART vs NEB for grain boundary transitions and for localized point defects generated in a perfect copper crystal. Values above the solid line are those for which the ART

method over estimates the activation energy.

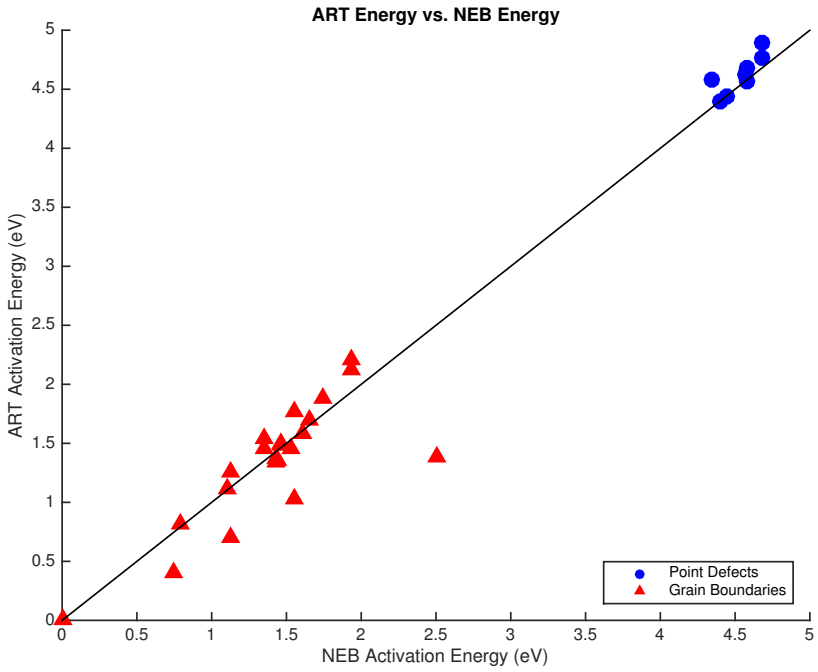

Figure 3-1: Activation energy calculated by activation relaxation technique (ART) vs nudged elastic band (NEB) on grain boundary kinetic events and localized point defect generation

3.2.1 What is NEB?

The nudged elastic band (NEB) method is a constrained method for finding the saddle point energy of a kinetic process given both an initial and a final atomic configuration. Given these end states as inputs, NEB breaks up the reaction coordinate into a series of snapshots, called replicas, through linear interpolation of the atomic positions at the initial and final states of the process. [46, 47]

Minimization occurs in a two-stage process. First, a spring-force is applied between these replicas tangentially to keep them evenly distributed along the reaction coordinate. The true force is the gradient of the energy function with respect to position and acts perpendicular to the spring force. The atoms in each replica are then relaxed using a conjugate gradient approach modified by the spring-force connecting

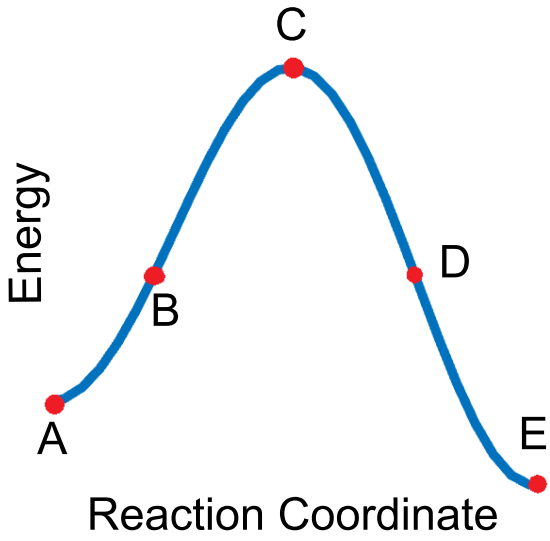

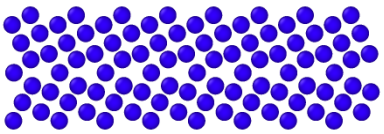

(a) A

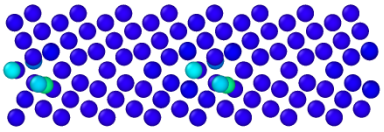

(b) B

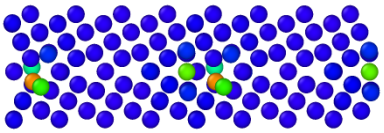

(c) C

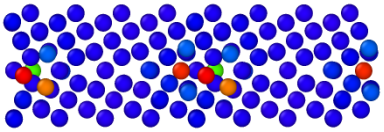

(d) D

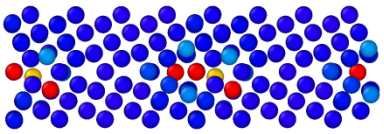

(e) E

Figure 3-2: Nudged elastic band replicas as shown by a kinetic event in the Σ5[210] grain boundary colored based on atomic displacement

the replicas, which effectively drives the band to the minimum energy path. Then the spring-force is replaced by a function of the energy gradient for the saddle point replica and the system is minimized with a damped dynamics routine. [48, 49]

3.2.2 Implementation of NEB

This work uses the NEB method as implemented in LAMMPS [44]. Preliminary studies were performed using the hydrostatic stress state on grain boundary transitions in copper in order to find adequate NEB settings. For all kinetic events, the quickmin minimizer was used, with a time step of 0.01 ps, a band spring constant of 5, a convergence energy threshold of 1.0x 10^{-15} eV, a convergence force threshold of 5.0x10^{-9} eV/Å. The number of replicas was dependent on the transition complexity. This work used 8 replicas for the vacancy migration studies, 12 replicas for the local defects, and 20 to 24 replicas for the Σ 5 [210] grain boundary transitions. The maximum allowable iterations also varied with system complexity, with values ranging from 150,000 to 500,000 for the simple transitions and grain boundary transitions, respectively. These system variables were determined by doing sweeps of each parameter individually and selecting the least computationally intensive value.

3.3 Activation Volume Scalar

As described in 1.4, the activation scalar, V*, is a singular value which describes the overall dilation between an initial atomic configuration and the saddle point configuration for a given kinetic event. It is useful in understanding the effect which a hydrostatic stress state has on the kinetics of a given reaction.

The diagram in figure 3-3 shows the general workflow for determining the scalar activation volume for a given kinetic transition. First, the initial and final state atomic configurations must be determined from the methods in section 3.1. Then, a hydro-

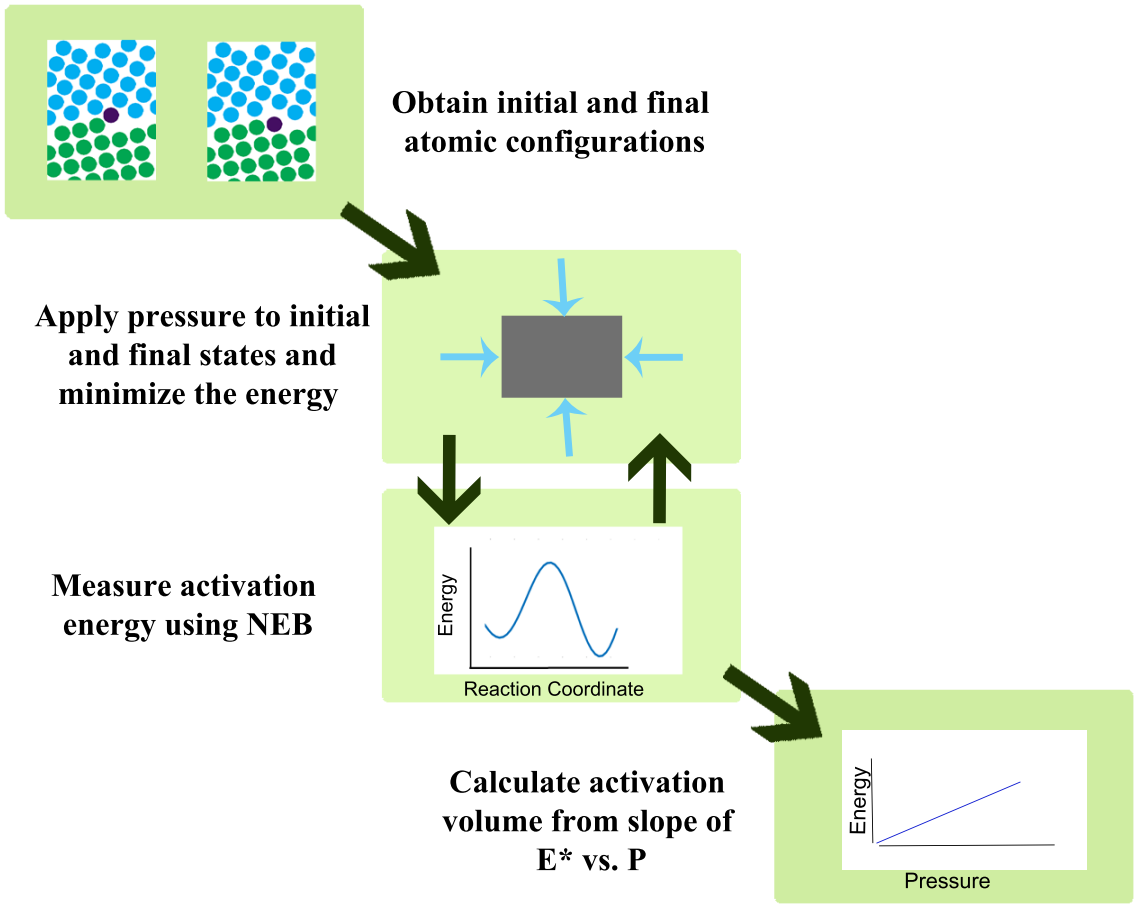

Figure 3-3: Activation Volume Scalar Determination Process

static pressure is applied to these two configurations, and the atoms are relaxed to the lowest energy state. The activation energy is then determined using NEB. The pressure and energy steps are repeated for a set number of pressure magnitudes. Finally, the activation volume scalar, V^* is calculated using a least squares regression analysis from the slope of the activation energy with respect to pressure magnitude.

3.3.1 Implementation

The activation volume scalar is determined by applying a hydrostatic stress state to the initial and final atomic configurations using the fix box/relax command with the iso keyword for an isostatic stress state, with $\sigma_{xx} = \sigma_{yy} = \sigma_{zz} = P$, and the shear terms equal to zero, $\sigma_{xy} = \sigma_{xz} = \sigma_{yz} = 0$.

Under each applied hydrostatic pressure, P, the energy of the system was relaxed to its minimum energy state using a conjugate gradient method, with an additional energetic term associated with this applied pressure. This process was repeated for different magnitudes of hydrostatic pressure. It should be noted that in the LAMMPS convention of stress, negative values of pressure correspond with tensile loading; whereas positive values correspond to compression. The applied values of hydrostatic pressure ranged from 5000 bar in tension to 5000 bar in compression.

Initial studies were performed using a high sampling density, with pressure increments of 100 to 250 bar over the entire pressure regime. It was soon determined that this high sampling rate was not necessary to adequately measure the activation volume. The optimal sampling rate was determined to be 1000 bar increments over the entire pressure regime, in order to reduce the computational load, while still capturing the behavior of the kinetic transition under load.

3.3.2 Calculation and Uncertainty

As stated in section 1.4, the activation volume of a given transition is given by equation 1.7.

$$V^* = \left.\frac{\partial E^*}{\partial P}\right|_{T=0}$$

In this work, it is determined by the slope of the activation energy, E*, with respect to the hydrostatic pressure, P, as shown by figure 3-4, using a linear least squares regression analysis as shown in equation 3.1, where n is equal to the number of pressure magnitudes measured.

$$V^* = \frac{(\Sigma E^*)(\Sigma P^2) - (\Sigma P)(\Sigma E^* P)}{n(\Sigma P^2) - \Sigma(P^2)} \tag{3.1}$$

There is always some amount of uncertainty when calculating a given quantity. This uncertainty must be known in order to understand the validity of the calculation.

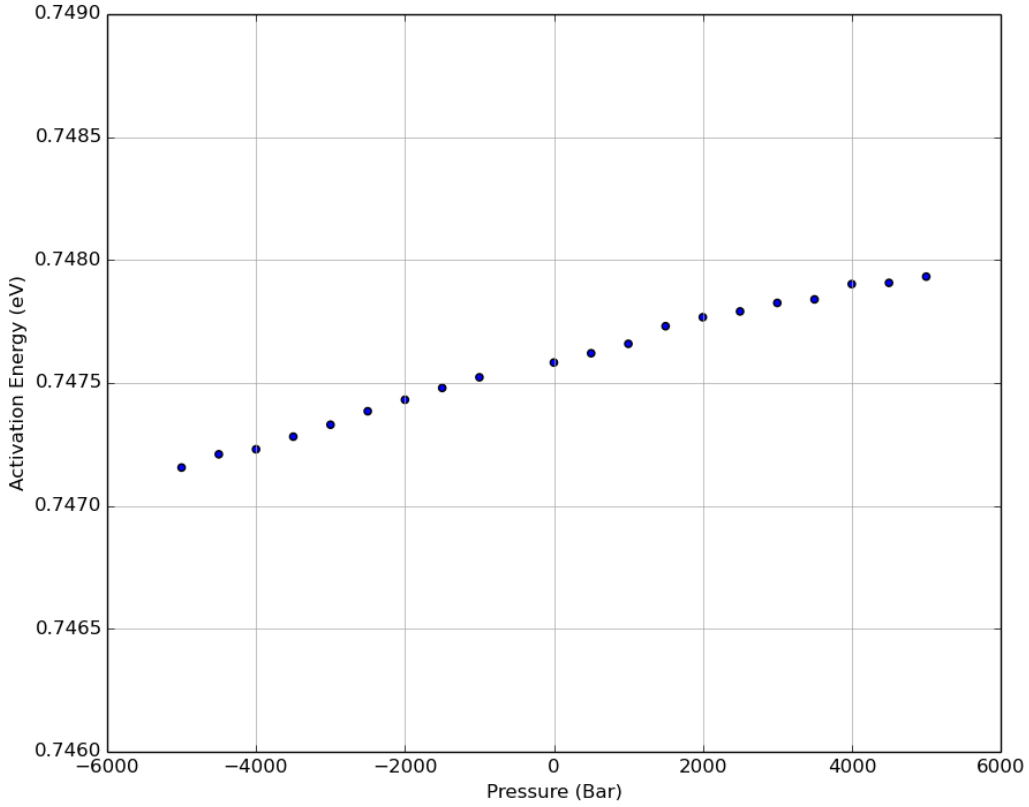

Figure 3-4: Activation Energy vs. Hydrostatic Pressure in a Copper Vacancy Migration

The uncertainty in the slope of the line can be determined by equation 3.2

$$S_{V^*} = \sqrt{\frac{\frac{\Sigma(E_i^* - \hat{E^*}_i)^2}{n-2}}{\Sigma(P_i - \bar{P})^2}} \tag{3.2}$$

The confidence interval for the activation volume from the uncertainty in the slope can be obtained by multiplying the uncertainty, S_{V^*}, with the Students t-value for the given degrees of freedom, n-2, for a ninety percent confidence interval as shown in equation 3.3

$$\epsilon_{slope} = t_{90} S_{V^*} \tag{3.3}$$

In addition to this uncertainty, the uncertainty from the numerical error associated with the cutoff energy, $\mathcal{E}$, during convergence as shown in equation 3.4 is

$$\epsilon_{num} = \frac{\mathcal{E}}{E^*} V^* \tag{3.4}$$

These errors can be combined by equation 3.5

$$\epsilon_{total} = \sqrt{(\epsilon_{slope})^2 + (\epsilon_{num})^2} \tag{3.5}$$

This total error defines the upper and lower bounds of the activation volume.

3.4 Activation Volume Tensor

As stated previously, the activation volume tensor shows the effect any arbitrary stress state has on the activation enthalpy for a given reaction, as shown by 1.3. It is also a measurement of how the atomic configuration changes between the initial and saddle point of the kinetic event. [10] The method of calculating the activation volume tensor is very similar to that which is used in determining the activation volume scalar. Figure 3-5 shows the steps of this process.

3.4.1 Implementation

In order to calculate the activation volume tensor, $\overline{\Omega}$, several directional measurements of activation energy versus pressure are required. To this end, an array of evenly distributed directions is generated, equivalently populating half of a unit sphere. This hemisphere, in the positive z-direction, has been populated using two distinct methods. The first is a discrete value method, where integer values from one to five are selected in the x, y, and z directions, these integer values are then normalized. This method has the drawback of unevenly sampling the region of low angular displacement from the xz and yz planes, as shown in figure 3-6 The second method, developed by Rusin [50] generates a given number of evenly dispersed directions around the positive

Figure 3-5: Activation Volume Tensor Determination Process

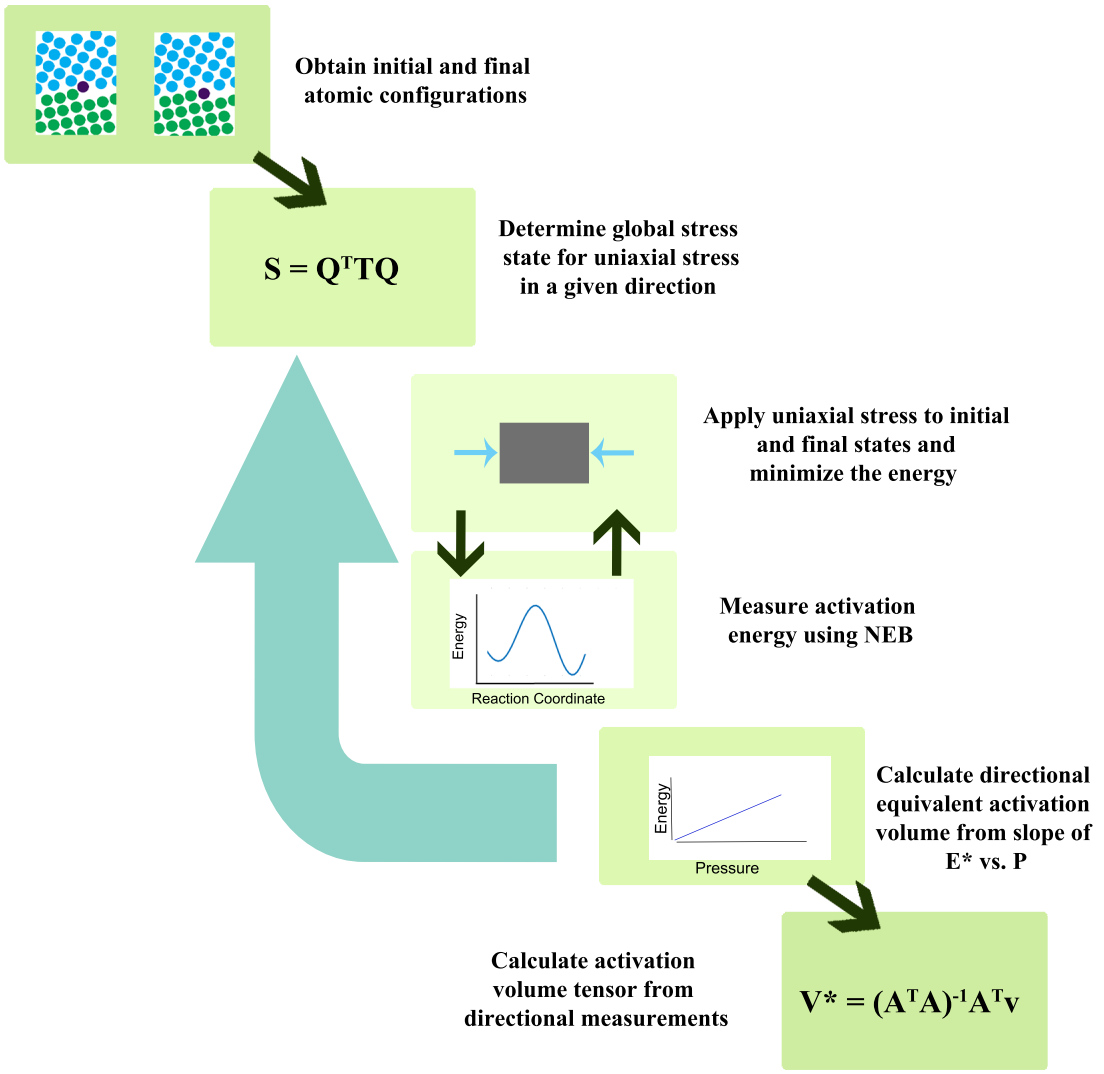

z-hemisphere of directional unit space. As seen in figure 3-7, the density of direction normals is evenly distributed about the space.

Once the array of directions is found, the uniaxial load in each direction must be converted into an equivalent stress state within the coordinates of the system cell. In order to do this, the stress state is converted into uniaxial stress, $\bar{T}$, in the local

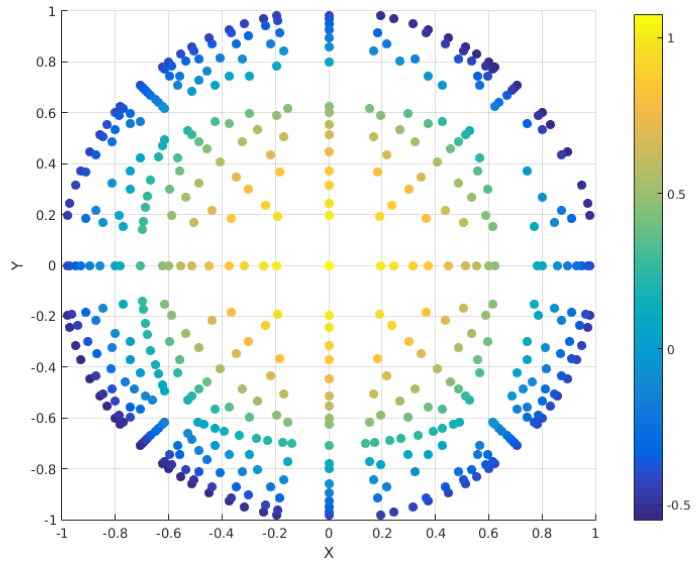

Figure 3-6: Uniaxial Load Direction Normals for Integer Method

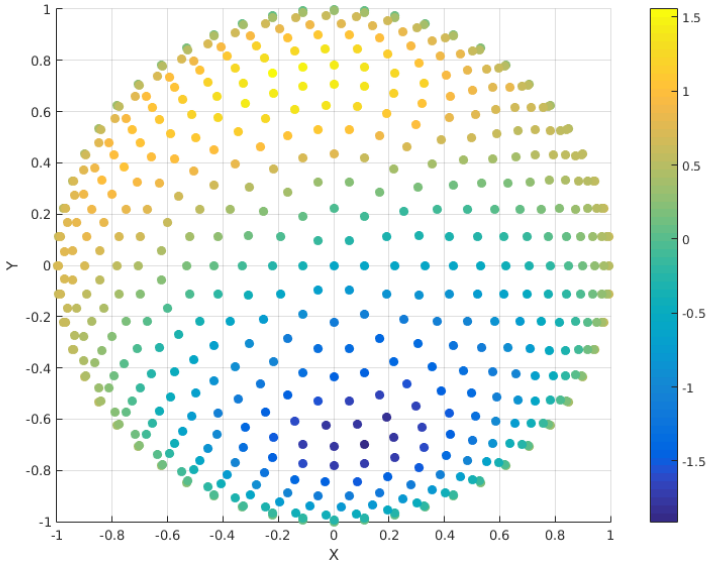

Figure 3-7: Uniaxial Load Direction Normals for Evenly Distributed Method

coordinate frame.

$$\bar{T} = \begin{pmatrix} P & 0 & 0 \\ 0 & 0 & 0 \\ 0 & 0 & 0 \end{pmatrix} \tag{3.6}$$

The normalized direction that this uniaxial stress in the global frame of the simulation cell is $\vec{l}$

$$\vec{l} = \begin{pmatrix} l_x & l_y & l_z \end{pmatrix} \tag{3.7}$$

This local stress state can be transformed into the global reference frame stress state $\bar{S}$ from the direction cosine matrix, $\bar{Q}$ using equation 3.9. [51]

$$\bar{Q} = \begin{pmatrix} l_x & 0 & l_y^2 - l_z^2 \\ l_y & l_z & -l_x l_y \\ l_z & l_y & l_x l_z \end{pmatrix} \tag{3.8}$$

$$\bar{S} = \bar{Q}\bar{T}\bar{Q}^T \tag{3.9}$$

$$S = \begin{pmatrix} l_x & 0 & l_y^2 - l_z^2 \\ l_y & l_z & -l_x l_y \\ l_z & l_y & l_x l_z \end{pmatrix} \begin{pmatrix} P & 0 & 0 \\ 0 & 0 & 0 \\ 0 & 0 & 0 \end{pmatrix} \begin{pmatrix} l_x & l_y & l_z \\ 0 & l_z & l_y \\ l_y^2 - l_z^2 & -l_x l_y & l_x l_z \end{pmatrix} = \begin{pmatrix} l_x^2 & l_x l_y & l_x l_z \\ l_x l_y & l_y^2 & l_y l_z \\ l_x l_z & l_y l_z & l_z^2 \end{pmatrix} P$$

The global stress matrix, S, can be applied to the target system using the LAMMPS box/relax fix during static minimization where P is is the stress magnitude in bar.

Next, we find the directional activation volume scalar, v', in the given uniaxial direction $\vec{l}$ by taking the partial derivative of the activation energy, E*, with respect to the magnitude of the uniaxial stress using equation 3.1, where P is now the magnitude of the uniaxial stress in the given direction.

3.4.2 Calculation and Uncertainty

This work uses the weighted least squares regression analysis to calculate the activation volume tensor, $\overline{\Omega}$, from the directional activation volume scalar, $\vec{v'}$. The weighted least squares method is preferred over the ordinary least squared method commonly used to measure tensorial properties [51] because it allows for the quantification of error in the activation volume tensor. In this section, the mathematical derivation of

this method will be outlined.

Table 3.1 outlines the variables and concepts used in this derivation.

If activation energy calculations and stress state applications were exact, the activation volume tensor could be quantified by six measurements of the activation volume in six directions according to equations 3.10.

$$\vec{v'} = \bar{a}\vec{\Omega} \tag{3.10}$$

Where $\bar{v'}$ is the vector of directional activation volume scalars, $\vec{\Omega}$ is the vector representation of the symmetric activation volume tensor $\bar{\Omega}$, and $\bar{a}$ is a matrix of coefficients calculated from the components of the direction vectors, $\vec{l}$, by:

$$\bar{a} = \begin{pmatrix} l_{1x}^2 & l_{1y}^2 & l_{1z}^2 & 2l_{1y}l_{1z} & 2l_{1x}l_{1z} & 2l_{1x}l_{1y} \\ l_{2x}^2 & l_{2y}^2 & l_{2z}^2 & 2l_{2y}l_{2z} & 2l_{2x}l_{2z} & 2l_{2x}l_{2y} \\ & \vdots & & & \vdots & \\ l_{Nx}^2 & l_{Ny}^2 & l_{Nz}^2 & 2l_{Ny}l_{Nz} & 2l_{Nx}l_{Nz} & 2l_{Nx}l_{Ny} \end{pmatrix} \tag{3.11}$$

However, there are inherent errors associated with the measurements necessary for determining the activation volume tensor. Therefore, instead of solving, 6 equations, one must find a solution that minimizes the error, η, between the measured value and the transformed value of $\vec{\Omega}$ in N given directions.

$$\vec{\eta} = \bar{a}\vec{\Omega} - \vec{v'} \tag{3.12}$$

Equation 3.12 does not take into account the measurement error, $\vec{\epsilon}$; therefore, a weighting matrix,$\bar{W}$ is introduced and the weighted least squares method is used as shown by equation 3.13.

$$\vec{\eta} = \bar{W}\bar{a}\vec{\Omega} - \bar{W}\vec{v'} \tag{3.13}$$

Table 3.1: Activation Volume Tensor Calculation Variables

Variable	Description	Mathematical Representation
N	total number of directional measurements taken	
$\bar{a}$	(N x 6) transformation matrix	$\begin{pmatrix} a_{11} & a_{12} & a_{13} & a_{14} & a_{15} & a_{16} \\ a_{21} & a_{22} & a_{23} & a_{24} & a_{25} & a_{26} \\ & \cdots & & & \cdots & \\ a_{N1} & a_{N2} & a_{N3} & a_{N4} & a_{N5} & a_{N6} \end{pmatrix}$
$\vec{l}$	uniaxial load direction vector	$\begin{pmatrix} l_x l_y l_z \end{pmatrix}$
$\bar{\Omega}$	(3 x 3) activation volume matrix in Voigt notation	$\begin{pmatrix} \Omega_1 & \Omega_6 & \Omega_5 \\ \Omega_6 & \Omega_2 & \Omega_4 \\ \Omega_5 & \Omega_4 & \Omega_3 \end{pmatrix}$
$\vec{\Omega}$	activation volume vector	$\begin{pmatrix} \Omega_1 \\ \Omega_2 \\ \Omega_3 \\ \Omega_4 \\ \Omega_5 \\ \Omega_6 \end{pmatrix}$
$\vec{v'}$	vector of directional activation volume scalars	$\begin{pmatrix} v'_1 \\ v'_2 \\ \vdots \\ v'_N \end{pmatrix}$
$\vec{\epsilon}$	directional activation volume measurement error	$\begin{pmatrix} \epsilon'_1 \\ \epsilon'_2 \\ \vdots \\ \epsilon'_N \end{pmatrix}$
W	(N x N) diagonal error weighting matrix	$\begin{pmatrix} W_1 & 0 & \cdots & 0 \\ 0 & W_2 & \cdots & 0 \\ \vdots & \vdots & \ddots & 0 \\ 0 & 0 & \cdots & W_N \end{pmatrix}$
$\vec{\eta}$	linear least squares error	$\begin{pmatrix} \eta'_1 \\ \eta'_2 \\ \vdots \\ \eta'_N \end{pmatrix}$

Where the weighting matrix is a diagonal matrix whose components are the reciprocals of the errors in the measurement of the slope.

$$W_{ii} = \frac{1}{\epsilon_i} \tag{3.14}$$

$$W_{i \neq j} = 0 \tag{3.15}$$

The vector, $\vec{\Omega}$, is the solution which satisfies min $|\eta|^2$. The error is minimized when

$$\eta_i \frac{d\eta_i}{d\Omega_j} = 0 \tag{3.16}$$

taking the derivative of equation 3.13,

$$\frac{d\eta_i}{d\Omega_j} = W_{ii} a_{ij} \tag{3.17}$$

3.13 and 3.17 into 3.16 provides

$$(W_{ii} a_{ik} \Omega_k - W_{ii} v_i') W_{ii} a_{ij} = 0 \tag{3.18}$$

which can be rewritten in matrix notation as

$$(\bar{W}\bar{a}\vec{\Omega} - \bar{W}\vec{v'})(\bar{W}\bar{a}) = 0 \tag{3.19}$$

furthermore,

$$(\bar{W}\bar{a})^T(\bar{W}\bar{a}\vec{\Omega} - \bar{W}\vec{v'}) = 0 \tag{3.20}$$

expanding these terms

$$(\bar{W}\bar{a})^T\bar{W}\bar{a}\vec{\Omega} - (\bar{W}\bar{a})^T\bar{W}\vec{v'} = 0 \tag{3.21}$$

bringing the $\vec{v'}$ term to the other side and distributing the transpose

$$\bar{a}^T\bar{W}^T\bar{W}\bar{a}\vec{\Omega} = \bar{a}^T\bar{W}^T\bar{W}\vec{v'} \tag{3.22}$$

and finally solving for $\vec{\Omega}$

$$\vec{\Omega} = (\bar{a}^T \bar{W}^T \bar{W} \bar{a})^{-1} \bar{a}^T \bar{W}^T \bar{W} \vec{v'} \tag{3.23}$$

Confidence intervals on the activation volume tensor can be determined from initially calculating the error standard deviation as:

$$\hat{\sigma} = \sqrt{\frac{\vec{v'}^T (\bar{I} - \bar{a}(\bar{a}^T \bar{a})^{-1} \bar{a}^T) \vec{v'}}{N - 7}} \tag{3.24}$$

From this, the standard error matrix can be constructed

$$\bar{C} = \hat{\sigma}^2 (\bar{a}^T \bar{a})^{-1} \tag{3.25}$$

Finally, the 90 % confidence interval can be determined on each value in the activation volume vector, $\vec{\Omega}$, from the diagonal components of 3.25

$$\vec{\Omega_j} \pm t_{90,N-7} \sqrt{C_{jj}} \tag{3.26}$$

Alternatively, the error associated with a measurement was to take the difference between $\overline{\Omega^*}$ as measured with the maximum error and the minimum error. The maximum vector is calculated by adding the measurement error to the directional activation volume vector, v'

$$\vec{\Omega_{max}} = (\bar{a}^T \bar{W}^T \bar{W} \bar{a})^{-1} \bar{a}^T \bar{W}^T \bar{W} (\vec{v'} + \vec{\epsilon}) \tag{3.27}$$

In a similar fashion, the minimum vector is calculated

$$\vec{\Omega_{min}} = (\bar{a}^T \bar{W}^T \bar{W} \bar{a})^{-1} \bar{a}^T \bar{W}^T \bar{W} (\vec{v'} - \vec{\epsilon}) \tag{3.28}$$

and the maximum difference error is found by

$$\vec{\Omega_{max}} - \vec{\Omega_{min}} \tag{3.29}$$

The confidence interval error was used with the vacancy migration studies and point defect generation. The maximum difference error was used with the point defects.

3.5 The Second Invariant of the Activation Volume Tensor

Similar to the concept of the equivalent shear stress in solid mechanics problems, the second invariant of the activation volume, Λ, captures the deviatoric part of the activation volume tensor. In this work, this concept will be referred to as Λ. It can be calculated much in the same way as the equivalent shear stress as follows:

$$\Lambda = \sqrt{\frac{1}{6}[(\overline{\Omega_{11}} - \overline{\Omega_{22}})^2 + (\overline{\Omega_{11}} - \overline{\Omega_{33}})^2 + (\overline{\Omega_{22}} - \overline{\Omega_{33}})^2] + \overline{\Omega_{12}}^2 + \overline{\Omega_{13}}^2 + \overline{\Omega_{23}}^2} \tag{3.30}$$

Large values of Λ correspond to large deviations from complete uniform dilation of the system. Therefore, this value can tell you whether the activation volume scalar, which only captures the dilation or response to a hydrostatic load, is a good approximation to use when looking at how stress affects the Gibbs free energy of the system.

3.6 Calculating the Enthalpy Change from a Given Applied Stress

The purpose of this work is to understand how an applied stress state affects the kinetics of a given reaction. The change in enthalpy of activation was previously

given in equation 1.3 as:

$$H^* = E^* + pV^*$$

The pressure work term, pV*, is more accurately represented by the inner product of the applied stress tensor and the activation volume tensor:

$$\bar{\sigma} \cdot \overline{\Omega} \tag{3.31}$$

where $\bar{\sigma}$ is the symmetric applied stress tensor,

$$\bar{\sigma} = \begin{pmatrix} \sigma_{11} & \sigma_{12} & \sigma_{13} \\ \sigma_{12} & \sigma_{22} & \sigma_{23} \\ \sigma_{13} & \sigma_{23} & \sigma_{33} \end{pmatrix} \tag{3.32}$$

and $\overline{\Omega}$ is the activation volume tensor. The inner product then produces:

$$\sigma \cdot \overline{\Omega} \equiv \sigma_{11}\Omega_{11} + \sigma_{22}\Omega_{22} + \sigma_{33}\Omega_{33} + 2(\sigma_{12}\Omega_{12} + \sigma_{13}\Omega_{13} + \sigma_{23}\Omega_{23}) \tag{3.33}$$

Chapter 4

Method Validation: Vacancy Migration in FCC Copper

Vacancy migration in FCC copper consists of an atom swapping with a vacancy at one of its nearest neighbor sites. Vacancy migration is the primary mechanism for self-diffusion within the bulk of the material. This system is used to validate the methods implemented in this work for two primary reasons. Firstly, the system is well-characterized and results can be compared to computational and experimental literature. Secondly, atomic positions are also well understood and symmetric at the initial, saddle point, and final configurations of the transition, therefore relationships between the symmetry of the mechanism can be related to the activation volume tensor.

4.1 Simulation Parameters

The vacancy migration simulation cell consisted of a crystal of FCC copper with 2047 atoms, with edge lengths of 28.92 angstroms and periodic boundary conditions. The vacancy was placed at the origin of the unit cell, (0,0,0) and in the final state, it is

placed at the nearest neighbor site at ($a_0/2$, $a_0/2$, 0) The initial and final states are relaxed using conjugate gradient energy minimization methods before NEB was used to determine the activation energy of the event. The Mishin embedded atom method (EAM) potential was used to calculate the energies. [52]

4.2 Results

The formation and activation energies and volumes are well tabulated in FCC copper, therefore, these are used to verify the system parameters. The activation volume tensor, $\overline{\Omega}$, was determined for this system by Zhu et al. using a strain calculation method, this tensor is used to verify the calculated value of $\overline{\Omega}$ using the applied stress method. Finally, the second invariant of the activation volume, Λ, is used to describe the acceptability of using the activation volume scalar as a substitution for the activation volume tensor in practice.

4.2.1 Formation and Activation Energy

The formation energy was determined by equation 4.1, where E_f is the formation energy, m is the number of atoms in the perfect crystal, E_{vac} is the energy of the relaxed system with a vacancy in it, and E_{pc} is the energy of the perfect crystal.

$$E_f = E_{vac} - \frac{m-1}{m} E_{pc} \tag{4.1}$$

This value has been measured extensively in the copper diffusion literature [2] Since it is a commonly reported value, it provides us with a good check to verify that the initial vacancy configuration is at the minimized state.

The activation energy for the copper vacancy migration was determined using the method described in chapter 3. Table 4.1 shows the activation and formation energies for the vacancy migration in FCC copper. The calculated column refers to

the value determined in this work, the computational value is reported for the EAM potential and the experimental values come from measurements of diffusion. [52]. These numbers match closely, verifying the validity of NEB for this system.

Table 4.1: Formation and Activation Energy in FCC Cu Migration

	Calculated	Computational	Experimental
Formation Energy (eV)	1.272	1.27	1.27
Activation Energy (eV)	0.689	0.69	0.71

4.2.2 Activation Volume Scalar

The activation volume scalar captures the overall volume change between the initial configuration and the saddle point state. For the vacancy migration study, this value is reported in the validation work of the interatomic potential used. [52]Table 4.2 shows the activation volume scalar as compared to the reported value for the given EAM potential and experimental values. [52, 2] It should be noted that the activation volume referred to here is occasionally referred to as the activation volume of migration. This is the only part of the activation volume term for diffusion which involves adding the formation volume of the relaxed vacancy to this migration activation volume.

Table 4.2: Activation Volume in FCC Cu Migration

	Calculated	Computational	Experimental
Activation Volume (Ω_0)	0.107	0.107	0.12

It should be noted that the overall volume change between the initial and saddle point states is roughly 10% of the atomic volume of copper. This suggests that there is not a significant volume change for this transition, and therefore there will be no significant change in the activation enthalpy due to the pressure-volume term. Looking further, the activation volume tensor suggests a different story.

4.2.3 Activation Volume Tensor

The activation volume tensor was determined with 513 distributed directions of directional activation volume scalars, v', as shown in figure 4-1.

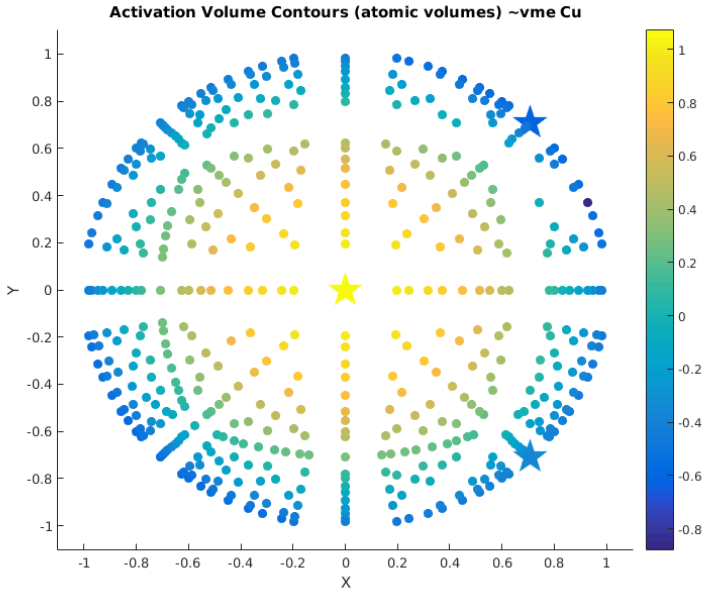

Figure 4-1: Directional activation volume scalar projection for Cu vacancy migration

In the reference frame of the simulation cell, the activation volume tensor is listed in table 4.3. It should be again noted that the direction of migration is along the (1,1,0) direction. The eigenvalues and eigenvectors show the magnitude of volume change in the principal directions, where only dilation occurs along the direction of the given vector. These values are shown in table 4.4 and are represented as the stars in figure 4-1

The activation volume tensor for copper vacancy migration has been calculated by Zhu and Li in their study of ultra-strength materials [10]. The local atomic strain between the initial state and the saddle point state is used to measure the activation volume tensor. Transforming their work into the reference frame of this simulation cell generates the tensor found in table 4.5. The reference tensor is very close to the calculated tensor, though roughly 1.15 larger than the calculated tensor, and the

Table 4.3: Activation volume tensor for FCC Cu vacancy migration

-0.4809	-0.1333	0
-0.1333	-0.4806	0
0	0	1.069

Table 4.4: Activation volume principal directions for FCC Cu vacancy migration

Magnitude	-0.614	-0.3475	1.069
Direction	0.7074	0.7068	0
	0.7068	0.7074	0
	0	0	1

trace of this tensor is 0.12 Ω_0. Since the trace of the tensor calculated in this work matches the computational reference value of 0.107, the applied stress method used in this work has been proven to be a valid technique to calculate the activation volume tensor.

Table 4.5: Reference activation volume tensor for FCC Cu vacancy migration

-0.5675	-0.1519	0
-0.1519	-0.5675	0
0	0	1.2505

4.2.4 Second Invariant of the Activation Volume Tensor

Most works that discuss stress effects on kinetic transitions only focus on the first invariant of the activation volume tensor, the activation volume scalar. This value only accounts for the spherical term of the tensor and the overall volume change. In order to better understand how the transition responds to stress, the second invariant of the activation volume tensor, the second invariant of the activation volume tensor, Λ, was studied. For this transition,Λ was 0.9045. This value is nine times larger than the activation volume scalar, which means that V^* is not similar to one of pure dilation, which would have zero off-diagonal terms and equal terms along the diagonal.

4.3 Discussion

As shown by the eigenvectors of the activation volume matrix in table 4.4, the vacancy migration in the (1,1,0) direction has one principal axis along this axis of migration and two principal axes in the directions perpendicular to the direction of migration. This is indicative of the symmetric nature of the saddle point. At the saddle point, the migrating atom is at the $(\frac{1}{4}, \frac{1}{4}, 0)a_0$ location. There are no atoms in the direct vicinity of the atom in the saddle point state in the principal directions. Additionally, the signs of these terms are negative to the term along the transition axis. When taking the sum of these terms, the activation volume scalar of 0.107 Ω_0 is an order of magnitude smaller than the largest diagonal term of 1.069 Ω_0.

This suggests that for this particular kinetic transition, using the activation volume scalar to calculate the pressure term of the enthalpy is only valid for the hydrostatic case. If, for instance, one were to apply a uniaxial tensile stress along the axis of migration of a given magnitude, the energy would drop by an order of magnitude larger than if a hydrostatic tension of the same magnitude was applied.

A few other features came out of this vacancy study. First, is that the symmetry of the activation volume tensor is dependent on the symmetry of the atoms at the saddle point state, not the symmetry of the underlying crystal structure. Additionally, there were a few directions in which an applied uniaxial stress produced a non-linear relationship between the activation energy and the stress magnitude. One of these directions is shown in figure 4-2. This specific direction corresponds to a direction of close-packed atoms aligned with the migrating atom at the saddle point configuration shown in figure 4-3. The other directions of close-packed atoms are similarly nonlinear and indicate the same symmetry as the saddle point configuration.

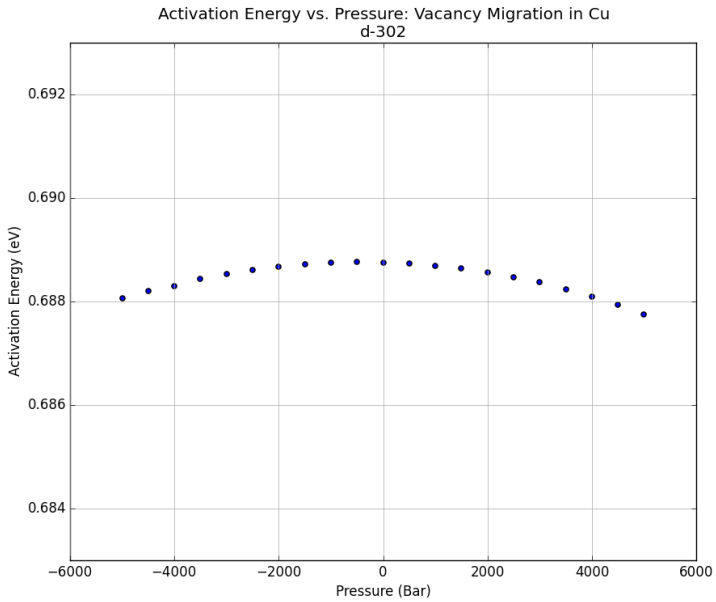

Figure 4-2: Nonlinear Directional Activation Volume Scalar

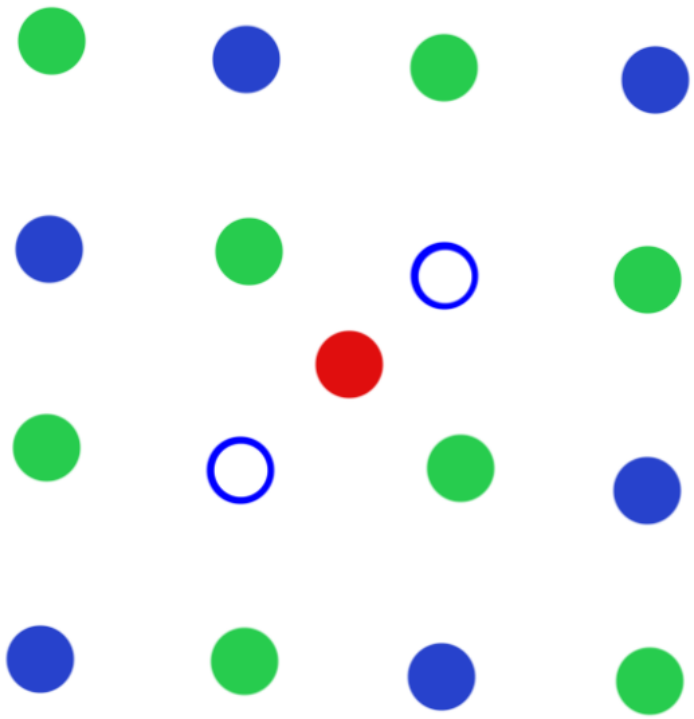

Figure 4-3: Saddle point configuration with close-packed directions

Chapter 5

Vacancy Migration in HCP Titanium

In addition to the FCC copper vacancy migration study described in chapter 4, the vacancy formation and migration was studied for α titanium. This hexagonal close packed (HCP) metal was chosen as a contrasting system to the FCC copper case; and because it is a well characterized kinetic transition with experimental results and a reasonable interatomic potential. [53, 54, 55, 56, 57, 58, 59]

There are two distinct vacancy migrations in HCP metals: migration within the basal plane of the vacant site and migration out of the basal plane. Within the basal plane, an atom exchanges positions with a nearest neighbor vacant site within the basal plane; similarly in the non-basal vacancy migration, an atom changes positions with a nearest neighbor vacancy out of the basal plane. Atom-vacancy exchange within the basal plane has been experimentally shown to occur at slightly lower activation energies than that out of the plane. [53]

5.1 Simulation Parameters

Both of the titanium vacancy migrations had simulation cells consisting of 2047 atoms and edge lengths of 23.3964 Å, 40.5238 Å, and 38.2062 Å for the x, y, and z coordinates respectively. The boundary conditions for this system were periodic in all directions, and the atomic spacing, a_0 was 2.975 Å. The embedded atom potential by Zope et. al was used for these simulations. Initial studies were performed comparing different interatomic potentials for titanium, but only the Zope interatomic potential performed well under an applied external stress [53, 60] For the basal migration study, the vacancy was located at the origin, (0,0,0) and was moved to the nearest neighbor site at (a_0,0,0). The out of plane migration also began at the origin, but was moved to the nearest neighbor site at (0, $\frac{a_0}{2}$, $\frac{4a_0}{5}$) These two configurations are shown in figure 5-1 and 5-2; these images are looking at the simulation cell with a viewing axis in the positive z-direction, colored according to bond energy.

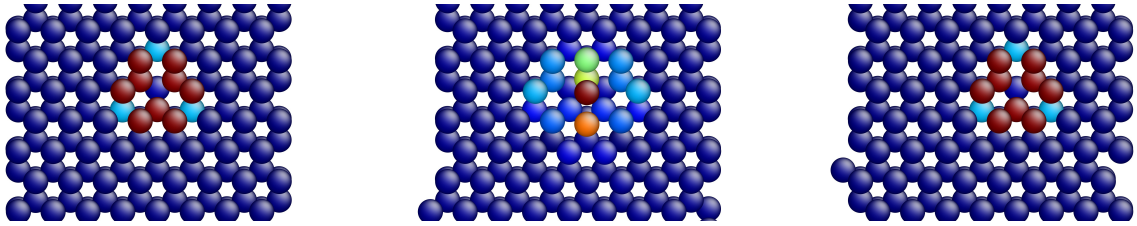

(a) Initial State (b) Saddle Point State (c) Final State

Figure 5-1: Basal Plane Vacancy Migration in HCP Ti

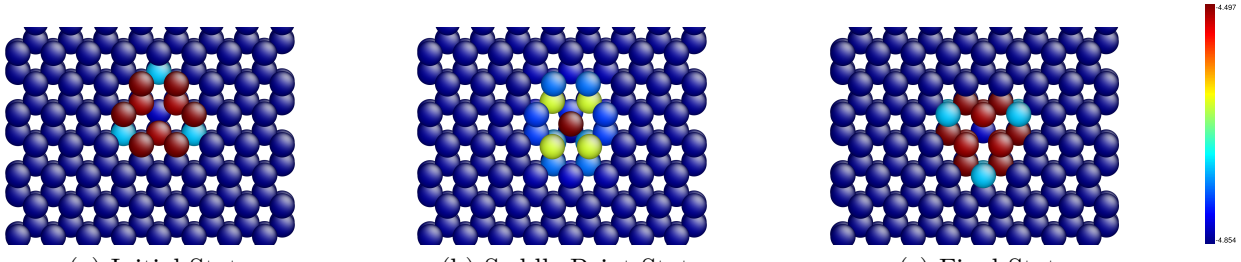

(a) Initial State (b) Saddle Point State (c) Final State

Figure 5-2: Non-Basal Plane Vacancy Migration in HCP Ti

5.2 Results

5.2.1 Formation and Activation Energy

The formation energy for a vacancy in HCP titanium was determined in the same method as for the copper vacancy using equation 4.1. Table 5.1 shows the comparison between the measured values in this study, the predicted reference values from the EAM potential, and the experimental values of formation and activation energy for each of the kinetic transitions. [53, 61]

Table 5.1: Formation and Activation Energies in HCP Ti Migration

	Calculated	Computational	Experimental
Formation Energy (eV)	1.82	1.83	1.55
Basal Migration Activation Energy (eV)	0.795	0.80	–
Non-Basal Migration Activation Energy (eV)	0.827	0.83	–

In agreement with prior work, the activation energy required to migrate out of the plane of the vacancy is greater than that required for in-plane migration and match closely with the reference values.[53, 61]

5.2.2 Activation Volume Scalar

The activation volume scalars in the titanium vacancy migration events are shown in table 5.2. The activation volume for a vacancy migration in α-Ti is not well characterized experimentally. One study was performed in the 1970's which worked to quantify the activation volume in dislocation migration [62], and several works look at the formation energy of titanium monovacancies [61]. In all of the literature on this topic, there are no values listed for direct comparison. [2, 58]

Table 5.2: Activation Volume in HCP Ti Migration

	Activation Volume Ω_0
Basal Plane Migration	0.0218
Non-Basal Plane Migration	0.0372

5.2.3 Activation Volume Tensor

The activation volume tensors for the basal and non-basal vacancy migrations were determined using 452 and 459 integer distributed directions, respectively, as shown in figure 5-3. The stars represent the principal directions mapped onto the directional unit hemisphere.

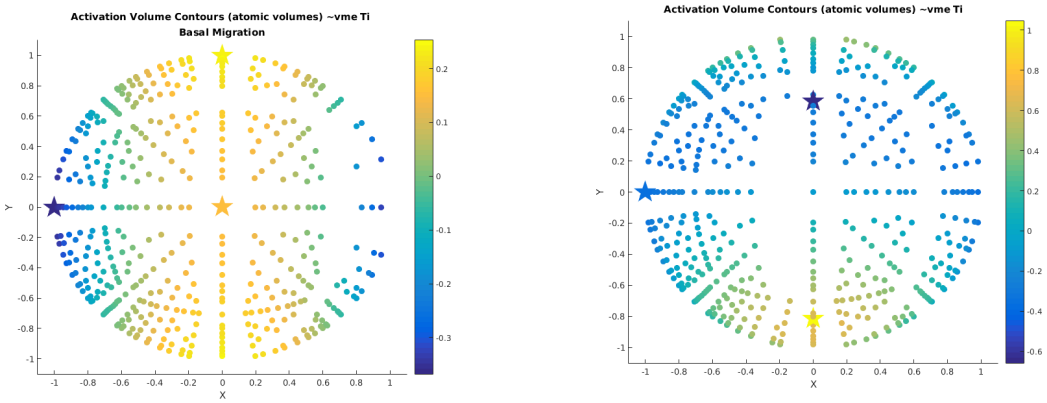

Figure 5-3: Distributed directions of v' for Ti vacancy migration colored by magnitude of v'

The activation volume tensors for each direction of migration are shown in tables 5.3 to 5.6. Tables 5.3 and 5.5 show the tensors within the frame of reference of the simulation cell, while tables 5.4 and 5.6 show the principal directions of the transition and magnitudes of the activation volume, where only dilation occurs in the given direction.

Table 5.3: Activation volume tensor for HCP Ti basal plane vacancy migration

-0.3677	0	0
0	0.2412	0
0	0	0.1489

Table 5.4: Activation volume principal directions for HCP Ti basal plane vacancy migration

Magnitude	-.3677	0.2412	0.1489
Direction	-1	0	0
	0	1	0
	0	0	1

Table 5.5: Activation volume tensor for HCP Ti nonbasal plane vacancy migration

-0.3501	0	0
0	0.4671	-0.8061
0	-0.8061	-0.0798

Table 5.6: Activation volume principal directions for HCP Ti non-basal plane vacancy migration

Magnitude	-0.658	-0.350	1.045
Direction	0	-1	0
	0.583	0	-0.813
	0.813	0	0.583

5.2.4 Second Invariant of the Activation Volume Tensor

The second invariant of the activation volume tensor describes the response of the kinetic transition to non-hydrostatic stress states. It is shown in table 5.7.

Table 5.7: Second Invariant of the Activation Volume in HCP Ti Migration

	Second Invariant of the Activation Volume Ω_0
Basal Plane Migration	0.3282
Non-Basal Plane Migration	0.6085

5.3 Discussion

The formation and activation energy for the kinetic events in Ti self-diffusion shown above are consistent with the literature. This provides confidence in the EAM potential used and verifies the model is correctly set up. Though the activation volume scalars are not commonly reported, the values for in-plane and out-of-plane migrations are similar, as expected. These values are an order of magnitude smaller , 0.02 Ω_0 , as compared to the activation volume of a vacancy migration in copper, 0.1 Ω_0. Therefore, the titanium vacancy migration events are less sensitive to applied stress than the copper vacancy migrations.

The second invariant of the activation volume, Λ, for the basal plane migration is approximately half of the out-of-plane value. As noted above, the activation volume scalar is approximately the same for both kinetic events. This suggests that the non-basal plane migration is more sensitive to non-hydrostatic stress states than the basal migration case.

For the basal migration case, the activation volume tensor in the reference frame of the simulation cell has no nonzero off diagonal terms and the primary directions are the simulation cell axes. For this transition, the migrating atom is moving in the (1,0,0) direction. At the saddle point, halfway between the two atomic sites, the atom has four nearest neighbor atoms symmetrically about itself as shown in figure 5-4. It also has free space in the three principal directions, including the direction of migration as shown in the red boxes. This makes sense because in these directions, the volume around the atom can freely grow or shrink without having to shear atoms out of the way.

The nonbasal migration in Ti is similar to that in copper; they both have one non-zero shear term. For this migration in the (0,0.5,0.8) direction, the principal directions are in the directions in which free space exists as shown in figure 5-5, one in the direction of migration, and two in the perpendicular directions of free space.

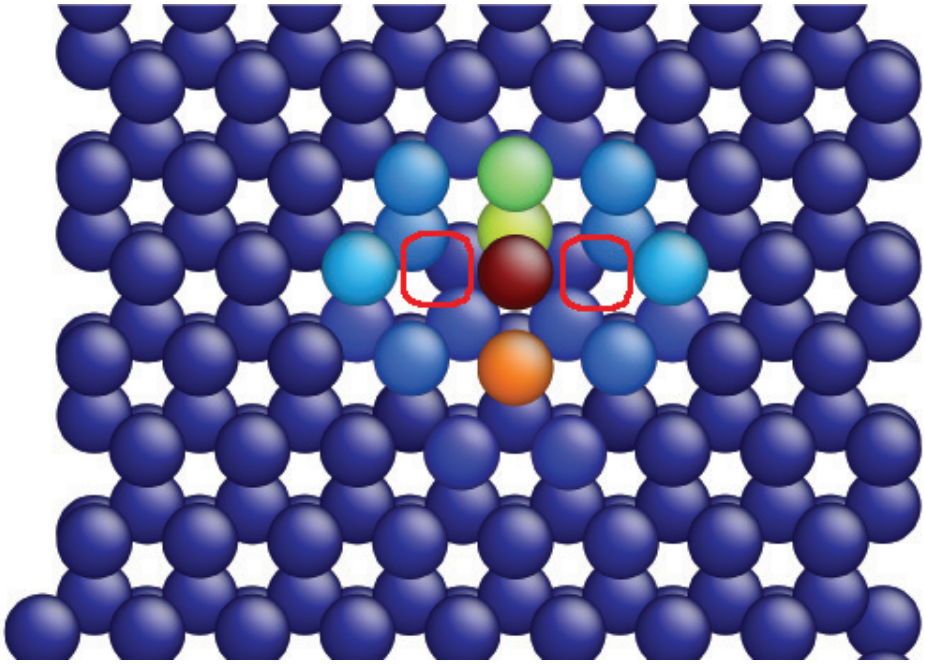

Figure 5-4: Basal Ti migration saddle point

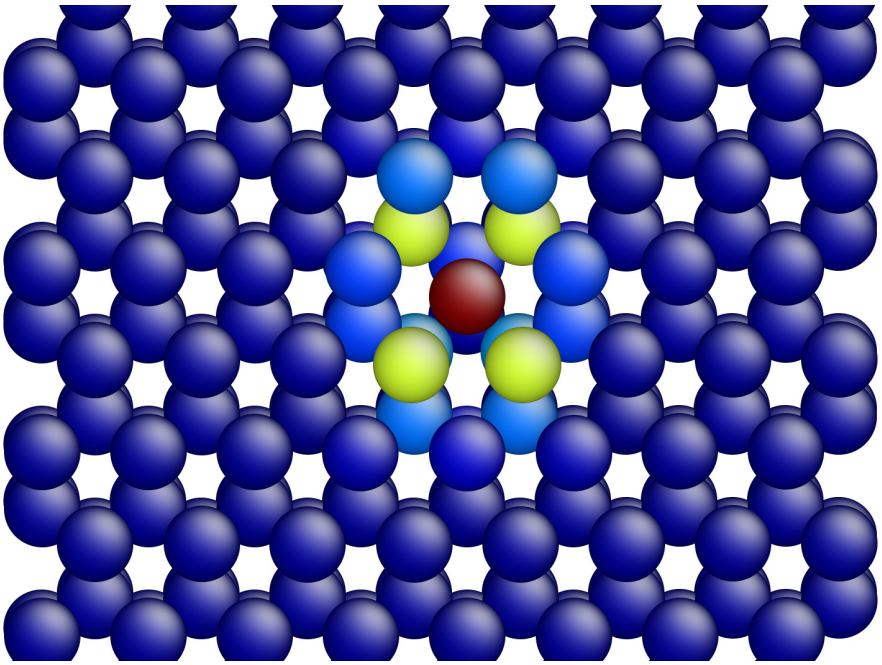

Figure 5-5: Non-Basal Ti migration saddle point

Chapter 6

Point Defects in FCC Copper

Point defects are one dimensional imperfections and play a crucial role in material properties including strength, hardness, and diffusion characteristics. Some point defects include interstitials with foreign atoms, self interstitials, vacancies, dumbbells, and substitutional defects. [2, 63]

In this work, we use the term point defect very loosely, meaning localized defects that emerge from a perfect crystal by a kinetic event. Two distinct types of local defects were studied: dumbbell/vacancy pair creation, and ring mechanisms. This work on local defects is a crucial step in understanding between the simplest vacancy migration studies described in earlier chapters, to the much more complicated studies of grain boundary kinetic events, described in the subsequent chapter. But the energy associated with the kinetic transitions of point defects is very high; they are, therefore, not likely to occur at a high enough rate for experiments to capture. Additionally, these defects are created in a perfect crystal where no preexisting defects exist. As stated in the beginning of this chapter, even the most ideal crystal has defects, therefore these kinetic events are more likely going to occur as several kinetic events in series.

6.1 Simulation Parameters

This is the first study in this thesis in which the activation relaxation technique (ART) was required in order to determine the final atomic configuration. For this, the technique developed by Mousseau, et al. [45] and later implemented by Alexander et al. [42] was implemented using the Mishin EAM potential [52]. The initial configuration consisted of a triclinic simulation cell with 500 atoms with equal edge lengths of 18.075 and periodic boundary conditions.

The activation relaxation technique was applied to this perfect crystal and over the course of 12 hours, it found 500 transitions with nine distinct values of activation energy ranging from 4.40 to 4.89 eV. Of these 500 successful measurements, eleven were chosen for further study, one for each distinct energy value which appeared at a low frequency, and two for those which the same activation energy appeared often. Initial studies on the activation volume scalar determined that some of these eleven transitions were fundamentally the same. Ultimately, we only fully studied five distinct transitions.

The nudged elastic band method for these defects used 12 replicas, an energy tolerance of 1×10^{-15} eV and a force tolerance of 5×10^{-9} eV/Å, the quickmin minimizer and a spring force coefficient of 5.

6.2 Results

6.2.1 The Two Categories of Defects

Of the 11 defects studied, there were two distinct subclasses of kinetic transitions: vacancy/dumbbell pairs and ring mechanisms. In the vacancy and dumbbell event, a vacancy was generated somewhere in the crystal, this caused a collective movement of atoms which ultimately led to a dumbbell located at a lattice site somewhere else

in the crystal. Figure 6-1 shows a schematic of how atoms are distributed in the final state. The ring mechanisms were events which resulted in another perfect crystal

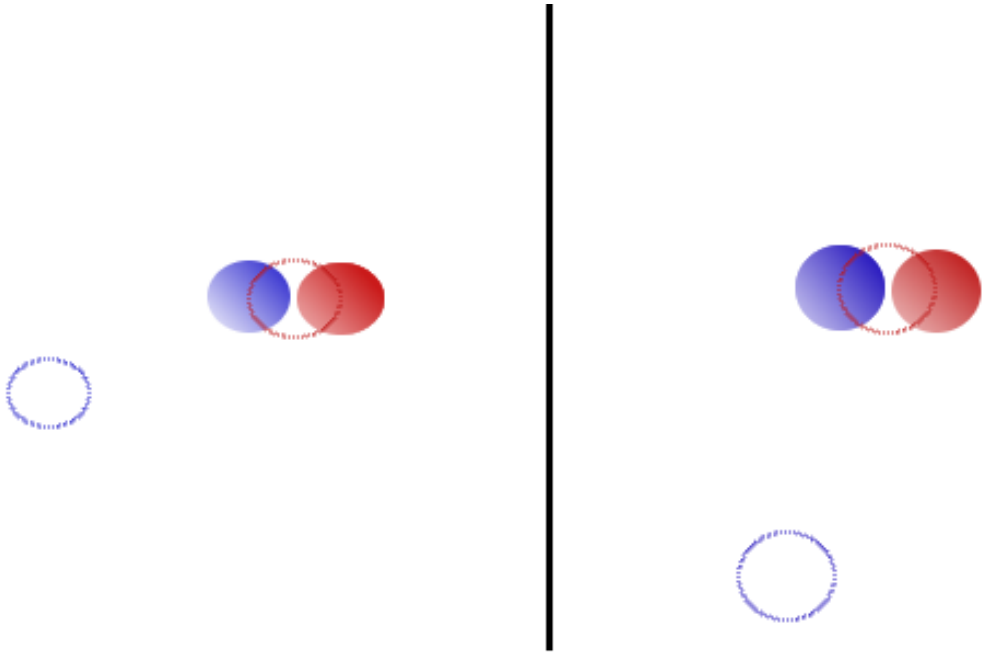

Figure 6-1: Dumbbell-Vacancy Mechanism

configuration, but with atoms in positions differing from those in which they started. Two atom, three atom, and four atom ring mechanisms were found in this study. The schematic in figure 6-2 shows how the atoms behave in these transitions.

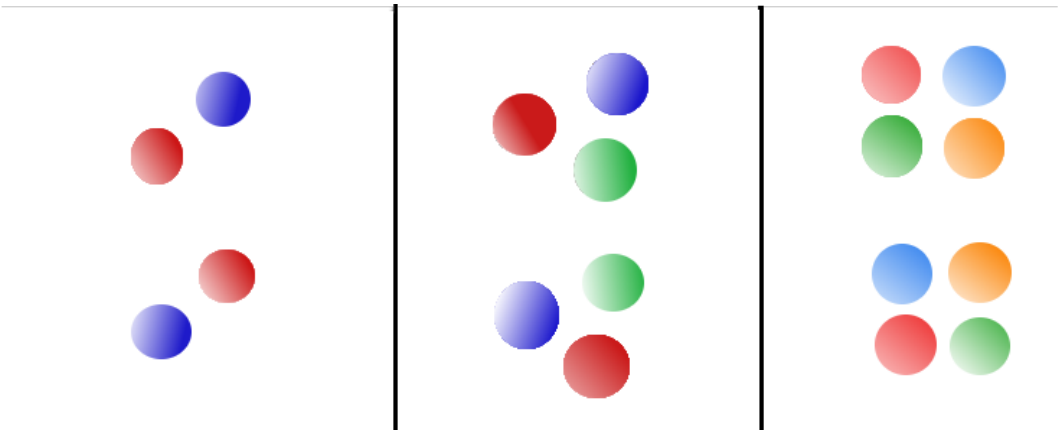

Figure 6-2: Ring Mechanism

The figures of the atomic configurations for each of the studied local mechanisms can be found in appendix B. However, a brief verbal description is given here in table 6.1.

It should be noted that the identifier used in this work corresponds to the activation energy in eV, as calculated by the ART method, multiplied by 100.

Table 6.1: Local point defect descriptions

Identifier	Description
440	dumbbell/vacancy pair with dumbbell aligned with traversal direction
444	dumbbell/vacancy pair with dumbbell aligned with traversal direction
457A	dumbbell/vacancy pair with dumbbell perpendicular to traversal direction
457B	dumbbell/vacancy pair with dumbbell perpendicular to traversal direction
458A	2 atom collective ring mechanism
458B	3 atom ring mechanism
462	4 atom ring mechanism
468	2 atom collective ring mechanism to dumbbell
476	2 atom collective ring mechanism
476B	2 atom collective ring mechanism
489	2 atom collective ring mechanism

6.2.2 Activation Energy and Activation Volume Scalar

The activation energy for each of the eleven transitions is listed in 6.2. The activation

Table 6.2: Local point defect activation energy and volume

Identifier	Energy (eV)
440	4.402
444	4.443
457A	4.577
457B	4.577
458A	4.676
458B	4.341
462	4.568
468	4.583
476	4.676
476B	4.676
489	4.676

Identifier	Volume (Ω_0)
440	1.55
444	1.58
457A	1.65
457B	1.65
458A	1.63
458B	1.53
462	1.58
468	1.77
476	1.63
476B	1.63
489	1.63

volume scalar vs. activation energy plot for these point defects is shown in figure 6-3. This shows a general increasing trend between activation volume and activation energy. This intuitively makes sense because as more atoms get involved with the transition, the energy and the volume change between the initial perfect crystal and the saddle point state increase together.

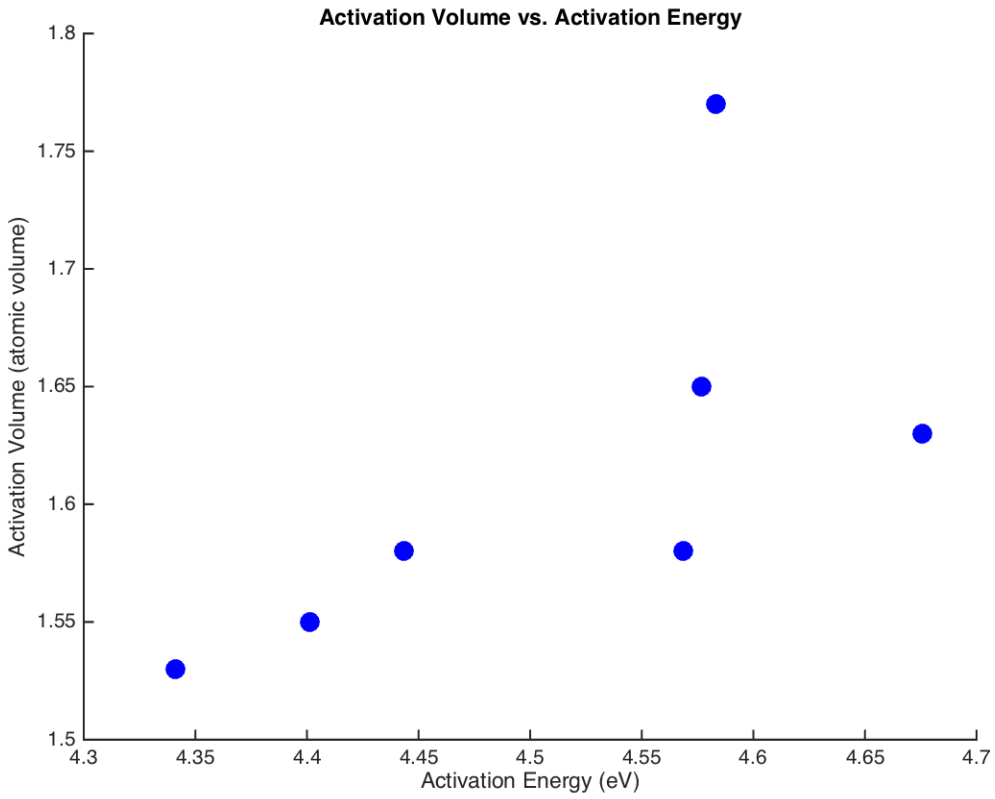

Figure 6-3: Activation Volume vs. Activation Energy

From these initial studies, it was determined that the 457A and 457B transitions were the same dumbbell/vacancy pair; this will be referred to as the 457 transition. The collective two-atom ring mechanism was also the same for the 458B, 476A, 476B, and 489 kinetic events; the 476 identifier will be used to represent this group of transitions. Transitions 440 and 444 were very similar in nature, with the 444 transition creating an unbound dumbell-vacancy pair, with the dumbell one lattice spacing further away from the vacancy; therefore, only the 440 transition was studied further.

6.2.3 Activation Volume Tensor

Of the eleven originally selected kinetic events, only five of the distinct transitions were further studied. The activation volume tensors in this work were determined using between 422 and 536 integer distributed directions as shown in appendix B. Table 6.3 shows the activation volume tensors for each of these five transitions.

Table 6.3: Activation volume tensors for selected point defects

Point Defect ID	Activation Volume Tensor
440 (|| dumbbell)	$\begin{matrix} 0.6555 & -0.0584 & 0.5062 \\ -0.0584 & 0.6721 & 0.0334 \\ 0.5062 & 0.0334 & 0.2228 \end{matrix}$
457 ($\perp$ dumbbell)	$\begin{matrix} 0.5660 & 0 & 0 \\ 0 & 0.5713 & -0.2773 \\ 0 & -0.2773 & 0.5817 \end{matrix}$
476 (2 atom ring)	$\begin{matrix} 1.368 & -0.0007 & 0.0074 \\ -0.0007 & 0.1183 & 1.439 \\ 0.0074 & 1.439 & 0.0871 \end{matrix}$
458B (3 atom ring)	$\begin{matrix} 0.4929 & 0.0702 & -0.0768 \\ 0.0702 & 0.5058 & -0.0854 \\ -0.0768 & -0.0854 & 0.5165 \end{matrix}$
462 (4 atom ring)	$\begin{matrix} 0.7842 & -0.1016 & -0.1019 \\ -0.1016 & 0.3963 & -1.879 \\ -0.1019 & -1.879 & 0.3965 \end{matrix}$

6.2.4 Second Invariant of the Activation Volume Tensor

The second invariant of the activation volume tensor was determined for each of the five transitions. These values are shown in table 6.4. These values should be compared to the activation volume scalars, V*, of the given transitions in order to understand the validity of using V* to represent the overall applied stress term.

Table 6.4: Point defect second invariant of the activation volume tensor

Identifier	Second Invariant of the Activation Volume
440 (|| dumbbell)	0.5707
457 ($\perp$ dumbbell)	0.2788
476 (2 atom ring)	1.6142
458B (3 atom ring)	0.1351
462 (4 atom ring)	1.8978

6.3 Discussion

There were two sub-categories of local defect studies: dumbbell/vacancy pairs and ring mechanisms. The activation energy for both types of events is very similar, therefore these values are not capable of predicting the physical nature of the mechanism. For the dumbbell/vacancy migrations, a higher distance between the dumbbell and the vacancy resulted in higher activation energy, because more atoms were displaced in the kinetic transition. For the ring mechanism, the four ring mechanism had greater activation energy and volume than the three ring mechanism, because more atoms were involved. This trend is also true with the two-atom ring mechanism, because although in the final state, only two neighboring atoms swapped positions, a very large number of atoms were displaced in the collective mechanism at the saddle point. High populations of disturbed atoms lead to large values of E* and V*. For all of these local defect kinetic events, the activation energy is much higher than for the vacancy migration studies, which had a preexisting defect in the crystal lattice.

These local kinetic events also show the full functionality of the second invariant of the activation volume, Λ. Remember that this term captures the deviatoric part of the activation volume tensor. When the Λ term is large with respect to the activation volume, like in point defect 462 (the 4 atom ring mechanism), the off-diagonal terms are large and the diagonal terms are different within the activation volume tensor. The uniform dilation assumption is not valid, and the activation volume scalar does not accurately represent the system under a non-hydrostatic load. If, however, the second invariant of the activation volume tensor is small compared to the activation volume scalar, as in point defects 457 ($\perp$ dumbbell) and 458B (the 3 atom ring mechanism), the off-diagonal terms are much smaller than the terms in the diagonal, which are nearly equal. These systems are well represented by the activation volume scalar, because they exhibit nearly uniform dilation and when any stress state applied, they will behave the same as a hydrostatic pressure.

As stated previously, the activation energy required to drive these kinetic events is very high. A calculation in the 457 dumbbell/vacancy pair shows that in order to reduce the activation energy to below 2 eV, a hydrostatic load of 21 GPa is required. This is several orders of magnitude larger than the ultimate tensile strength of copper.

6.3.1 Error

As stated in the chapter on vacancy migration in copper, non-linear trends exist between the activation energy and the applied stress state. In the studies on local defects, a second behavior emerged. In some directions of applied uniaxial stress, the event exhibited two different, yet linear trends in the activation energy versus volume. In this work, they will be referred to as "knees" in the data. Figure 6-4 demonstrates this behavior for a (-1, -2, 5) applied stress in the 2 atom ring collective point defect. It is currently unclear what causes these knees to exist, but the high sampling rate with relatively few knees and the weighting matrix under the high

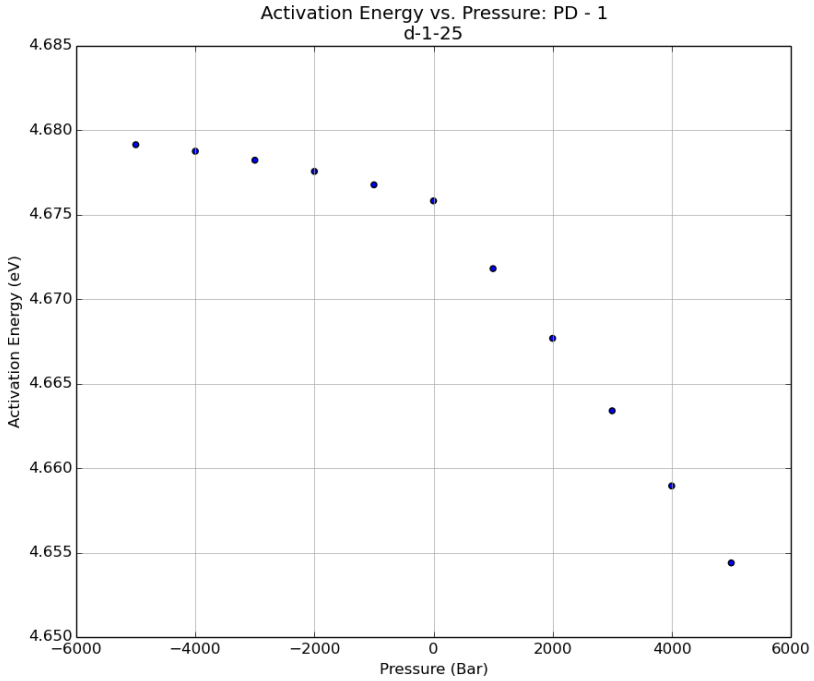

Figure 6-4: Non-Linear Activation Energy vs. Uniaxial Stress

error in the slope means that these are not a big contributing factor to the overall calculation of the activation volume tensor. The standard error ranges from 0.0005 Ω_0 for the 440 dumbbell vacancy pair to 1.324 Ω_0 for the 2 atom collective ring mechanism; appendix A shows the complete list of error arrays for each event.

Chapter 7

Grain Boundary Kinetic Transitions

This section focuses on kinetic events in the Σ5[210] grain boundary in FCC copper. The Σ5[210] boundary is a high angle, high energy symmetric tilt boundary which has been studied extensively by Frolov et. al. [64]. They also describe in great detail how this particular grain boundary was constructed. In this work, the grain boundary initial and final states were generated by my collaborator, Kathleen Alexander, using the activation relaxation technique. [42]

7.1 Simulation Parameters

Similar to the vacancy migration and point defect studies in copper, the grain boundary study used the EAM potential developed by Mishin et al. [52]. The simulation cell consisted of 2040 atoms and box dimensions of 18.044 Å, 16.143 Å, and 83.604 Å in the x, y, and z directions respectively. Figure 7-1 shows the grain boundary simulation cell at the initial configuration. There are two grain boundaries within this system in order to maintain periodic boundary conditions in all directions without

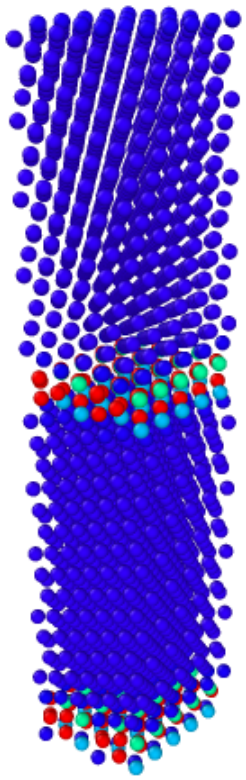

Figure 7-1: Σ5[210] Grain Boundary Simulation Cell

having free volume. The transitioning grain boundary is in the center of the cell in the x-y plane. The secondary boundary, which does not host any kinetic events in this study is parallel to this surface at 83.604 Å in the z-direction. Initial studies were performed in order to ensure that there was no interaction between these two grain boundaries at any point in the NEB process. These studies used 2960 atoms and had a z-dimension of 120.2 Å. Table 7.1 shows the energy per atom of the grain boundary regions for the two different grain boundary spacings.

Table 7.1: Grain Boundary Energy Comparison

Grain Boundary Spacing (Å)	Center Grain Boundary Energy (eV)	Distal Grain Boundary
83.6	-3.540	-3.540
120.2	-3.540	-3.540

After the initial and final configurations were determined using the activation relaxation technique, a known stress state was applied to the two given configurations and the system was relaxed to a minimum energy state using the conjugate gradient method. Finally the states were used as inputs to NEB with 20 or 24 replicas, a spring constant of 5, a cutoff energy of 1.0×10^{-15} eV , and a cutoff force of 5.5×10^{-9}eV/ Å.

The activation volume tensor for most of the kinetic transitions was determined using 74 evenly distributed uniaxial stress directions as shown in figure 7-2 (a). In order to ensure this was enough directions, the activation volume tensor for two of the kinetic transitions were also calculated with a higher sampling density of 526 evenly spaced directions as shown by figure 7-2 (b). These high directional density activation volume tensors matched closely with the low directional density values; however the error standard deviation as calculated by equation 3.24 was roughly an order of magnitude smaller with the higher sampling density. However, the reduction in the error is not worth the computational cost associated with running over seven times as many simulations, which would equate to over 350,000 extra simulations for just this small sample of kinetic events.

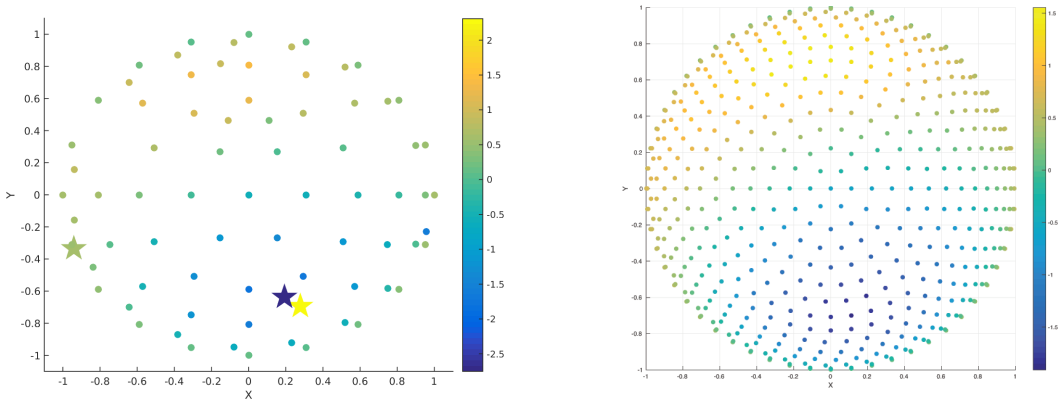

(a) Low density of stress directions

(b) High density of stress directions

Figure 7-2: Density of stress directions for grain boundary transition 112

7.2 Results

Similar to the local defect studies in copper, the grain boundary transitions are labeled by the activation energy determined by ART. It was determined that there were 70 distinct kinetic events with activation energies ranging from 0.72 eV to 2.44 eV. From these 70 kinetic transitions, 30 events were further analyzed.

7.2.1 Types of Grain Boundary Transitions

From analysis of the atomic displacements between the initial and saddle point states, two distinct trends emerge. The first is described by the global movement of bulk atoms in the simulation cell. In some kinetic transitions, the upper and lower grains slide relative to one another initiated by the local perturbation of the grain boundary; while, in other transitions, only local displacements within the grain boundary occurred. The secondary descriptor for the transition type is the local movement at the transition boundary. Some boundaries exhibited movement of atoms from one side of the grain boundary to the other, this will be referred to as a grain boundary migration mechanism. Other transitions exhibited atomic movement along the grain boundary, this is referred to as grain boundary diffusion. This is demonstrated schematically in

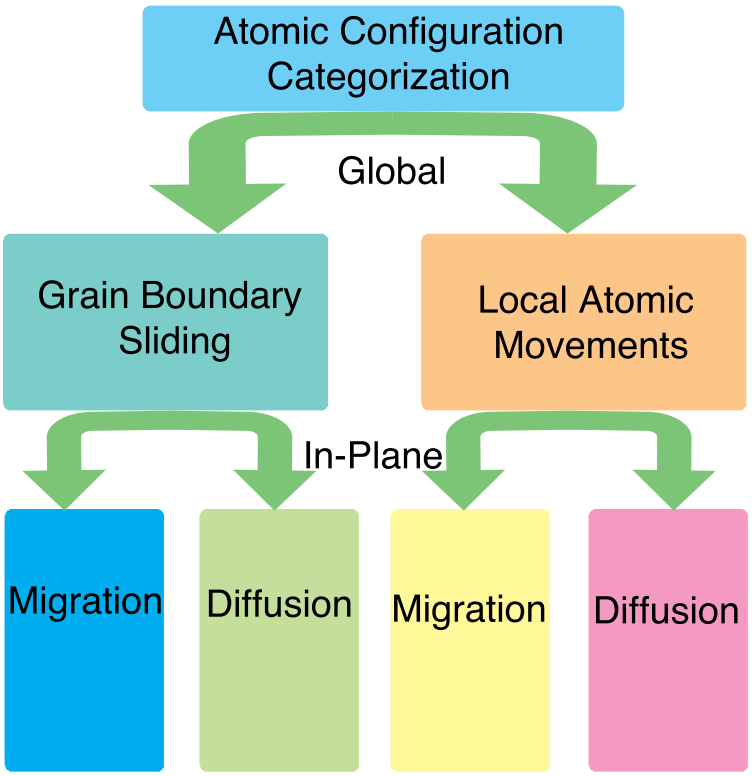

Figure 7-3: Categorization of Atomic Movements

figure 7-3.

The atomistic migration description for each of the grain boundary kinetic events is shown in table 7.2. These transitions are color coded based on the four types of movements.

Table 7.2: Grain Boundary Kinetic Event Descriptions

41	Diffusion along GB in Y with no sliding
70	Diffusion in X & Y, Sliding in Y
77	Migration from top and bottom grain with no sliding
81	Migration from top grain with no sliding
103	Migration from top and bottom grains with sliding in Y
112	Diffusion in X-Y direction with no sliding
126	Diffusion in Y with sliding in Y
127	Diffusion in X & Y with no sliding
134a	Diffusion in X with no sliding
135	Diffusion in X with no sliding
137	Diffusion in X with no sliding
137a	Migration from top grain with sliding in Y
138	Diffusion in X with no sliding
145	Migration from top grain with sliding in Y
146	Diffusion in X with no sliding
148	Diffusion in X with no sliding
150	Diffusion in X &Y with no sliding
154	Migration from bottom grain with sliding in Y
159	Diffusion in X & Y with no sliding
170	Diffusion in X with no sliding
177	Migration from top and bottom grain with sliding in Y
184	"Follow-the-leader" migration in X with no sliding
188	Migration from the bottom grain with sliding in Y
197	Migration from top grain with no sliding
206	Diffusion in Y with no sliding
212	Migration from bottom grain with sliding in Y
221	Migration from the top and bottom grains with sliding
230	Direct exchange of two grain boundary atoms
239	Diffusion in Y with no sliding
242	Diffusion in Y with no sliding

7.2.2 Activation Energy

The activation energy for the kinetic transition ranges from 0.75 to 2.50 eV as determined by NEB as described in chapter 3. These energies are significantly lower than the point defect events as described in the previous chapter. This is due to the fact that the grain boundary is a large planar defect and it takes much less energy to move atoms in a loosely packed atomic configuration where the number of close bonds are fewer; therefore, the energies are lower. Table 7.3 shows the activation energy at each different grain boundary transition.

Table 7.3: Grain Boundary Activation Energy

Event Identifier	Activation Energy (eV)
41	0.7491
70	1.1308
77	0.7094
81	0.7935
103	1.5558
112	1.1000
126	1.1308
127	1.4515
134a	1.4348
135	1.4412
137	1.4348
137a	1.3547
138	2.5011
145	1.3547
146	0.9671
148	1.4609
150	1.4609
154	1.3547
159	1.6073
170	1.6589
177	1.5340
184	no convergence
188	1.7488
197	1.9365
206	description
212	1.9365
221	1.9613
230	no convergence
239	no convergence
242	no convergence

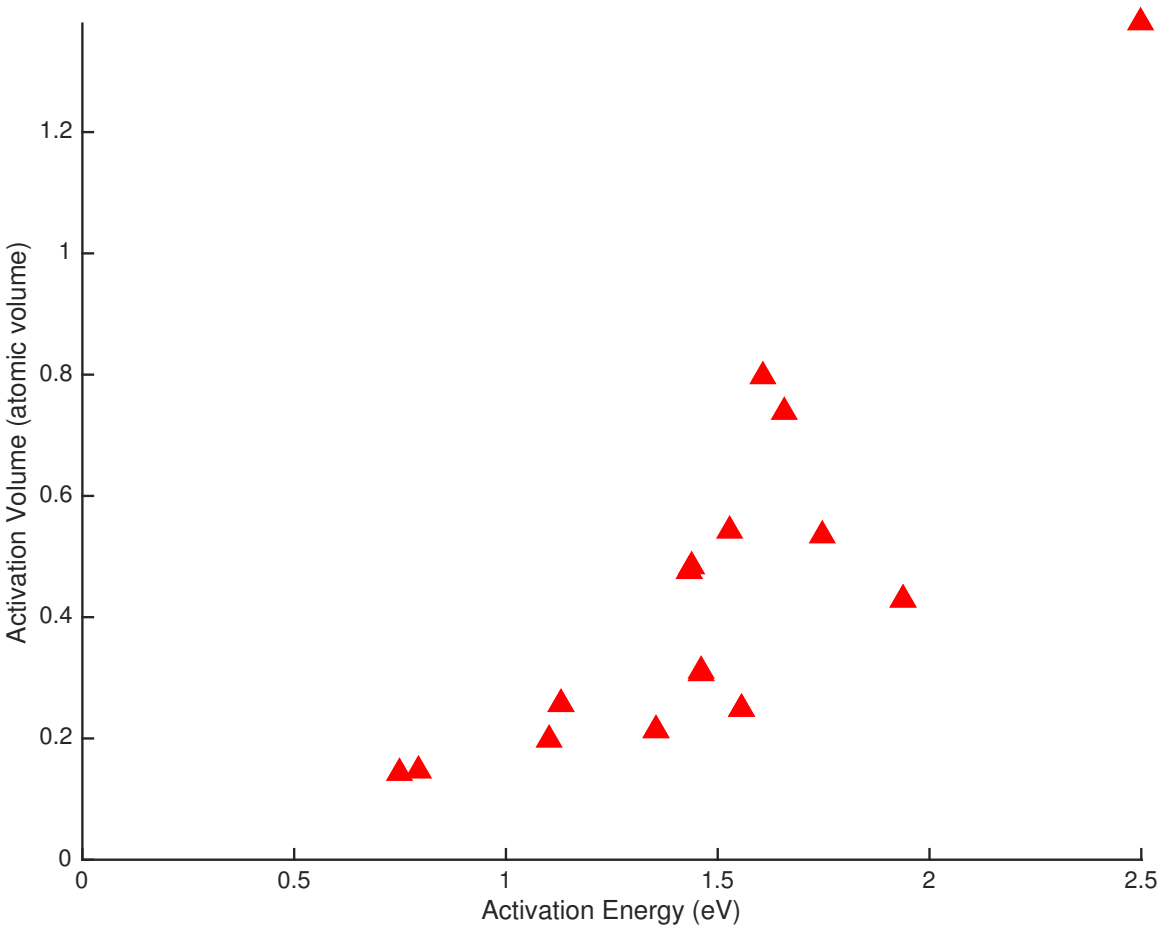

Figure 7-4: Activation volume vs. activation energy for grain boundary transitions

7.2.3 Activation Volume Scalar and the Second Invariant of the Activation Volume Tensor

The activation volume scalar, which is related to the spherical part of the activation volume tensor, and the second invariant of the shear activation volume are shown in table 7.4. The activation volume scalar has values ranging from 0.1557 Ω_0 to 1.8983 Ω_0. These values are plotted against the activation energy in figure 7-4 and show a generally increasing trend of V* with E*, as shown previously.

The second invariant of the activation volume has values between 0.7636 Ω_0 to 4.661 Ω_0. These values are significantly higher than those for the point defect generation or for vacancy migration. This means that there is a wider range of sensitivities to

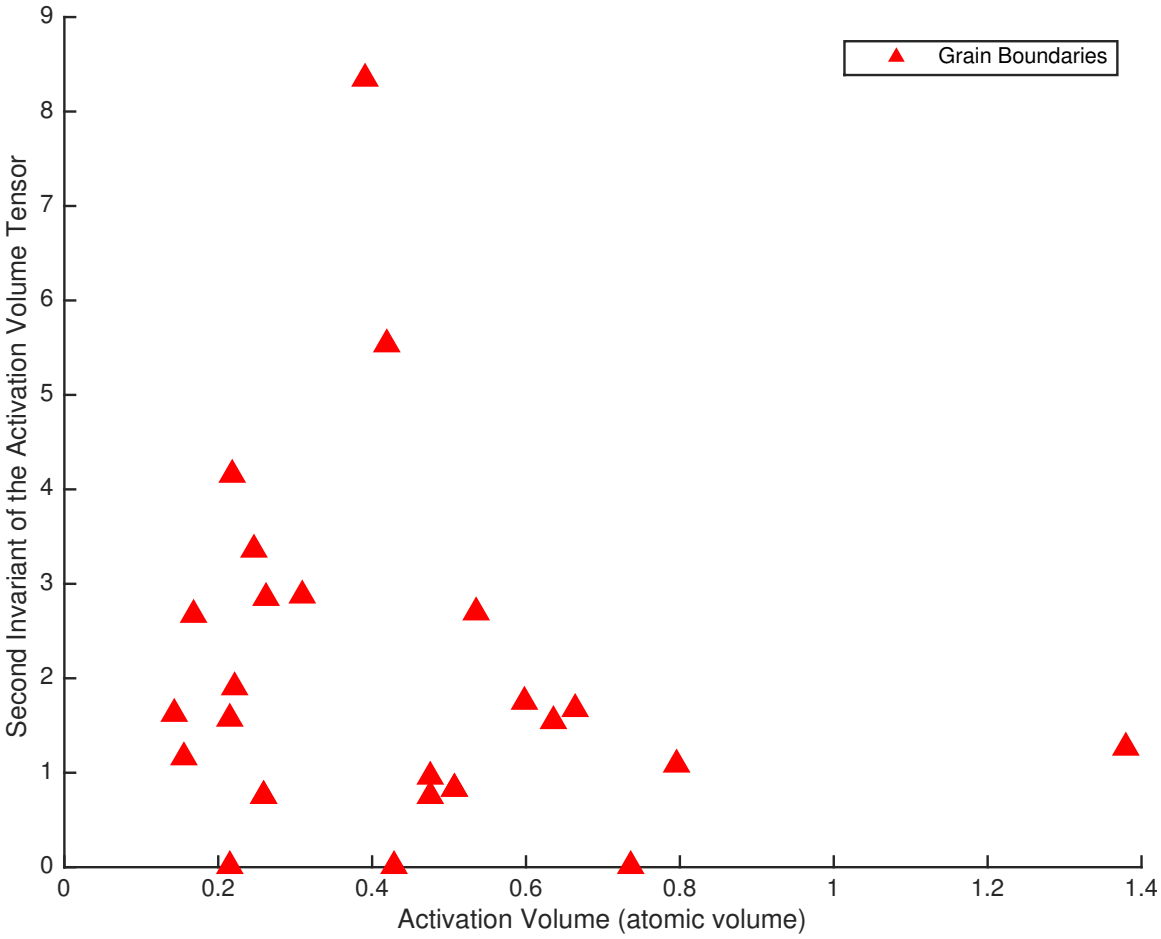

Figure 7-5: Λ vs. V* for grain boundary transitions

shear in the grain boundary kinetic events. This is likely due to the asymmetry and free volume within the grain boundaries. Figure 7-5 shows the second invariant of the activation volume plotted versus the activation volume scalar. As expected, and unlike the V* vs. E* plot, there is no general trend relating Λ and V*.

Table 7.4: Grain boundary activation volume and second invariant of the activation volume tensor

Event Identifier	Activation Volume (Ω_0)	Second Invariant Activation Volume (Ω_0)
41	0.2889	1.6220
70	0.3125	0.7539
77	0.2594	1.6853
81	0.1557	1.1557
103	0.4019	3.3676
112	0.1677	2.6731
126	0.3179	0.7636
127	0.2178	no convergence
134a	0.5668	0.9468
135	0.5082	0.8327
137	0.4741	.7586
137a	1.0853	no convergence
138	1.4406	1.2726
145	0.3899	no convergence
146	0.5054	0.8385
148	0.2676	2.8807
150	0.2618	2.8628
154	0.2792	1.5679
159	0.7935	1.0798
170	0.6281	0.7928
177	0.6365	1.5509
184	no convergence	
188	1.8983	2.6904
197	0.4175	4.5235
206	0.2215	no convergence
212	0.4175	4.5235
221	0.5991	1.7548
230	no convergence	
239	no convergence	
242	no convergence	

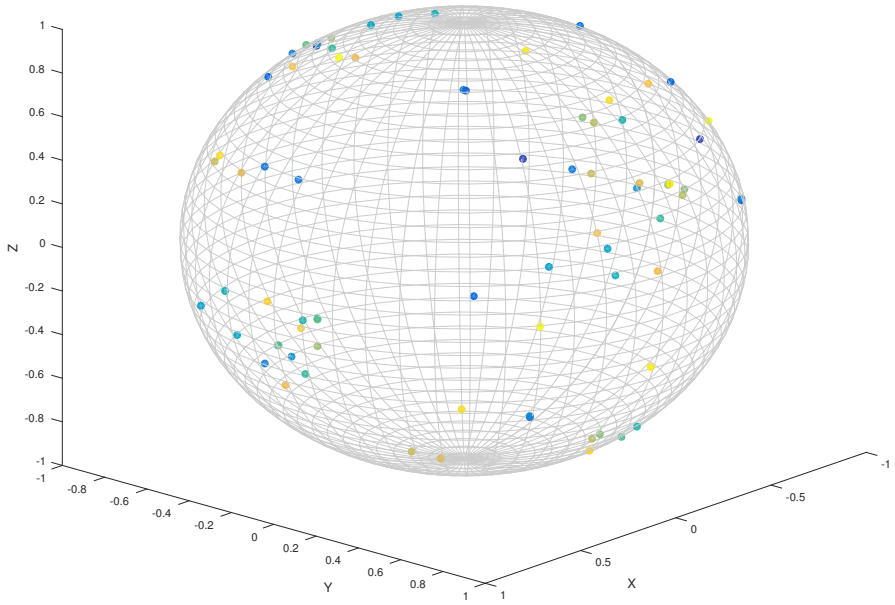

Figure 7-6: Spherical Distribution of Principal Directions of Grain Boundary Transitions

7.2.4 Activation Volume Tensor

For the sake of readability, the activation volume tensors are only listed in appendix A. This section will instead focus on the overall trends within the grain boundary kinetic events.

Figure 7-6 shows the spherical distribution of eigenvectors for each of the grain boundary transitions. Each color represents a different grain boundary kinetic transition. As discussed in previous chapters, the eigenvectors are the directions in which the shear components of the activation volume tensor are zero. This plot shows no distinct trends, which may appear as clusters, and that the directions are randomly dispersed along the surface of the unit sphere. This means that the dilation between the initial and saddle point configurations is distinct for each different event.

7.3 Discussion

Just like for the point defects, the activation energy in the grain boundary kinetic transitions is related to two main things: the number of atoms involved in a transition and the displacement. To illustrate this point, take for example the 77 and 81 kinetic events, which have energies of 0.7094 and 0.7935 eV respectively. These events involve highly localized atomic migration across the grain boundary. Very few atoms are required to move in order to accommodate the very short distance traversed. Compare this to the 212/197 kinetic event, which had one of the highest activation energies of 1.9365 eV and consisted of several atoms migrating along the x-axis down the grain boundary. Similarly, as more atoms are involved in the transition, the activation volume also increases, because there are more contributions to the volume shift between the initial and activated states. However, there are no easily discernible trends in the activation volume tensors or the second invariant of the activation volume tensors that can be established without looking at the individual mechanisms themselves.

Unlike the simple vacancy migrations and point defect studies, the grain boundary atomic movements consisted of complex movements in asymmetric geometry. There is, therefore, no simple mapping between the atomic movements of these events with their activation volume tensor. Figure 7-7 and 7-8 show the activation volume vs activation energy and second invariant of the activation volume tensor, respectively, as colored by the movement type. The random distribution of each color demonstrates that there is no distinct trend. This is expected, because as stated previously, the activation parameters are highly dependent on the atomic configurations at the saddle point state.

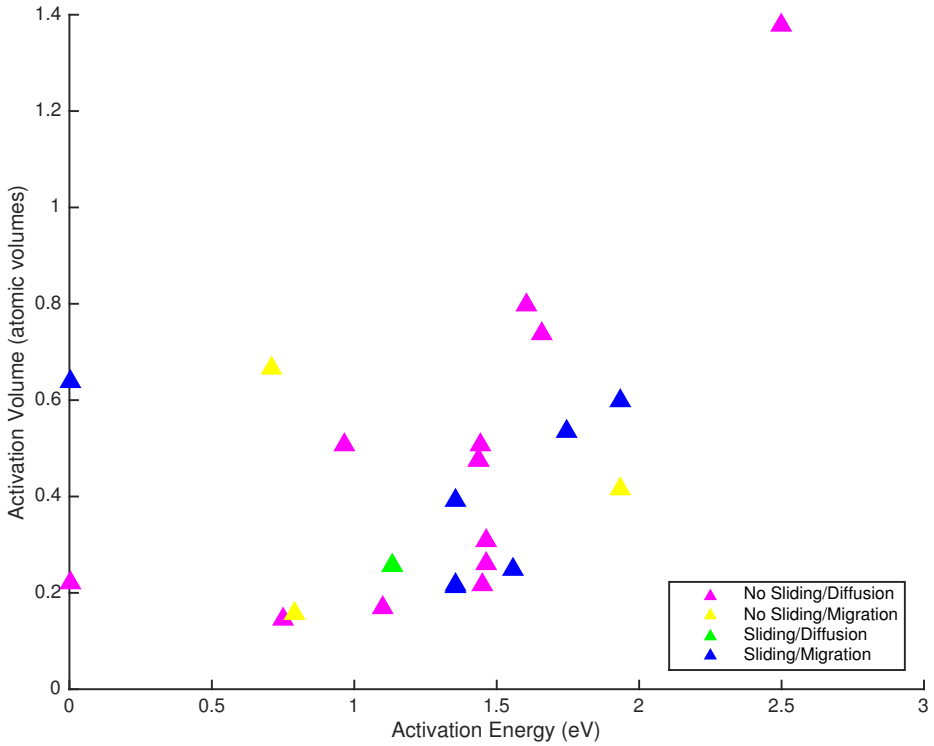

Figure 7-7: Activation volume vs. activation energy for grain boundary kinetic events as colored by the movement type

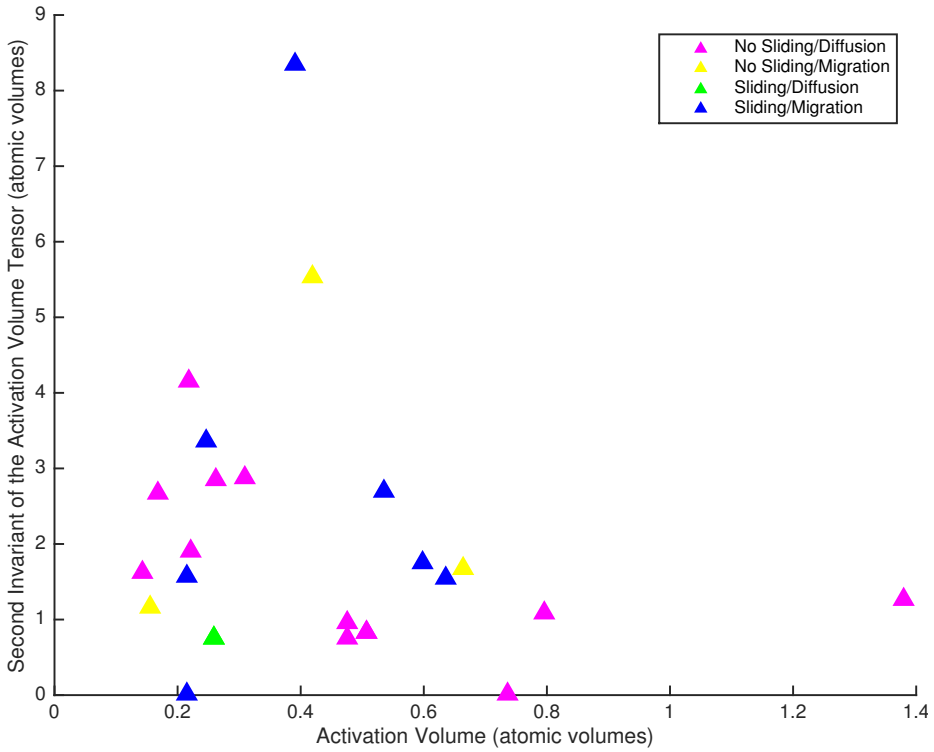

Figure 7-8: Second invariant of the activation volume vs. activation volume scalar for grain boundary kinetic events as colored by the movement type

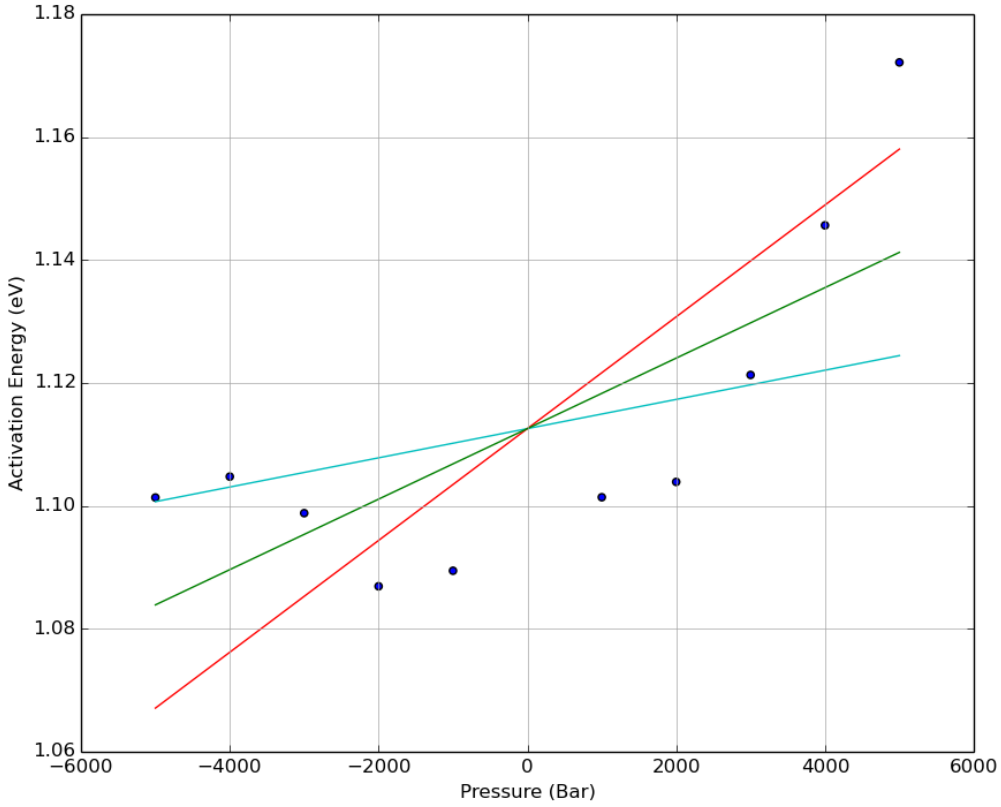

Figure 7-9: Curved non-linear direction

7.3.1 Error

The error in the activation volume tensor for the grain boundary kinetic events is much higher than that of the vacancy migration and point defect studies. This is most likely due to a high population of non-linear directions between the activation energy, E*, and the applied uniaxial stress, P. One example is shown in figure 7-9.

Though this data is for grain boundary transition 112, this specific shape occurs often in many of the different kinetic events. Additionally, this same shape appears for the applied uniaxial stresses which are symmetrically spaced about the Z-axis to the specific direction. In this example, the stress is applied in the (0.2937, 0.5091, 0.8090) direction within the simulation cell, this trend also appears in the (0.2937, -0.5091,

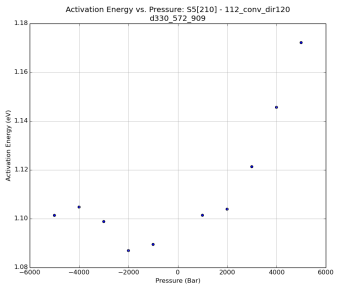

(a) (0.29, 0.51, 0.81)

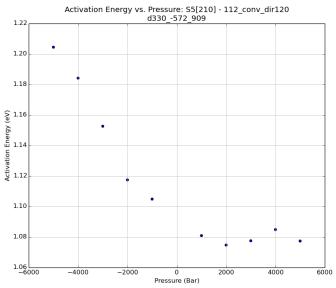

(b) (0.29, -0.51, 0.81)

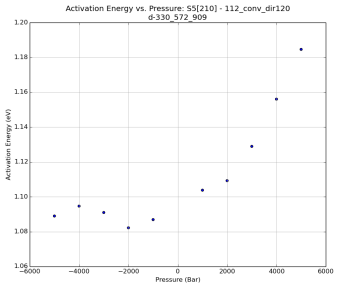

(c) (-0.29, 0.51, 0.81)

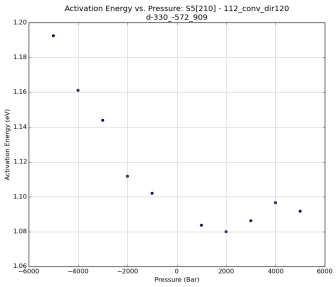

(d) (-0.29, -0.51, 0.81)

Figure 7-10: Non-linear trends in symmetric directions

0.8090), (-0.2937, 0.5091, 0.8090), and (-0.2937, -0.5091, 0.8090) directions, as shown in figure 7-10. As discovered in the copper vacancy migration study, non-linearities can be related to close-packed directions aligned with the saddle point atoms. Due to the symmetric nature of these directions, alignment to specific features within the grain boundary plane may be source of these non-linearities.

There exists a secondary type of non-linearity in the grain boundary directional activation volume scalars. This type consists of jagged linear sections, of alternating slope, as shown in figure 7-11 is similar to that which is found in the study on local defects.

It should be noted that these directions have a high error in the slope measurement, and are therefore, have a small weight in the weighted least squares regression analysis.

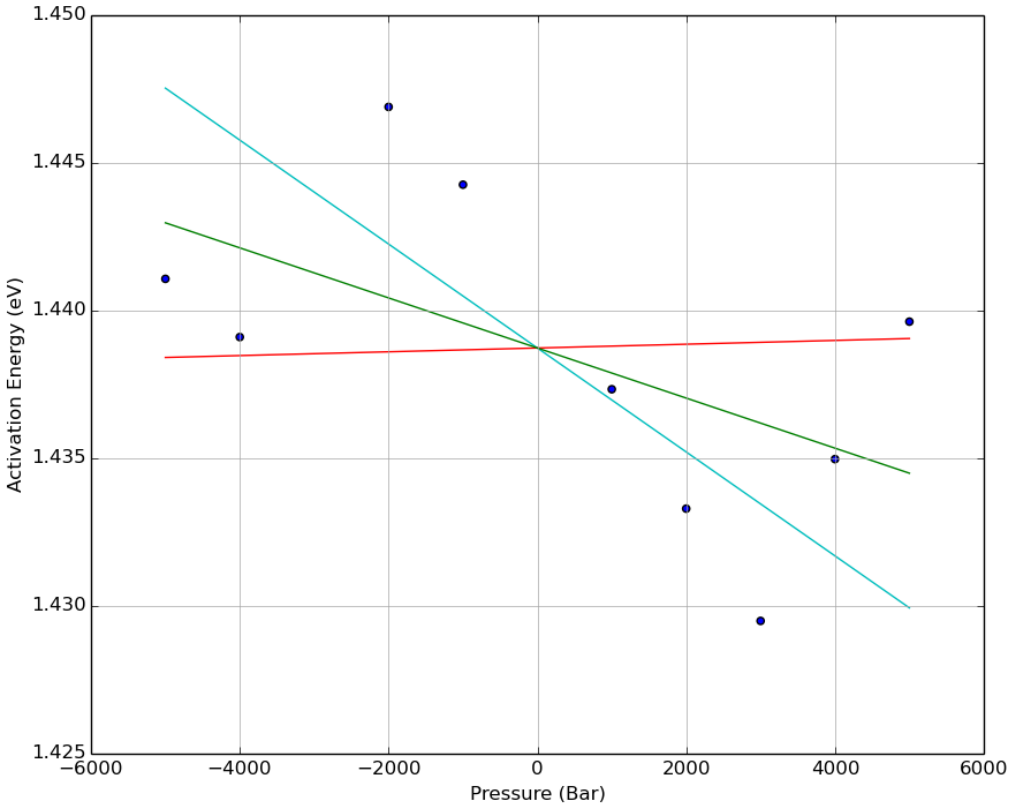

Figure 7-11: Jagged non-linear direction

Chapter 8

Conclusions

8.1 Activation Energy, Activation Volume Scalars, and the Second Invariant of the Activation Volume Tensor

This work demonstrates that the stress effects on kinetic events can be described in a multitude of ways. The first method for capturing the stress effects is through the first invariant of the stress tensor. The activation volume is commonly used when discussing how kinetic events behave under an applied load, but as shown in this work, it only tells part of the story and for most cases; it is not sufficient in capturing what happens under a stress state more complex than the simplest case of hydrostatic pressure.

The second way to describe how stress affects kinetic events is by analyzing the second invariant of the activation volume tensor. This value captures the deviatoric part of the activation volume tensor. It is useful in describing how sensitive the kinetic event is in response to a more physically realistic non-hydrostatic load in a singular, scalar value.

The final and most comprehensive method for understanding how a kinetic transition is affected by an applied stress state is by looking at the activation volume tensor. This second rank tensor physically represents the change in size and shape between the initial and saddle point states of the kinetic event. The scalar product between this tensor and the stress tensor determines the change in the activation energy under the applied load. When high applied stress or internal stress is coupled with the high magnitude values within the activation volume tensor, the Gibbs free energy barrier can be affected drastically. This phenomenon is not ordinarily captured by the more simplistic single value activation parameters.

The most simple kinetic events, such as vacancy migrations, are good systems to study in order to understand the relationships between the physical transition and the activation parameters. The copper and titanium vacancy studies demonstrated that the activation energy for single atom transitions is relatively low. The activation volume scalar is just the trace of the activation volume tensor, and therefore sign cancellations within the diagonal terms make the activation volume scalar much smaller than the individual terms. The principal directions of the activation volume tensor correspond to directions of free space around the atom at the saddle point state. The second invariant of the activation volume is much higher than the activation volume scalar, which suggests that the activation volume scalar is an oversimplification of the stress effects, and the activation volume tensor should be used instead. Additionally, these studies showed that non-linear behavior appears between the activation energy and the applied stress state magnitude when a uniaxial stress is applied in the direction of close-packed atoms aligned with the saddle point configuration.

The local defect studies helped move the work in a more complex direction with multiple atoms moving simultaneously to get from a perfect lattice to a final state which consisted of either another perfect lattice or a dumbbell and vacancy pair. These were events which took a high amount of energy and were highly sensitive to the hydrostatic stress state, with high magnitudes of activation volume. Although the activation volume did not vary much between the different transitions studied, the

second invariant of the activation volume varied greatly. The transitions with low Λ values had very small shear components and similar values along the diagonal, which means the reaction to any load is similar to the hydrostatic case, and the activation volume scalar nicely captures the effects. However, when Λ is high, significant off-diagonal terms exist, the magnitudes along the diagonal vary greatly, the assumption of hydrostatic load is not valid and the activation volume scalar no longer provides enough information. The final piece of insight that these transitions provide is that in complex atomic configurations, the directional activation volume scalar can change based on the load applied. In some directions of applied uniaxial load, the behavior was completely different for tensile and compressive loads.

The most complex system studied in this work was in the $\Sigma5[210]$ grain boundary in copper. The events occurring at the grain boundary were sorted by two movement type categories: global and local. Globally, some transitions exhibited bulk sliding between the two grains in order to accommodate the given kinetic event and others that did not. Secondly, the local atomic movements within the grain boundary were divided between those which the majority of the movement occurred along the plane of the grain boundary, which has been coined as diffusion, and those which the movement primarily occurred across the grain boundary, which is referred to as migration. There is no correlation between these overall movement classes with the activation parameters. There is, however, a relationship between the number of atoms involved in a given transition and the distance traveled by migrating atoms which can be qualitatively related the the activation energy and volume.

For all kinetic events, there was a general trend of increasing activation volume with activation energy. This is a well studied and understood phenomenon [7] shown in figure 8-1.

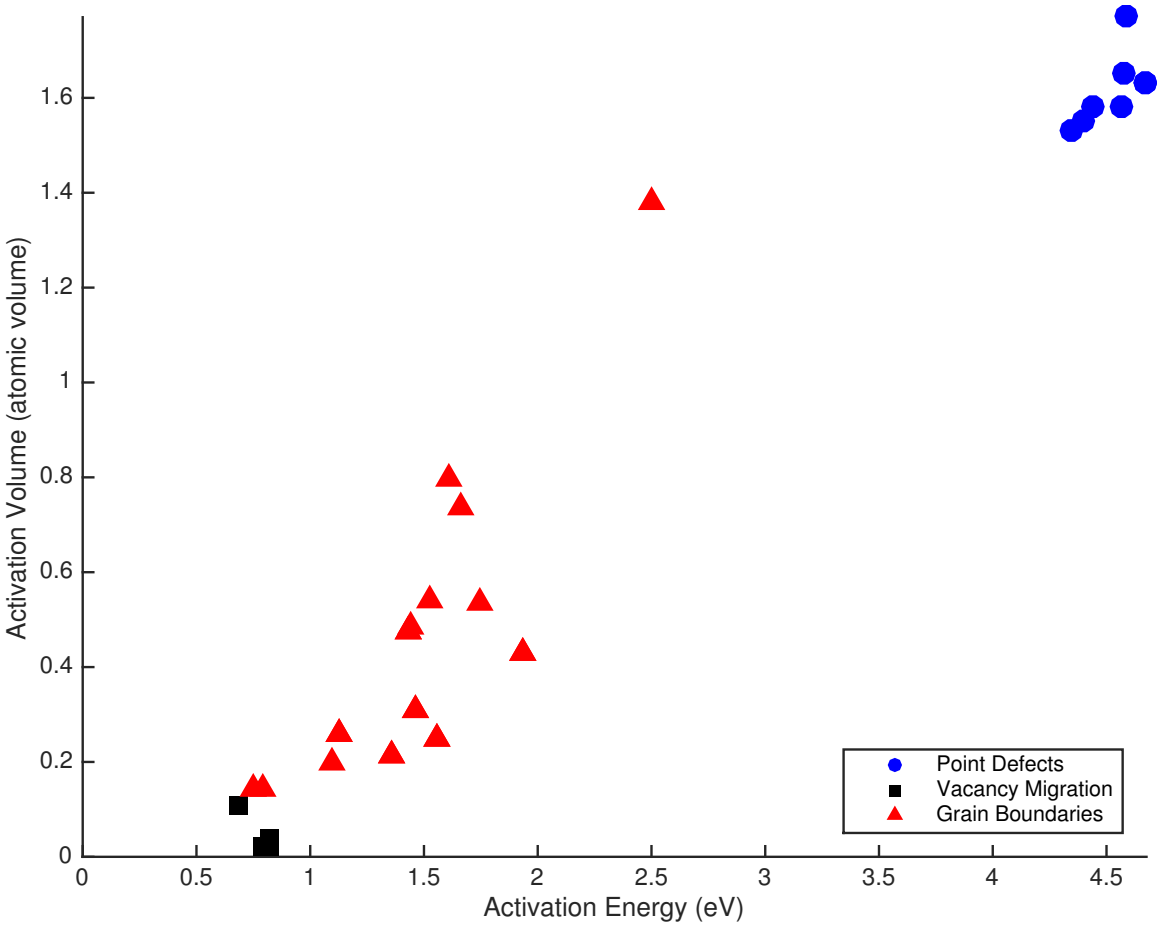

Figure 8-1: Activation Volume vs. Activation Energy for All kinetic events

8.2 Future Directions

Stress effects on kinetic transitions is a sparsely populated topic of research. Upon completion of this project, I am left with more questions than answers I have created. There are many topics within this field which should be explored beyond this work. One topic of future study would be to investigate the abrupt change in trends of the directional activation volume scalar, v', between the various regions of stress in the local defect studies. Additionally, it would be useful to efficiently visualize the activation volume axes on the actual crystal structure at the transition point. Another useful study in the realm of point defects would be to investigate how solute atoms might behave under load in binary systems. In the larger scope of this project, applying this process to transitions in other grain boundaries would be the next step in finding out how grain boundary kinetics behave under applied stresses. Finally, it would be useful to connect with the larger field of grain boundary engineering to use these tools in the study grain boundary mobility.

Appendix A

Activation Parameters Tables

A.1 Vacancy Migration in FCC Cu

Table A.1: Formation and Activation Energy in FCC Cu Migration

	Calculated	Computational	Experimental
Formation Energy (eV)	1.272	1.27	1.27
Activation Energy (eV)	0.689	0.69	0.71

Table A.2: Activation Volume in FCC Cu Migration

	Calculated	Computational	Experimental
Activation Volume (Ω_0)	0.107	0.107	0.12

* from the work of Zhu and Li using a strain measurement calculation [10]

Table A.3: Activation volume tensor for FCC Cu vacancy migration

-0.4809	-0.1333	0
-0.1333	-0.4806	0
0	0	1.069

Table A.4: Zhu reference activation volume tensor for FCC Cu vacancy migration *

-0.5675	-0.1519	0
-0.1519	-0.5675	0
0	0	1.2505

Table A.5: Activation volume principal directions for FCC Cu vacancy migration

Magnitude	-0.614	-0.3475	1.069
Direction	0.7074	0.7068	0
	0.7068	0.7074	0
	0	0	1

A.2 Vacancy Migration in HCP Ti

The basal plane vacancy migration in HCP titanium is in the (1,0,0) direction and the out of plane migration was along the (0,0.5, 0.8) direction.

Table A.6: Formation and Activation Energies in HCP Ti Migration

	Calculated	Computational	Experimental
Formation Energy (eV)	1.52	1.83	1.55
Basal Migration Activation Energy (eV)	0.795	0.80	
Non-Basal Migration Activation Energy (eV)	0.827	0.83	

Table A.7: Activation Volume in HCP Ti Migration

	Activation Volume Ω_0
Basal Plane Migration	0.0218
Non-Basal Plane Migration	0.0372

Table A.8: Activation volume tensor for HCP Ti basal plane vacancy migration

-0.3677	0	0
0	0.2412	0
0	0	0.1489

Table A.9: Activation volume principal directions for HCP Ti basal plane vacancy migration

Magnitude	-.3677	0.2412	0.1489
Direction	-1	0	0
	0	1	0
	0	0	1

Table A.10: Activation volume tensor for HCP Ti nonbasal plane vacancy migration

-0.3501	0	0
0	0.4671	-0.8061
0	-0.8061	-0.0798

Table A.11: Activation volume principal directions for HCP Ti non-basal plane vacancy migration

Magnitude	-0.658	-0.350	1.045
Direction	0	-1	0
	0.583	0	-0.813
	0.813	0	0.583

Table A.12: Second invariant of the activation volume tensor in HCP Ti migration

	Second invariant of the activation volume tensor Ω_0
Basal Plane Migration	0.3282
Non-Basal Plane Migration	0.6085

A.3 Point Defects in Cu

The following section contains the activation parameters for point defect events generated in a perfect crystal of FCC copper as described in chapter 6.

Table A.13: Local Point Defect Descriptions

Identifier	Description
440	dumbbell/vacancy pair with dumbbell aligned with traversal direction
444	dumbbell/vacancy pair with dumbbell aligned with traversal direction
457A	dumbbell/vacancy pair with dumbbell perpendicular to traversal direction
457B	dumbbell/vacancy pair with dumbbell perpendicular to traversal direction
458A	2 atom collective ring mechanism
458B	3 atom ring mechanism
462	4 atom ring mechanism
468	2 atom collective ring mechanism to dumbbell
476	2 atom collective ring mechanism
476B	2 atom collective ring mechanism
489	2 atom collective ring mechanism

Table A.14: Local Point Defect Activation Energy and Volume

Identifier	Energy (eV)
440	4.402
444	4.443
457A	4.577
457B	4.577
458A	4.676
458B	4.341
462	4.568
468	4.583
476	4.676
476B	4.676
489	4.676

Identifier	Volume (Ω_0)
440	1.55
444	1.58
457A	1.65
457B	1.65
458A	1.63
458B	1.53
462	1.58
468	1.77
476	1.63
476B	1.63
489	1.63

Table A.15: Activation volume tensors for selected point defects

Point Defect ID	Activation Volume Tensor
440 (|| dumbbell)	$\begin{matrix} 0.6555 & -0.0584 & 0.5062 \\ -0.0584 & 0.6721 & 0.0334 \\ 0.5062 & 0.0334 & 0.2228 \end{matrix}$
457 ($\perp$ dumbbell)	$\begin{matrix} 0.5660 & 0 & 0 \\ 0 & 0.5713 & -0.2773 \\ 0 & -0.2773 & 0.5817 \end{matrix}$
476 (2 atom ring)	$\begin{matrix} 1.368 & -0.0007 & 0.0074 \\ -0.0007 & 0.1183 & 1.439 \\ 0.0074 & 1.439 & 0.0871 \end{matrix}$
458B (3 atom ring)	$\begin{matrix} 0.4929 & 0.0702 & -0.0768 \\ 0.0702 & 0.5058 & -0.0854 \\ -0.0768 & -0.0854 & 0.5165 \end{matrix}$
462 (4 atom ring)	$\begin{matrix} 0.7842 & -0.1016 & -0.1019 \\ -0.1016 & 0.3963 & -1.879 \\ -0.1019 & -1.879 & 0.3965 \end{matrix}$

Table A.16: Local defect second invariant of the activation volume tensor

Identifier	second invariant of the activation volume tensor
440 (|| dumbbell)	0.5707
457 ($\perp$ dumbbell)	0.2788
476 (2 atom ring)	1.6142
458B (3 atom ring)	0.1351
462 (4 atom ring)	1.8978

A.4 Σ 5 [210] Grain Boundary Transitions

Table A.17: Grain Boundary Activation Energy

Event Identifier	Activation Energy (eV)
41	0.7491
70	1.1308
77	0.7094
81	0.7935
103	1.5558
112	1.1000
126	1.1308
127	1.4515
134a	1.4348
135	1.4412
137	1.4348
137a	1.3547
138	2.5011
145	1.3547
146	0.9671
148	1.4609
150	1.4609
154	1.3547
159	1.6073
170	1.6589
177	1.5340
184	no convergence
188	1.7488
197	1.9365
206	description
212	1.9365
221	1.9613
230	no convergence
239	no convergence
242	no convergence

Table A.18: Grain boundary activation volume and second invariant of the activation volume tensor

Event Identifier	Activation Volume (Ω_0)	Second Invariant (Ω_0)
41	0.2889	1.6220
70	0.3125	0.7539
77	0.2594	1.6853
81	0.1557	1.1557
103	0.4019	3.3676
112	0.1677	2.6731
126	0.3179	0.7636
127	0.2178	no convergence
134a	0.5668	0.9468
135	0.5082	0.8327
137	0.4741	.7586
137a	1.0853	no convergence
138	1.4406	1.2726
145	0.3899	no convergence
146	0.5054	0.8385
148	0.2676	2.8807
150	0.2618	2.8628
154	0.2792	1.5679
159	0.7935	1.0798
170	0.6281	0.7928
177	0.6365	1.5509
184	no convergence	
188	1.8983	2.6904
197	0.4175	4.5235
206	0.2215	no convergence
212	0.4175	4.5235
221	0.5991	1.7548
230	no convergence	
239	no convergence	
242	no convergence	

Table A.19: Activation volume tensors, $\bar{\Omega}$, and Error

Identifier	Activation Volume Tensor (Ω_0)			Max Difference Error (Ω_0)		
41	1.309	−0.2777	−0.1947	0.0042	0.0027	0.0014
	−0.2777	−0.5407	1.188	0.0027	0.0378	0.0117
	−0.1947	1.188	−0.4794	0.0014	0.0117	0.0074
70	0.4853	−0.3874	−0.3214	0.0213	0.0068	0.0028
	−0.3874	0.3138	−0.2144	0.0068	0.0142	0.0002
	−0.3214	−0.2144	−0.4866	0.0028	0.0002	0.0138
77	−0.1124	0.3111	1.1797	0.0193	0.0055	0.0231
	0.3111	0.3446	−1.1388	0.0055	0.0089	0.0274
	1.1797	−1.1388	0.0271	0.0231	0.0274	0.0385
81	0.7139	−0.3114	0.9150	0.0111	0.0005	0.0070
	−0.3114	−0.4383	−0.2177	0.0005	0.0353	0.1690
	0.9150	−0.2177	−0.1199	0.0070	0.1690	0.0129

103	$\begin{matrix} 1.5593 & 0.1539 & 0.3086 \\ 0.1539 & 0.1183 & -3.0352 \\ 0.3086 & -3.0352 & -1.2757 \end{matrix}$	$\begin{matrix} 0.0883 & 0.0053 & 0.0450 \\ 0.0053 & 0.1035 & 0.2803 \\ 0.0450 & 0.2803 & 0.0319 \end{matrix}$
112	$\begin{matrix} 0.6076 & 0.0805 & -0.7959 \\ 0.0805 & 0.0554 & 2.3819 \\ -0.7959 & 2.3819 & -0.5084 \end{matrix}$	$\begin{matrix} 0.0138 & 0.0007 & 0.0077 \\ 0.0007 & 0.0269 & 0.0244 \\ 0.0077 & 0.0244 & 0.0217 \end{matrix}$
126	$\begin{matrix} 0.4935 & -0.4102 & -0.3232 \\ -0.4102 & 0.3143 & -0.1901 \\ -0.3232 & -0.1901 & -0.4899 \end{matrix}$	$\begin{matrix} 0.0211 & 0.0064 & 0.0026 \\ 0.0064 & 0.0142 & 0.0004 \\ 0.0026 & 0.0004 & 0.0139 \end{matrix}$
127	$\begin{matrix} 1.3112 & -0.1805 & -0.1658 \\ -0.1805 & -0.4124 & 4.0134 \\ -0.1658 & 4.0134 & -0.6810 \end{matrix}$	$\begin{matrix} 0.0257 & 0.0429 & 0.0103 \\ 0.0429 & 0.0658 & 0.1238 \\ 0.0103 & 0.1238 & 0.0469 \end{matrix}$

134a	$\begin{matrix} -0.0685 & -0.1609 & 0.2664 \\ -0.1609 & -0.3162 & -0.4868 \\ 0.2664 & -0.4868 & 1.0029 \end{matrix}$	$\begin{matrix} 0.0654 & 0.0032 & 0.0044 \\ 0.0032 & 0.0106 & 0.1426 \\ 0.0044 & 0.1426 & 0.0272 \end{matrix}$
135	$\begin{matrix} -0.2135 & -0.1408 & -0.0203 \\ -0.1408 & -0.2590 & -0.4230 \\ -0.0203 & -0.4230 & 0.9807 \end{matrix}$	$\begin{matrix} 0.0230 & 0.0006 & 0.0245 \\ 0.0006 & 0.0465 & 0.0043 \\ 0.0245 & 0.0043 & 0.1195 \end{matrix}$
137	$\begin{matrix} -0.0135 & -0.1679 & 0.0697 \\ -0.1679 & -0.3239 & -0.4408 \\ 0.0697 & -0.4408 & 0.8114 \end{matrix}$	$\begin{matrix} 0.0269 & 0.0022 & 0.0298 \\ 0.0022 & 0.0120 & 0.1065 \\ 0.0298 & 0.1065 & 0.0597 \end{matrix}$
137a	$\begin{matrix} 2.4312 & 0.4155 & -0.0640 \\ 0.4155 & -0.1137 & 8.4533 \\ -0.0640 & 8.4533 & -1.2322 \end{matrix}$	$\begin{matrix} 0.5190 & 0.0904 & 0.1281 \\ 0.0904 & 0.1736 & 0.0276 \\ 0.1281 & 0.0276 & 0.0580 \end{matrix}$

138	$\begin{matrix} -0.1733 & -0.0303 & -0.0848 \\ -0.0303 & -0.2620 & -0.3854 \\ -0.0848 & -0.3854 & 1.8758 \end{matrix}$	$\begin{matrix} 0.0427 & 0.0023 & 0.0120 \\ 0.0023 & 0.0122 & 0.0109 \\ 0.0120 & 0.0109 & 0.0429 \end{matrix}$
145	$\begin{matrix} 3.4237 & 0.9420 & -1.1556 \\ 0.9420 & -1.7773 & 7.7087 \\ -1.1556 & 7.7087 & -1.2565 \end{matrix}$	$\begin{matrix} 1.2117 & 0.1368 & 2.1061 \\ 0.1368 & 1.0660 & 0.3908 \\ 2.1061 & 0.3908 & 1.0264 \end{matrix}$
146	$\begin{matrix} 0.1071 & -0.1198 & 0.2982 \\ -0.1198 & -0.3756 & -0.5163 \\ 0.2982 & -0.5163 & 0.7739 \end{matrix}$	$\begin{matrix} 0.0937 & 0.0054 & 0.0192 \\ 0.0054 & 0.0097 & 0.2248 \\ 0.0192 & 0.2248 & 0.0077 \end{matrix}$
148	$\begin{matrix} 0.2696 & -0.0168 & -0.5481 \\ -0.0168 & 0.5123 & 2.7767 \\ -0.5481 & 2.7767 & -0.5143 \end{matrix}$	$\begin{matrix} 0.0473 & 0.0031 & 0.0339 \\ 0.0031 & 0.0399 & 0.0231 \\ 0.0339 & 0.0231 & 0.0174 \end{matrix}$

150	$\begin{matrix} 0.2419 & -0.0191 & -0.5461 \\ -0.0191 & 0.5194 & 2.7604 \\ -0.5461 & 2.7604 & -0.4995 \end{matrix}$	$\begin{matrix} 0.0516 & 0.0079 & 0.0357 \\ 0.0079 & 0.0386 & 0.0282 \\ 0.0357 & 0.0282 & 0.0166 \end{matrix}$
154	$\begin{matrix} 1.5598 & -0.3078 & -0.0903 \\ -0.3078 & -0.4707 & -0.8444 \\ -0.0903 & -0.8444 & -0.8100 \end{matrix}$	$\begin{matrix} 0.0464 & 0.0284 & 0.0080 \\ 0.0284 & 0.0398 & 0.0210 \\ 0.0080 & 0.0210 & 0.0129 \end{matrix}$
159	$\begin{matrix} -0.2183 & 0.0932 & 0.4653 \\ 0.0932 & 0.8190 & 0.8173 \\ 0.4653 & 0.8173 & 0.1927 \end{matrix}$	$\begin{matrix} 0.0174 & 0.0002 & 0.0073 \\ 0.0002 & 0.0178 & 0.0178 \\ 0.0073 & 0.0178 & 0.0146 \end{matrix}$
170	$\begin{matrix} -0.1382 & -0.0811 & 0.2185 \\ -0.0811 & 0.7253 & 0.6054 \\ 0.2185 & 0.6054 & 0.0410 \end{matrix}$	$\begin{matrix} 0.0112 & 0.0019 & 0.0026 \\ 0.0019 & 0.0242 & 0.0133 \\ 0.0026 & 0.0133 & 0.0372 \end{matrix}$

177	$\begin{matrix} 1.3026 & 0.0787 & -1.0900 \\ 0.0787 & 0.1731 & 0.2512 \\ -1.0900 & 0.2512 & -0.8392 \end{matrix}$	$\begin{matrix} 0.0113 & 0.0199 & 0.0041 \\ 0.0199 & 0.1656 & 0.0696 \\ 0.0041 & 0.0696 & 0.0871 \end{matrix}$
188	$\begin{matrix} 1.6687 & -0.2610 & -0.3533 \\ -0.2610 & -0.7064 & 2.3593 \\ -0.3533 & 2.3593 & 0.9360 \end{matrix}$	$\begin{matrix} 0.0474 & 0.0210 & 0.0760 \\ 0.0210 & 0.0590 & 0.1693 \\ 0.0760 & 0.1693 & 0.2713 \end{matrix}$
197	$\begin{matrix} 1.5334 & -0.0858 & 0.1744 \\ -0.0858 & 0.4808 & 4.2293 \\ 0.1744 & 4.2293 & -1.5967 \end{matrix}$	$\begin{matrix} 0.1490 & 0.0083 & 0.0078 \\ 0.0083 & 0.1190 & 0.0091 \\ 0.0078 & 0.0091 & 0.1713 \end{matrix}$
206	$\begin{matrix} 1.0796 & -0.5141 & 0.7133 \\ -0.5141 & -0.1489 & -1.4137 \\ 0.7133 & -1.4137 & -0.7093 \end{matrix}$	$\begin{matrix} 0.0294 & 0.0002 & 0.0312 \\ 0.0002 & 0.0370 & 0.0140 \\ 0.0312 & 0.0140 & 0.0096 \end{matrix}$

221	$\begin{matrix} 1.5522 & -0.0603 & -0.0032 \\ -0.0603 & 0.5978 & -0.7412 \\ -0.0032 & -0.7412 & -1.5510 \end{matrix}$	$\begin{matrix} 0.1579 & 0.0128 & 0.0064 \\ 0.0128 & 0.1261 & 0.0573 \\ 0.0064 & 0.0573 & 0.1845 \end{matrix}$
242	$\begin{matrix} 0.3868 & -0.1808 & -2.5075 \\ -0.1808 & 0.2429 & 1.5867 \\ -2.5075 & 1.5867 & -3.7460 \end{matrix}$	$\begin{matrix} 0.0607 & 0.3187 & 4.7312 \\ 0.3187 & 0.1789 & 3.1734 \\ 4.7312 & 3.1734 & 6.7750 \end{matrix}$

Appendix B

Figures of Atomic Configurations and Direction Distributions

This appendix is dedicated to useful reference figures of atomic configurations at the saddle point of the transitions and projected hemisphere plots of the direction distributions. The configuration plots are useful in understanding the physical nature of the mechanism and visualize the important directions within the kinetic transition itself. The direction distribution plots are projections of a hemisphere in the positive Z quadrant for the directions of uniaxial applied stress used in calculating the activation volume tensor. Each of the circles is a singular direction colored based on the magnitude of the directional activation volume scalar, v', in that given direction. The stars on the plot indicate a projection of the principal directions of the activation volume tensor, similarly colored by magnitude as measured in atomic volumes for the given material.

B.1 Vacancy Migration in FCC Copper

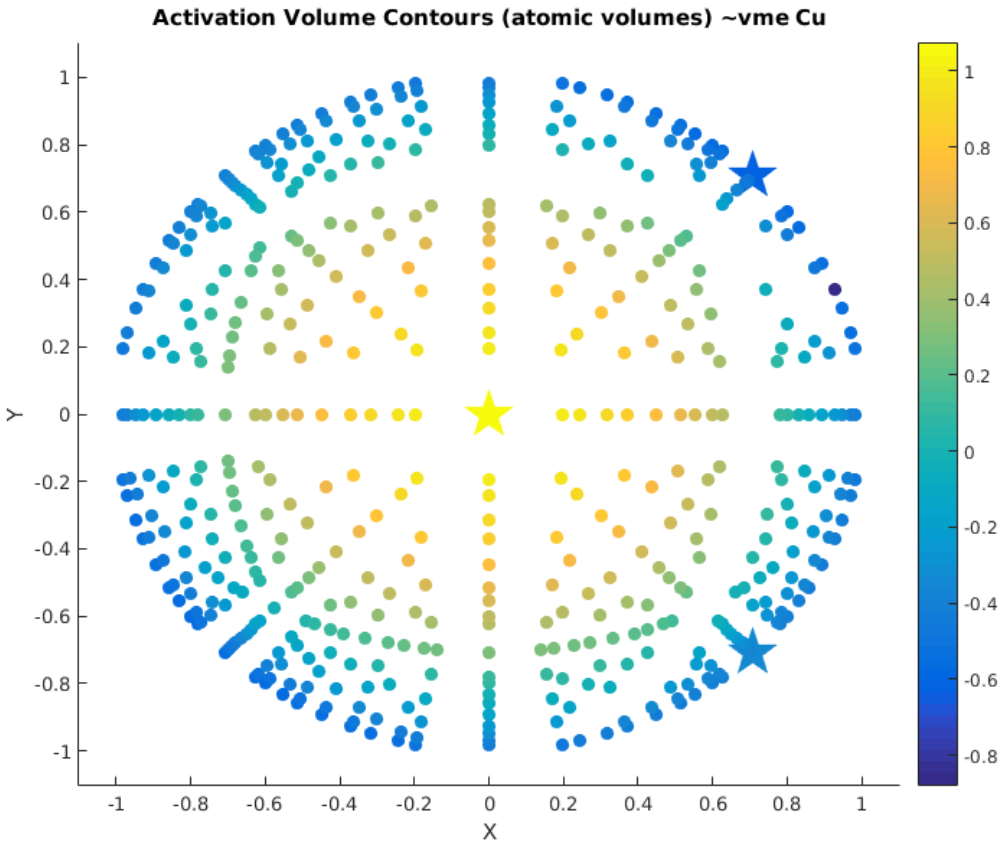

Figure B-1: Vacancy Migration in Copper

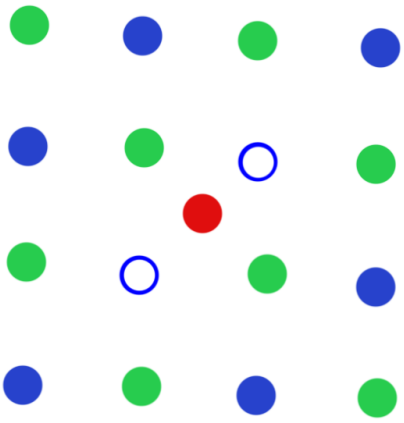

Figure B-2: Vacancy Migration in Copper

B.2 Vacancy Migration in HCP Titanium

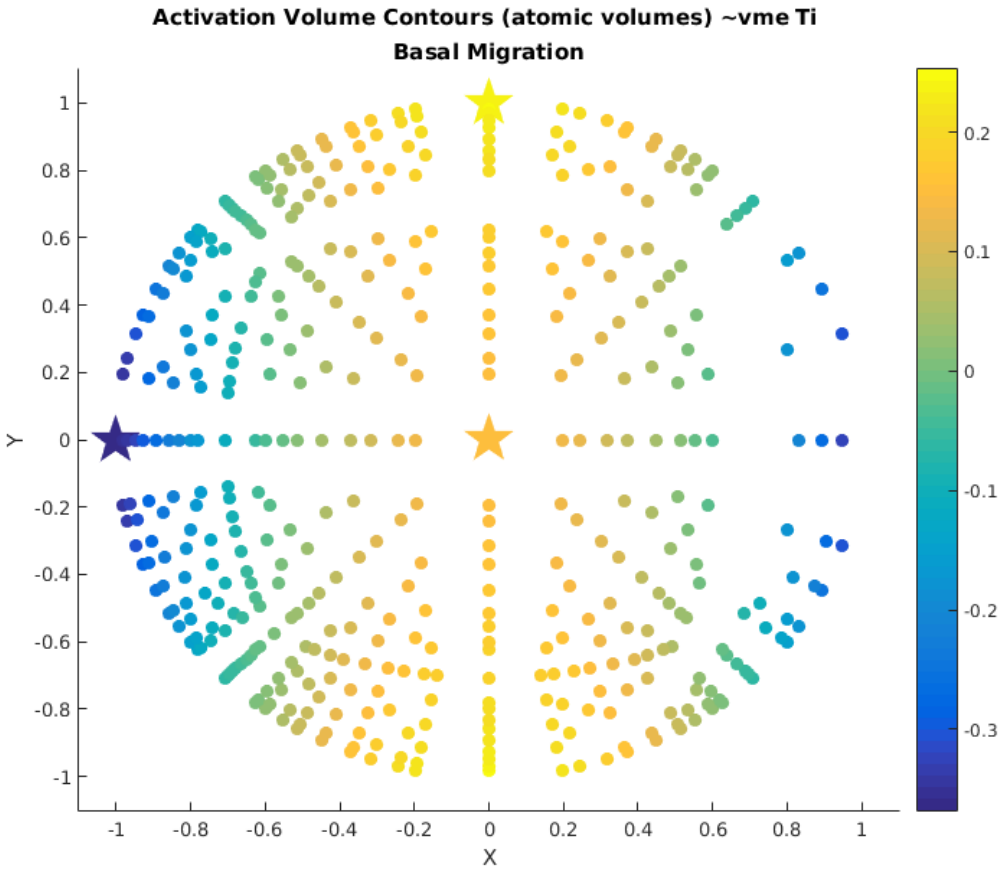

Figure B-3: Basal Vacancy Migration in Titanium

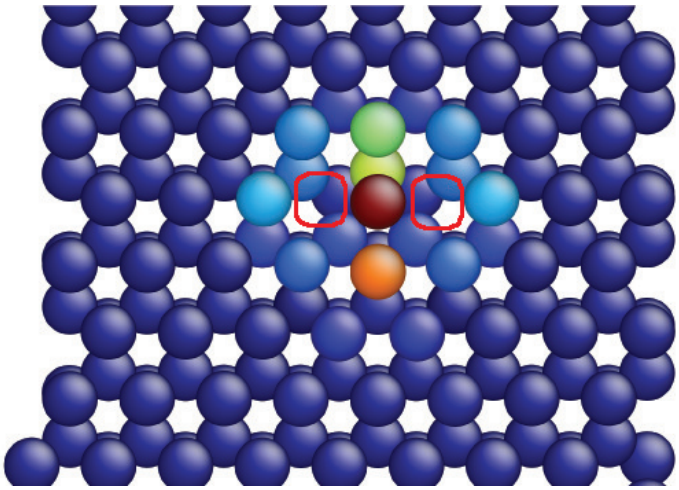

Figure B-4: Basal Vacancy Migration in Titanium

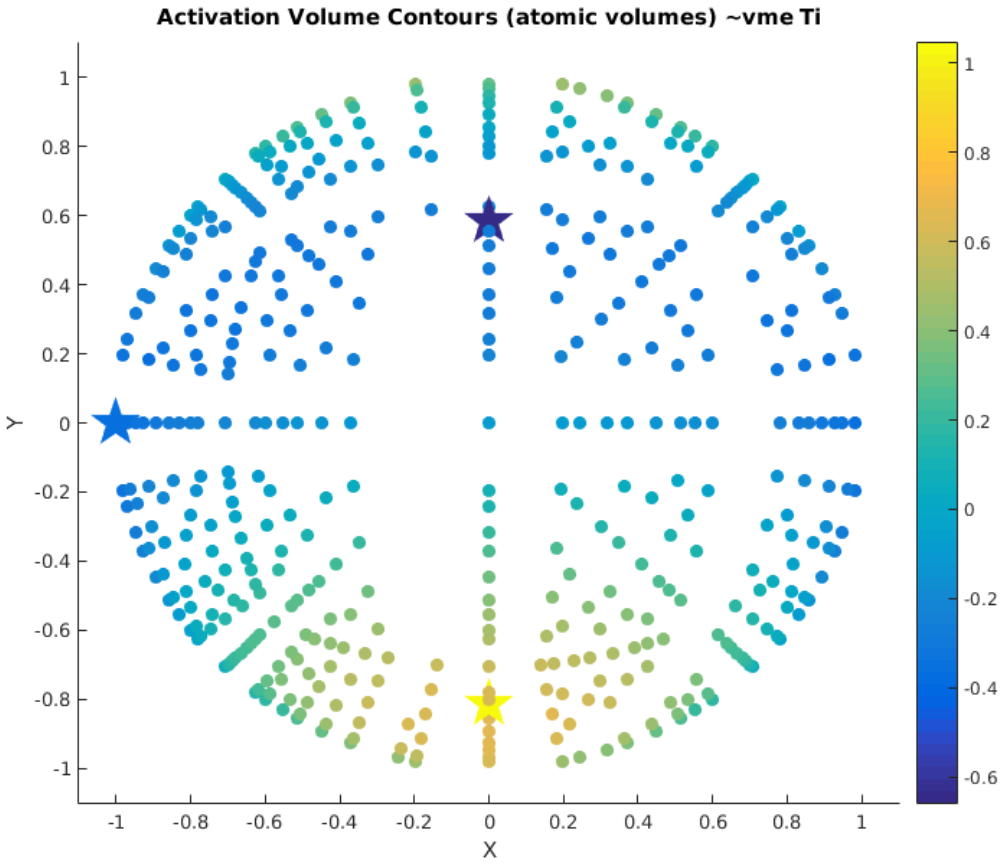

Figure B-5: Non-Basal Vacancy Migration in Titanium

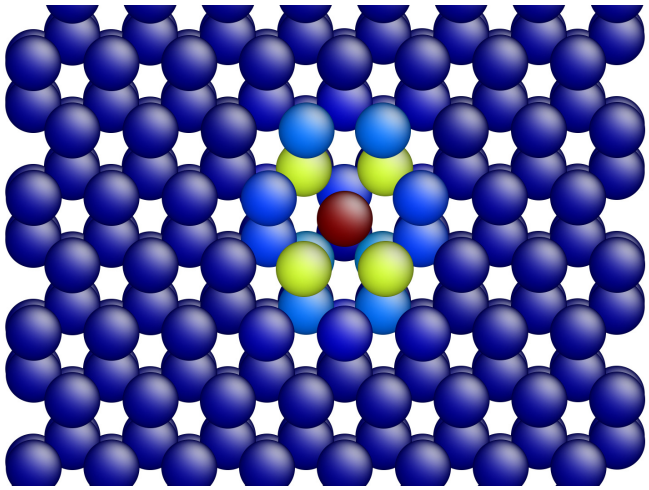

Figure B-6: Non-Basal Vacancy Migration in Titanium

B.3 Point Defects

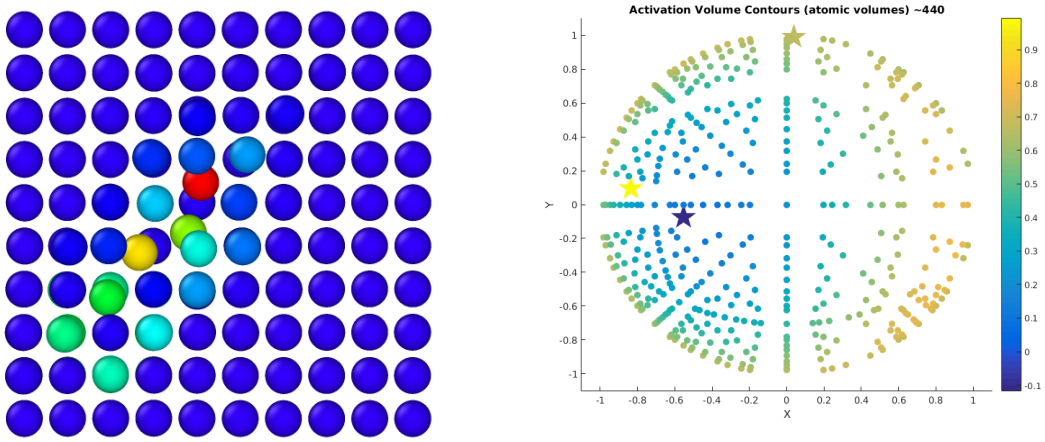

(a) Transition (b) Direction Hemisphere

Figure B-7: Parallel Dumbbell - Vacancy Creation Mechanism (440)

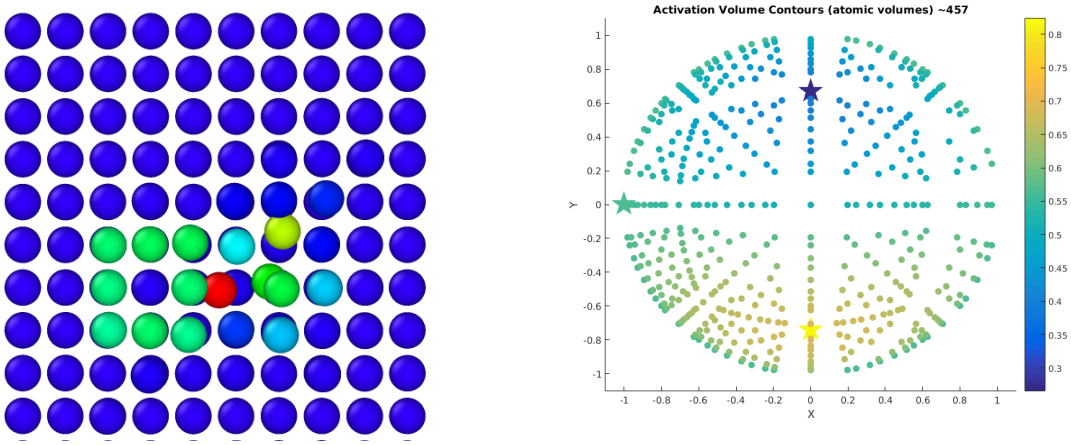

(a) Transition (b) Direction Hemisphere

Figure B-8: Perpendicular Dumbbell - Vacancy Creation Mechanism (457)

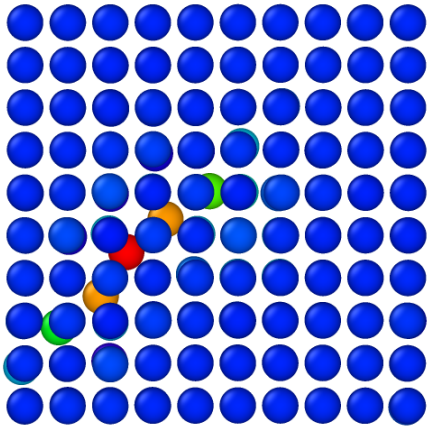

(a) Transition

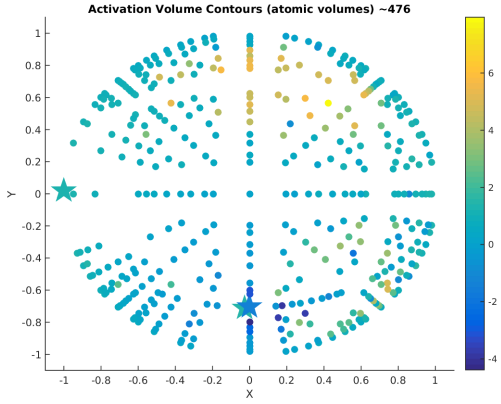

(b) Direction Hemisphere

Figure B-9: 2 atom ring Mechanism (476)

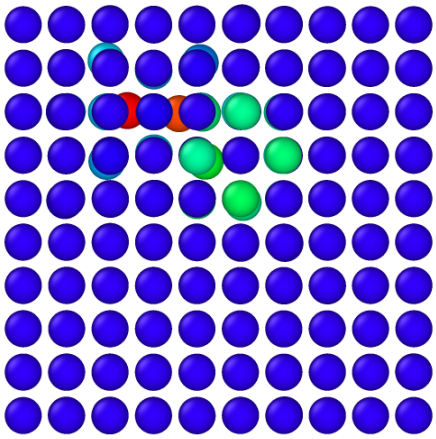

(a) Transition

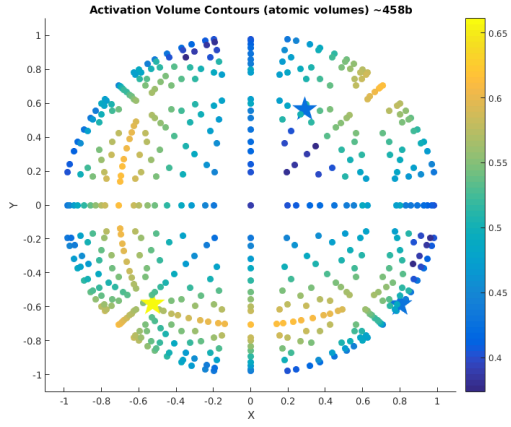

(b) Direction Hemisphere

Figure B-10: 3 atom ring Mechanism (458)

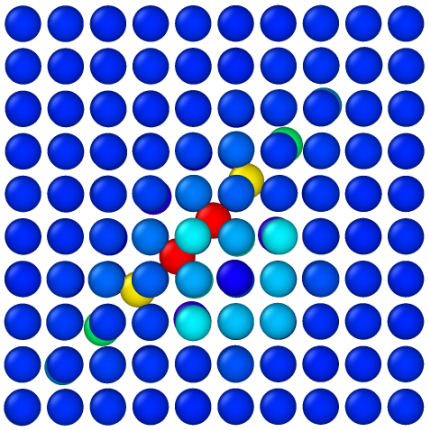

(a) Transition

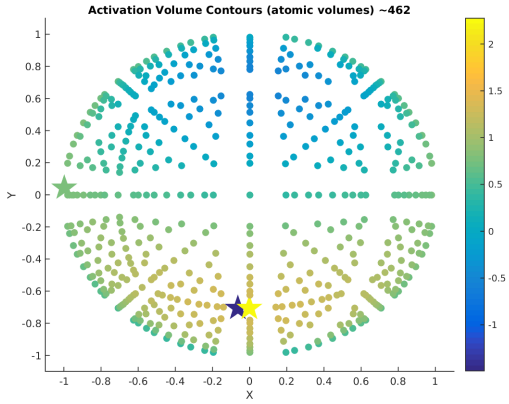

(b) Direction Hemisphere

Figure B-11: 4 atom ring Mechanism (462)

B.4 Grain Boundary Kinetic Transitions

The grain boundary transitions are generated using the OVITO visualization software. [**?**]. They are plotted looking down the Z-axis at the grain boundary plane with slices with a (0,0,1) normal direction at distances of 6 and -0.5. The atom coloring is based on displacement from the inital configuration state. There are two periods in the X and Y directions in order to show the movement of atoms across the periodic boundaries.

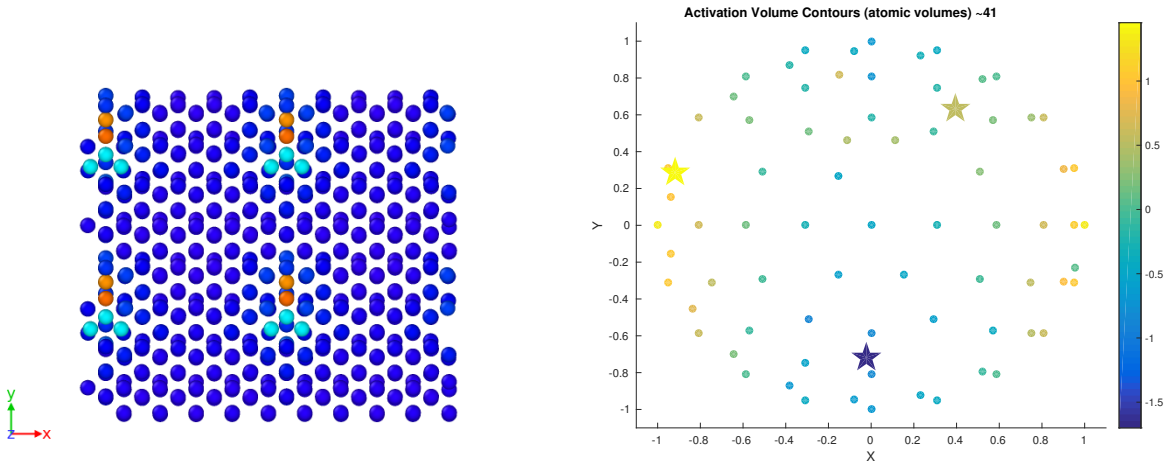

(a) GB 41 Transition

(b) GB 41 Direction Hemisphere

Figure B-12: GB Kinetic Event 41

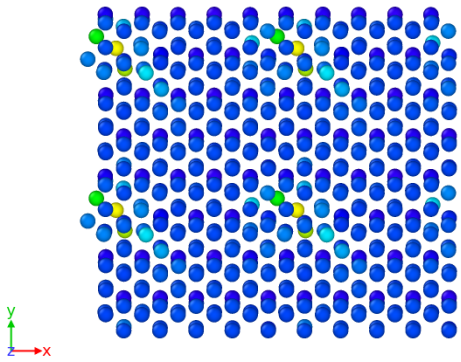

(a) GB 70 Transition

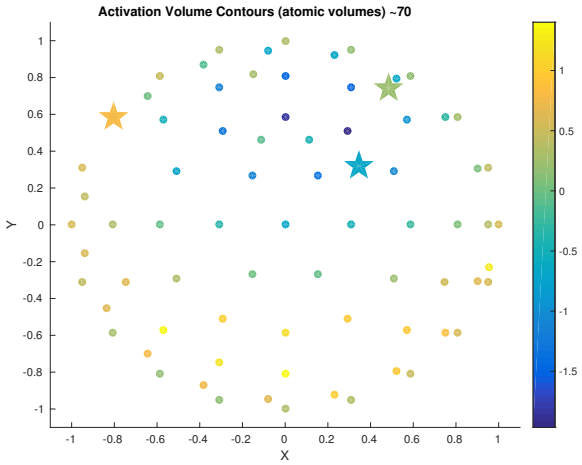

(b) GB 70 Direction Hemisphere

Figure B-13: GB Kinetic Event 70

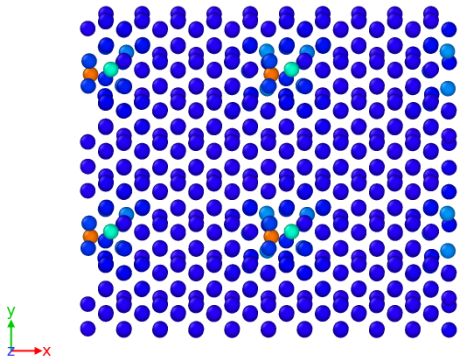

(a) GB 77 Transition

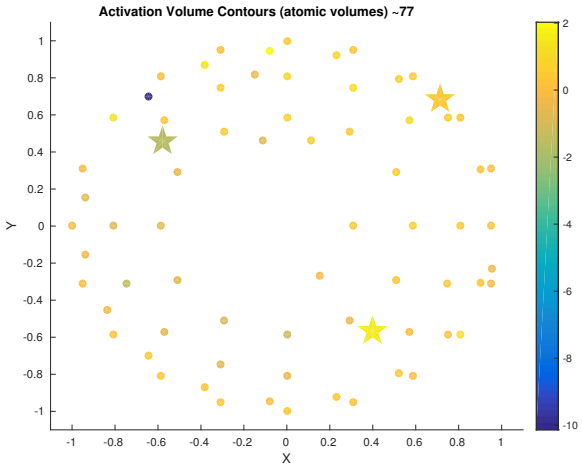

(b) GB 77 Direction Hemisphere

Figure B-14: GB Kinetic Event 77

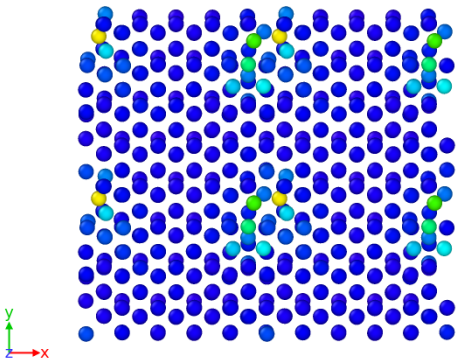

(a) GB 81 Transition

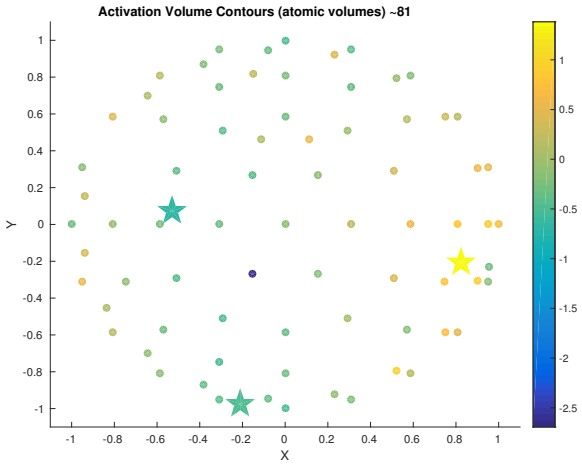

(b) GB 81 Direction Hemisphere

Figure B-15: GB Kinetic Event 81

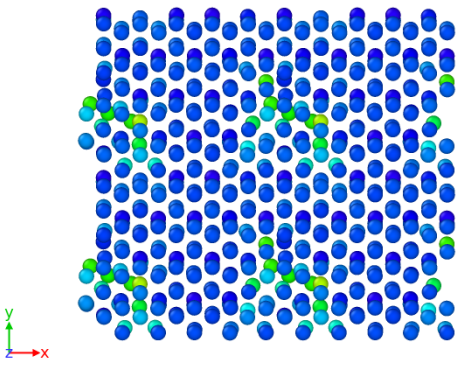

(a) GB 103 Transition

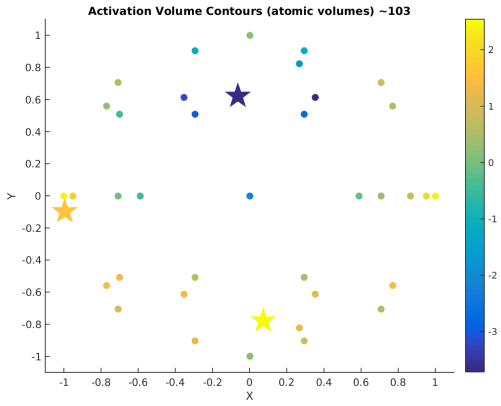

(b) GB 103 Direction Hemisphere

Figure B-16: GB Kinetic Event 103

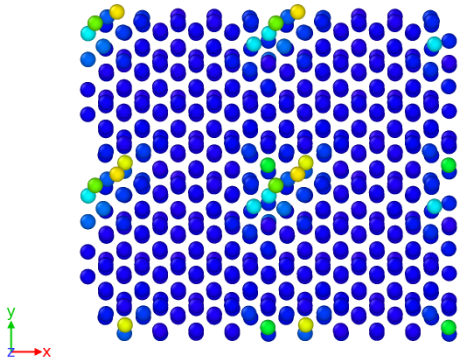

(a) GB 112 Transition

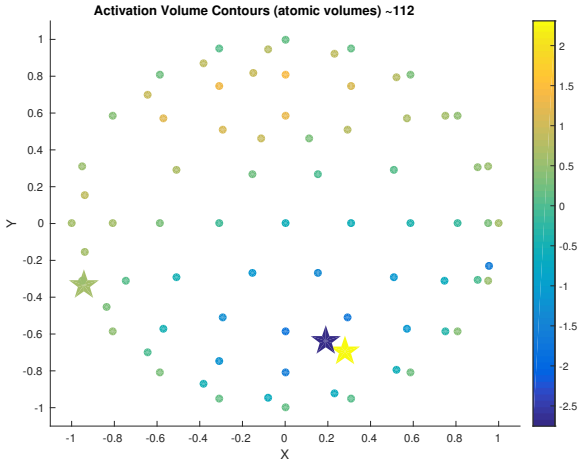

(b) GB 12 Direction Hemisphere

Figure B-17: GB Kinetic Event 112

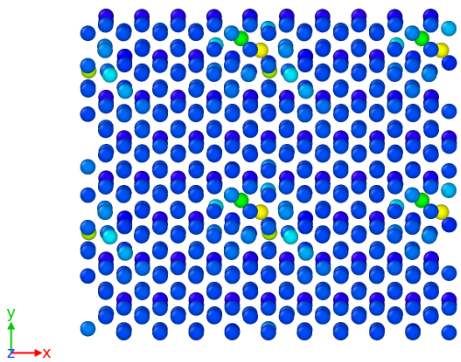

(a) GB 126 Transition

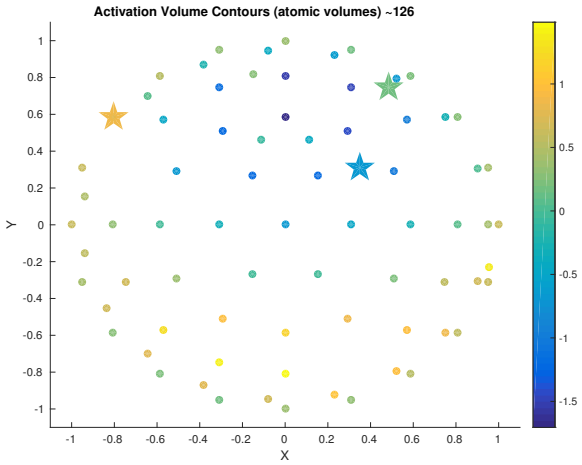

(b) GB 126 Direction Hemisphere

Figure B-18: GB Kinetic Event 126

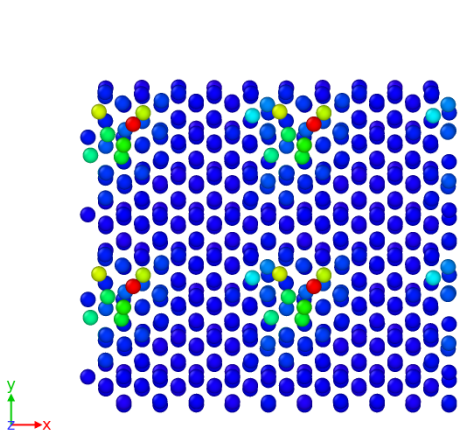

(a) GB 127 Transition

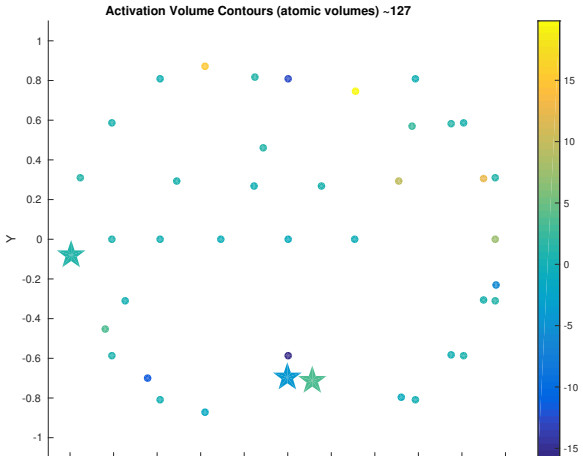

(b) GB 127 Direction Hemisphere

Figure B-19: GB Kinetic Event 127

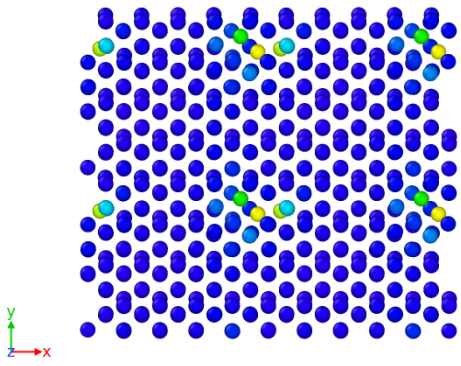

(a) GB 134a Transition

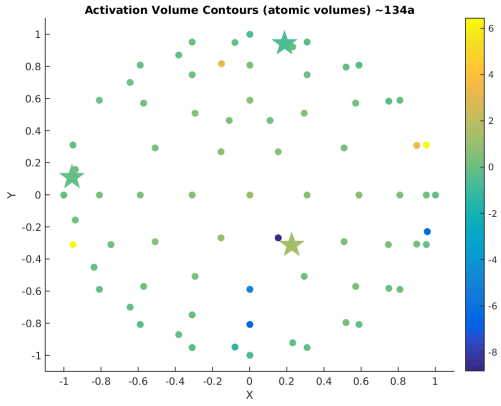

(b) GB 134a Direction Hemisphere

Figure B-20: GB Kinetic Event 134a

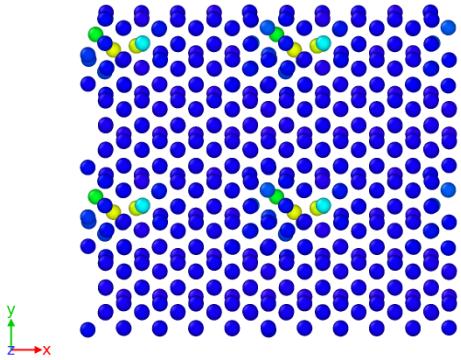

(a) GB 135 Transition

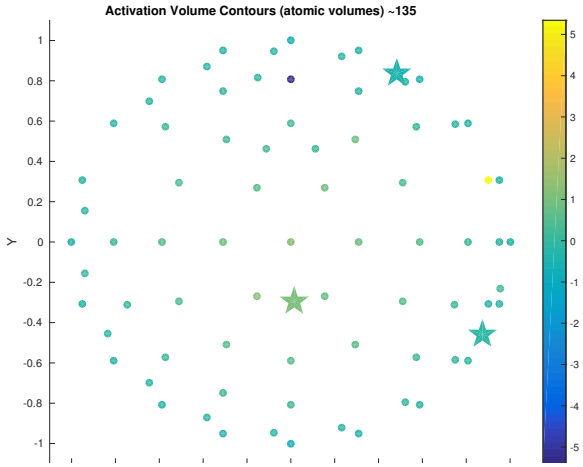

(b) GB 135 Direction Hemisphere

Figure B-21: GB Kinetic Event 135

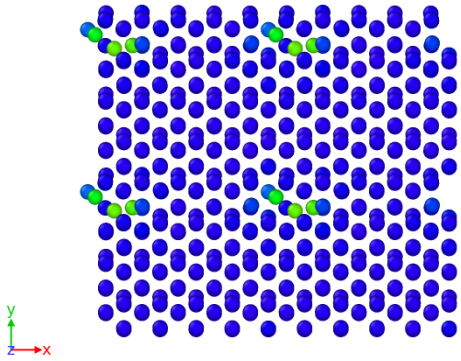

(a) GB 137 Transition

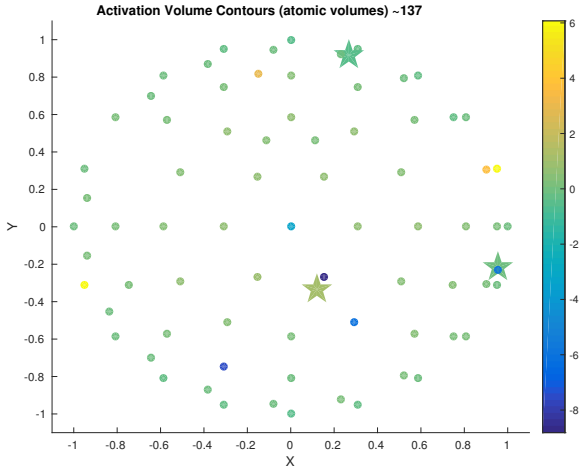

(b) GB 137 Direction Hemisphere

Figure B-22: GB Kinetic Event 137

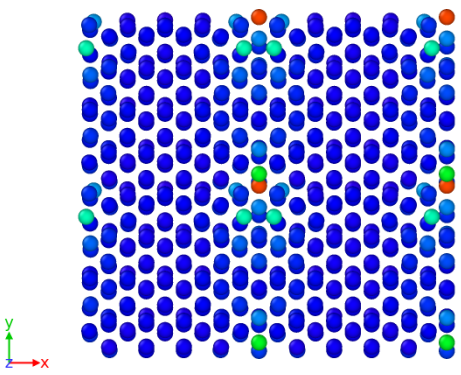

(a) GB 137a Transition

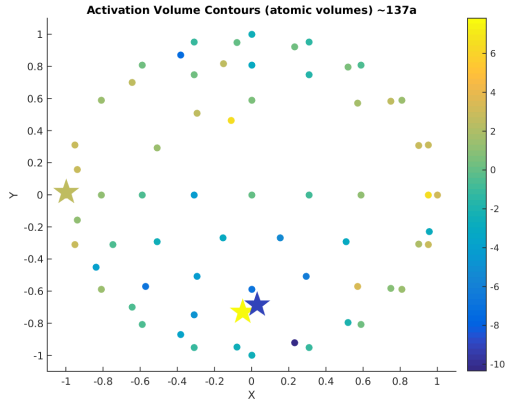

(b) GB 137a Direction Hemisphere

Figure B-23: GB Kinetic Event 137a

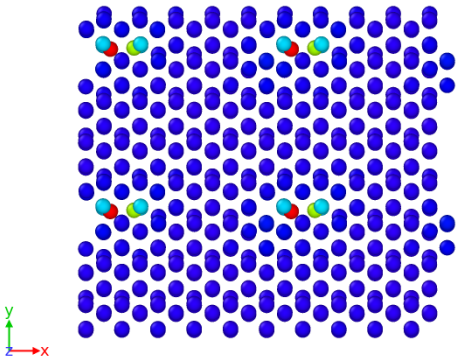

(a) GB 138 Transition

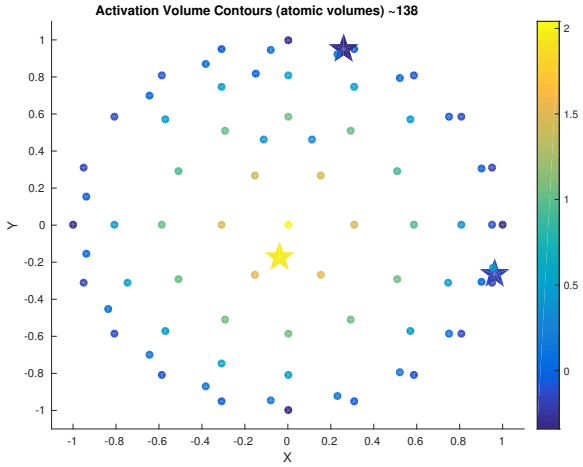

(b) GB 138 Direction Hemisphere

Figure B-24: GB Kinetic Event 138

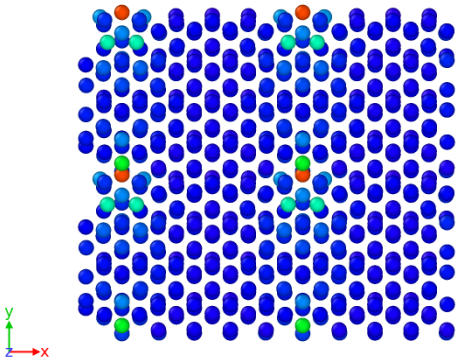

(a) GB 145 Transition

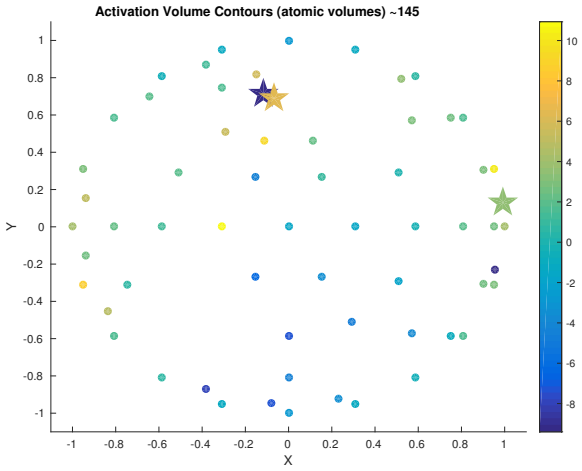

(b) GB 145 Direction Hemisphere

Figure B-25: GB Kinetic Event 145

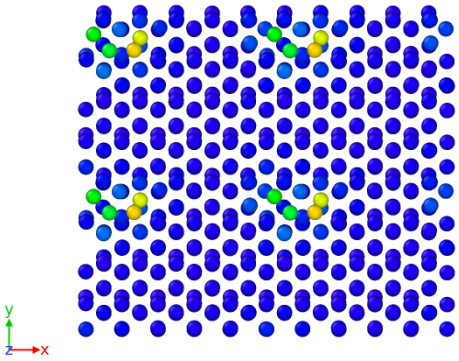

(a) GB 146 Transition

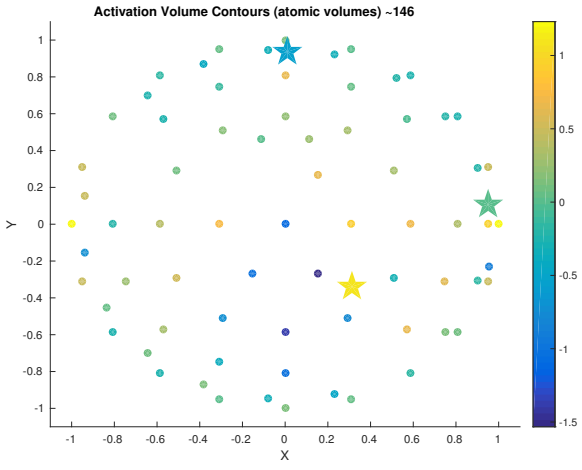

(b) GB 146 Direction Hemisphere

Figure B-26: GB Kinetic Event 146

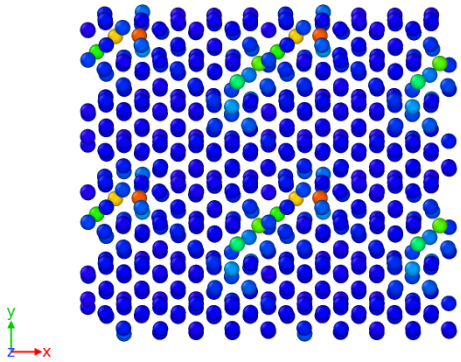

(a) GB 148 Transition

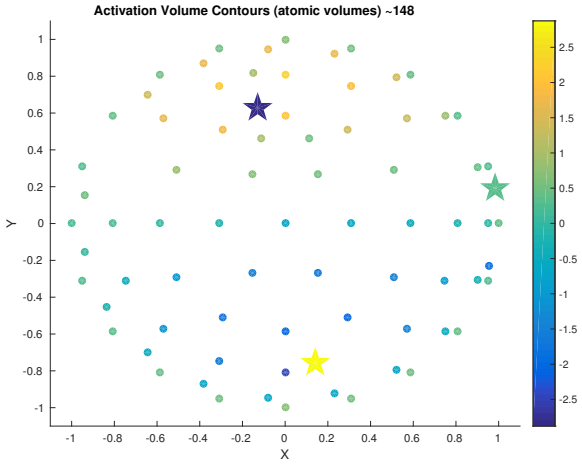

(b) GB 148 Direction Hemisphere

Figure B-27: GB Kinetic Event 148

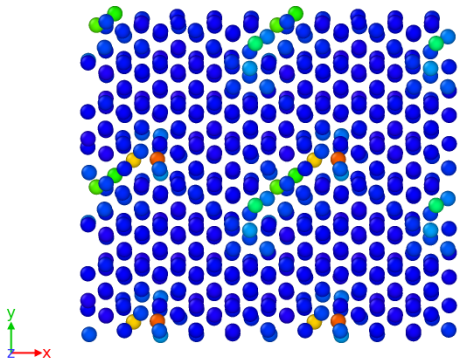

(a) GB 150 Transition

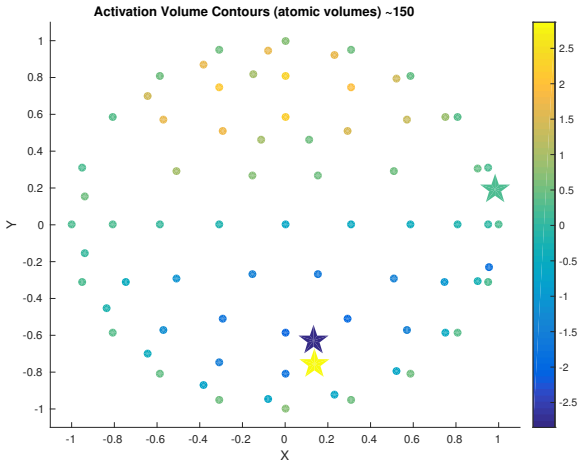

(b) GB 150 Direction Hemisphere

Figure B-28: GB Kinetic Event 150

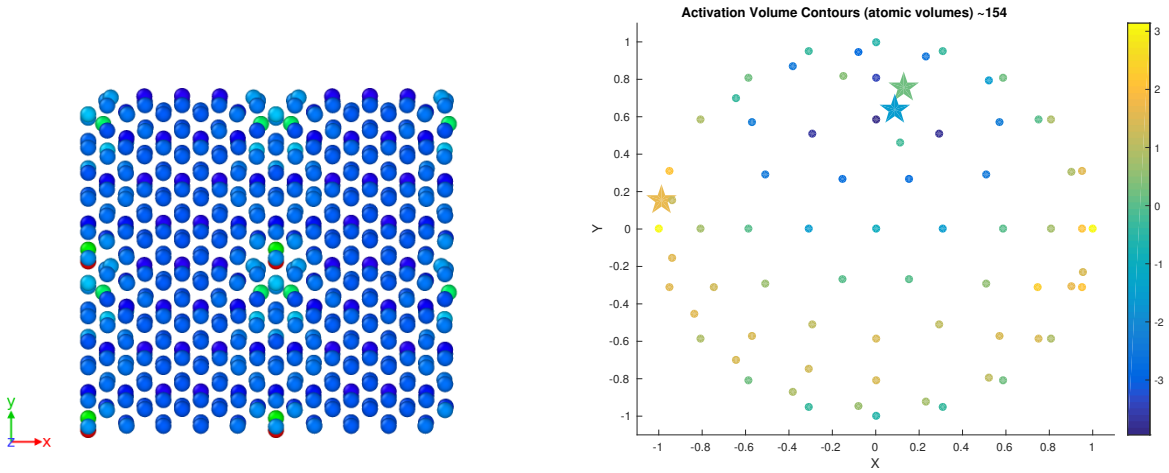

(a) GB 154 Transition

(b) GB 154 Direction Hemisphere

Figure B-29: GB Kinetic Event 154

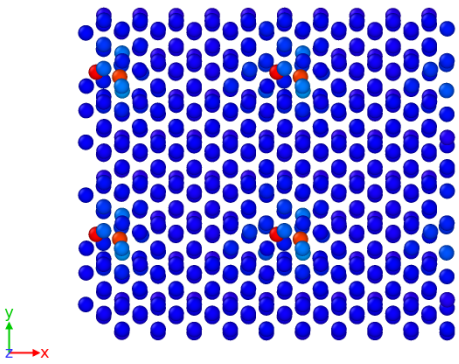

(a) GB 159 Transition

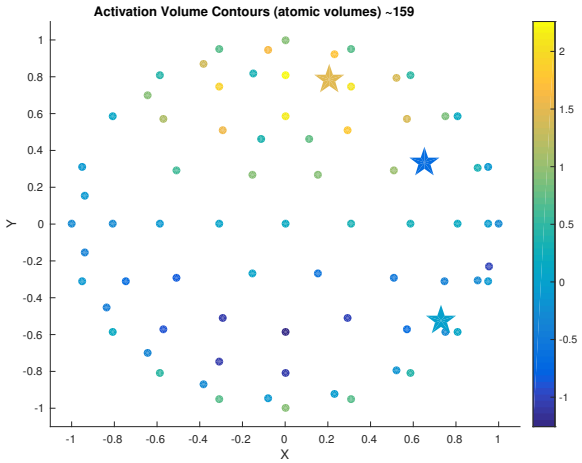

(b) GB 159 Direction Hemisphere

Figure B-30: GB Kinetic Event 159

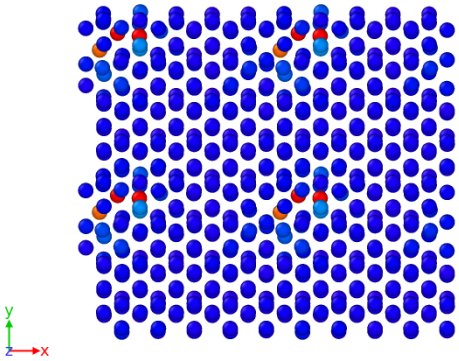

(a) GB 170 Transition

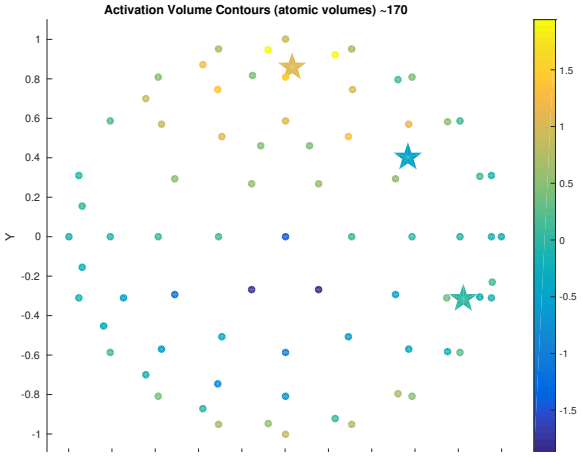

(b) GB 170 Direction Hemisphere

Figure B-31: GB Kinetic Event 170

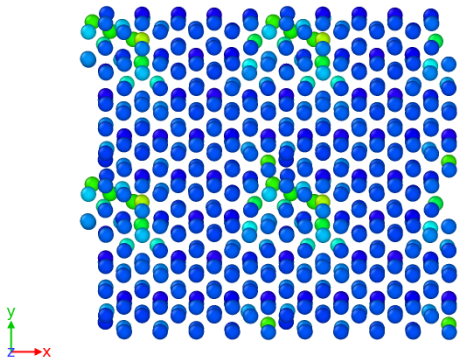

(a) GB 177 Transition

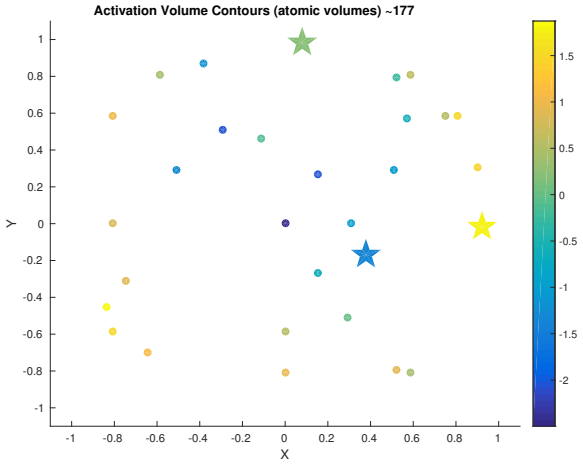

(b) GB 177 Direction Hemisphere

Figure B-32: GB Kinetic Event 177

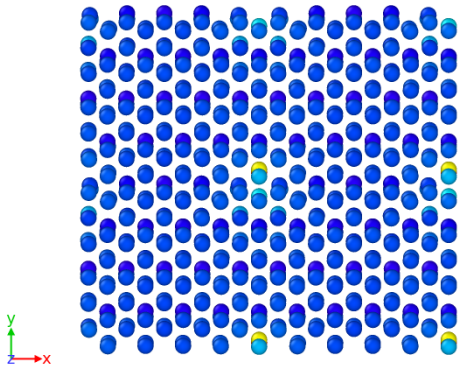

(a) GB 188 Transition

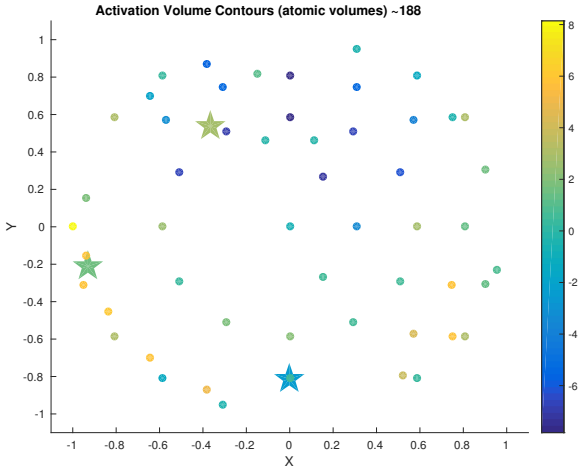

(b) GB 188 Direction Hemisphere

Figure B-33: GB Kinetic Event 188

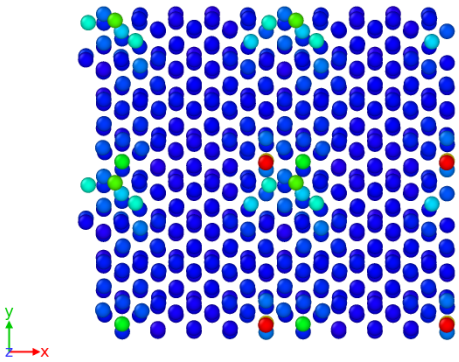

(a) GB 197 Transition

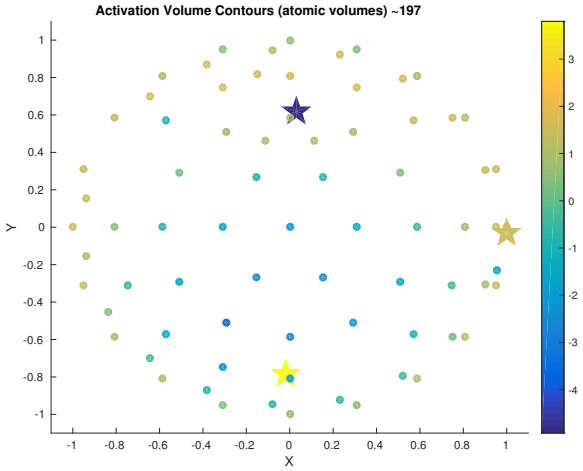

(b) GB 197 Direction Hemisphere

Figure B-34: GB Kinetic Event 197

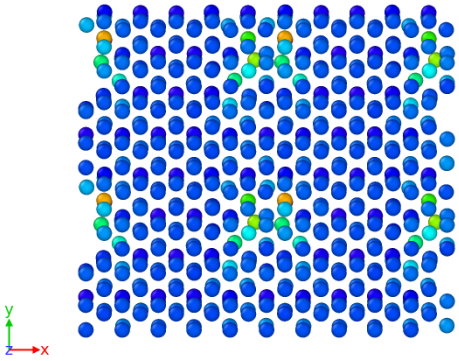

(a) GB 221 Transition

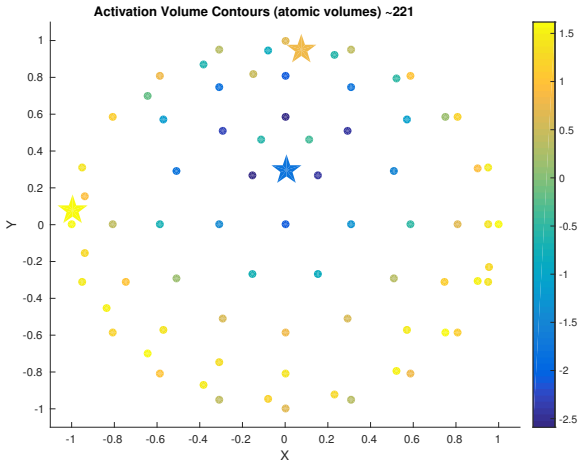

(b) GB 221 Direction Hemisphere

Figure B-35: GB Kinetic Event 221

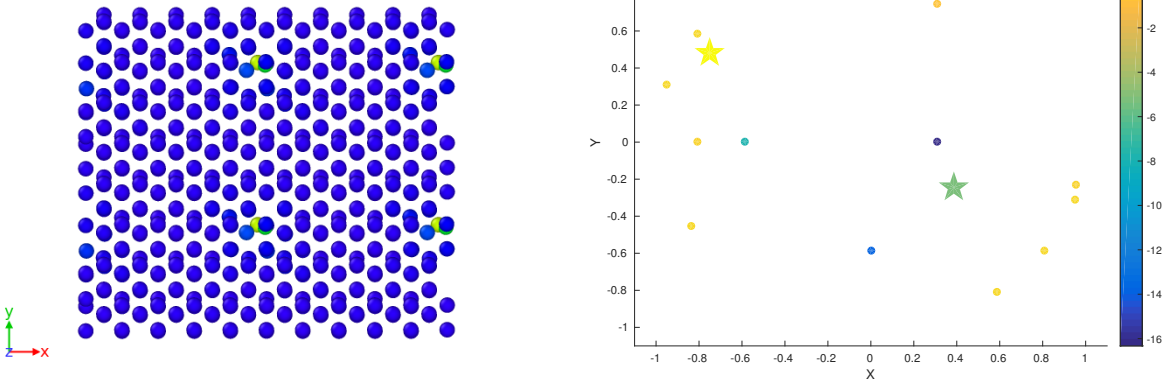

(a) GB 242 Transition

(b) GB 242 Direction Hemisphere

Figure B-36: GB Kinetic Event 242

Appendix C

LAMMPS input files

C.1 Vacancy Creation and Migration

The following section describes how a vacancy in copper is created and moved in order to create the initial and final states that are then used as inputs to the nudged elastic band file.

```
# Input file for Vacancy Migration Energy in Ti
# with zero applied pressure

# --------------- INITIALIZATION ------------------
clear
units metal
dimension 3
boundary p p    p
atom_style atomic
atom_modify     map array sort 0 0.0

# ------------------ ATOM DEFINITION -------------------
```

```
variable ao equal 2.9575
lattice         hcp 2.9575
region     simbox block -4 4 -4 4 -4 4
create_box     1 simbox
lattice      hcp 2.9575  origin 0 0 0
create_atoms     1 region simbox

# ------------------------ FORCE FIELDS ----------------------
pair_style    eam/alloy
pair_coeff * * Zope-Ti_Al-2003.eam.alloy Ti
#neighbor 2.0 bin
#neigh_modify delay 10 check yes

#---------------------------Settings----------------------------
compute csym all centro/atom fcc
compute eng all pe/atom
compute eatoms all reduce sum c_eng
compute atomstress all stress/atom NULL

#----------------------Run Minimization-------------------------
reset_timestep    0
thermo 100
thermo_style custom step pe lx ly lz press pxx pyy pzz c_eatoms
dump 1 all cfg 1000 dump.relax.*.cfg mass type xs ys zs id c_csym c_eng
min_style cg
minimize 1e-15 1e-15 5000 5000
minimize 1e-15 1e-15 5000 5000

#----------------------Pressure-------------------------------
#external pressure in bar
```

```
variable pres equal 0
#Apply pressure
fix fxp all box/relax iso ${pres}

#--------------------Phase 1 ---------------------------
# Vacancy Creation at (ao, 0, 0)
#r2 is the radius of the copper atom
variable r2 equal (${ao})/2
region select sphere ${ao} 0 0 ${r2} units box
delete_atoms region select compress yes

# Relax Atoms to lowest energy state
reset_timestep 0
dump L1p1 all cfg 5000 dump.p1.*.cfg mass type xs ys zs c_csym c_eng
#Relaxation of moving atom to initial NEB location
minimize 1e-15 1e-15 5000 5000
minimize 1e-15 1e-15 5000 5000
undump L1p1

## Store the positions  with the vacancy in position NEB final
write_dump all custom  final.txt id type x y z fx fy fz c_csym c_eng
unfix fxp
minimize 1e-15 1e-15 5000 5000
minimize 1e-15 1e-15 5000 5000
#-----------------Phase 2---------------------------
##  Move the atom to position NEB start (0, 0, 0)
region rmv1 sphere  0 0 0 ${r2} units box
group mv1 region rmv1
displace_atoms mv1 move ${ao} 0 0 units box
```

```
#Relax the atoms in the NEB initial position
reset_timestep 0
dump L1p2 all cfg 5000 dump.p2.*.cfg mass type xs ys zs c_csym c_eng
minimize 1e-15 1e-15 5000 5000
minimize 1e-15 1e-15 5000 5000
undump L1p2
write_dump all custom  initial.txt id type x y z fx fy fz c_csym c_eng

#variable Enebi equal "c_eatoms" computes the final energy of the cell
# system after the vacancy is in pos NEB initial
variable Enebi equal "c_eatoms"
```

C.2 Nudged Elastic Band for Known Configurations

When initial and final states are known, from LAMMPS or ART, the nudged elastic band method is used to find the activation energy. It should be noted that if the atomic configurations are coming from art, they must first be sorted such that the atomic numbering in the initial and final states match. Once this is complete are first relaxed under a given pressure state using the fix box/relax and the conjugant gradient method. These sorted and relaxed states are then used as inputs to the neb .in file as follows:

```
# Input file for Grain Boundary Transition Activation Energy in Cu
# with given applied pressure

# --------------- INITIALIZATION ------------------
clear
units metal
dimension 3
```

```
boundary p p    p
atom_style atomic
atom_modify     map array sort 0 0.0

# ------------------ ATOM DEFINITION -------------------
variable ao equal 3.615
lattice         fcc 3.615
region     simbox prism -4 4 -4 4 -4 4 0 0 0 units box
create_box     2 simbox

#create atom to fix a segmentation fault
#create_atoms    1 single 1.0 1.0 1.0

# read data from dump file
read_dump p_out.atom.initial 0 x y z box yes purge yes add yes replace no

# ------------------------ FORCE FIELDS -----------------------
pair_style    eam/alloy
pair_coeff * * Cu01.eam.alloy Cu Cu
neighbor 2.0 bin
neigh_modify delay 10 check yes

#----------------------------Computes-----------------------------
compute csym all centro/atom fcc
compute eng all pe/atom
compute eatoms all reduce sum c_eng

#-----------------------Pressure-------------------------------
#external pressure in bar
variable pres equal 500
```

```
variable Sx equal ${pres}/2
variable Sy equal ${pres}/2
variable Sz equal 0
variable Syz equal 0
variable Sxz equal 0
variable Sxy equal -${pres}/2
#Apply pressure
fix fxp1 all box/relax x ${Sx}
fix fxp2 all box/relax y ${Sy}
fix fxp3 all box/relax z ${Sz}
fix fxp4 all box/relax yz ${Syz}
fix fxp5 all box/relax xz ${Sxz}
fix fxp6 all box/relax xy ${Sxy}

#----------------------Energy Minimization-------------------------
reset_timestep    0
thermo 1000
thermo_style custom step pe lx ly lz press pxx pyy pzz c_eatoms
dump 1 all cfg 100 dump.initial.*.cfg mass type xs ys zs id c_csym c_eng
min_style cg
minimize 1e-15 1e-15 5000 5000
minimize 1e-15 1e-15 5000 5000
undump 1
unfix fxp1
unfix fxp2
unfix fxp3
unfix fxp4
unfix fxp5
unfix fxp6
```

```
#counts the total number of atoms in the cell
variable N equal count(all)
variable No equal $N

#variable Ei equal "c_eatoms" computes the initial energy of the
#cell system before the vacancy
variable E equal "c_eatoms"
variable Ei equal $E
print "Initial Energy energy = ${Ei}"

#-----------------------NEB-----------------------
reset_timestep   0
timestep       0.01
thermo 1000
variable A uloop 24 pad #run this job with 16 processors
dump 3 all cfg 10000 dump.NEB.${A}.*.cfg mass type xs ys zs  c_csym c_eng
fix fx1 all neb 5
min_style  quickmin
neb 1.0e-15 5.0e-9 300000 300000 10000 final p_out.atom.final

#--------------------Compute & Show-----------------
variable E equal "c_eatoms"
print "Final energy = ${E}"
variable N equal count(all)
variable EAtot equal $E/$N
print "Total Energy Per Atom = ${EAtot}"
```

Bibliography

[1] D.A. Porter and K.E. Easterling. *Phase transformations in metals and alloys*. CRC Press, Boca Raton, 2 edition, 1992.

[2] Helmut Mehrer. Diffusion in solids: fundamentals, methods, materials, diffusion-controlled processes. *Springer series in solid-state sciences*, pages —-, 2007.

[3] Robert W. Balluffi, Samuel M. Allen, and W. Craig Carter. *Kinetics of Materials*. 2005.

[4] Michael J Aziz. Questions and Answers on the Activation Strain. 321(001):449–459, 1994.

[5] Michael J. Aziz. Thermodynamics of diffusion under pressure and stress: Relation to point defect mechanisms. *Applied Physics Letters*, 70(21):2810, 1997.

[6] Michael J. Aziz, Yuechao Zhao, Hans J. Gossmann, Salman Mitha, Stephen P. Smith, and David Schiferl. Pressure and stress effects on the diffusion of B and Sb in Si and Si-Ge alloys. *Physical Review B - Condensed Matter and Materials Physics*, 73(5):1–20, 2006.

[7] Robert W. Keyes. Volumes of Activation for Diffusion in Solids. *The Journal of Chemical Physics*, 29(3):467–475, 1958.

[8] Murray Daw, Wolfgang Windl, Neil Carlson, Matt Laudon, and Michael Masquelier. Effect of stress on dopant and defect diffusion in Si: A general treatment. *Physical Review B*, 64(4):045205, 2001.

[9] Michael J. Aziz, Paul C Sabin, and Guo-quan Lu. The activation strain tensor: Nonhydrostatic stress effects on crystal growth kinetics. *Physical Review B*, 44(18):9812–9816, 1991.

[10] Ting Zhu and Ju Li. Ultra-strength materials. *Progress in Materials Science*, 55(7):710–757, sep 2010.

[11] Ju Li. Atomistic calculation of internal stress. pages 773–792, 2005.

[12] P. H. Dederichs and K. Schroeder. Anisotropic diffusion in stress fields. *Physical Review B*, 17(6):2524–2536, 1978.

[13] P. Lin, G. Palumbo, U. Erb, and K.T. Aust. Influence of grain boundary character distribution on sensitization and intergranular corrosion of alloy 600. *Scripta Metallurgica et materialia*, 33(9):1387–1392, 1995.

[14] E.M. Lehockey, G. Palumbo, and P. Lin. Grain boundary structure effects on cold work embrittlement of microalloyed steels. *Scripta Materialia*, 39(3):353–358, jul 1998.

[15] G Palumbo, P Linlp, and A M Brennenstuhl. On the Relationship Between Grain Boundary Character Distribution and Intergranular Corrosion. *Scripta Materialia*, 36(10):1211–1218, 1997.

[16] G. Palumbo, E. M. Lehockey, and P. Lin. Applications for Grain Boundary Engineered Materials. *JOM*, 50(2):40–43, feb 1998.

[17] Siyan Wang and Jianqiu Wang. Effect of grain orientation on the corrosion behavior of polycrystalline Alloy 690. *Corrosion Science*, 85:183–192, aug 2014.

[18] V.Y. Gertsman and S.M. Bruemmer. Study of grain boundary character along intergranular stress corrosion crack paths in austenitic alloys. *Acta Materialia*, 49(9):1589–1598, may 2001.

[19] M.A. Arafin and J.A. Szpunar. A new understanding of intergranular stress corrosion cracking resistance of pipeline steel through grain boundary character and crystallographic texture studies. *Corrosion Science*, 51(1):119–128, jan 2009.

[20] Liang Wan and Ju Li. Shear responses of [-1 1 0] -tilt {1 1 5}/{1 1 1} asymmetric tilt grain boundaries in fcc metals by atomistic simulations. *Modelling and Simulation in Materials Science and Engineering*, 21(5):055013, jul 2013.

[21] Ju Li, Alfonso H.W. Ngan, and Peter Gumbsch. Atomistic modeling of mechanical behavior. *Acta Materialia*, 51(19):5711–5742, nov 2003.

[22] Bryan W Reed, Roger W Minich, Robert E Rudd, and Mukul Kumar. The structure of the cubic coincident site lattice rotation group. *Acta crystallographica. Section A, Foundations of crystallography*, 60(Pt 3):263–77, may 2004.

[23] G Gottstein and L S Shvindlerman. Structure of Grain Boundaries. In *Grain Boundary Migration in Metals: Thermodynamics, Kinetics, Applications*, chapter 2, pages pages 111–133. CRC Press LLC, Boca Raton, FL, 2010.

[24] Y. Pan, B.L. Adams, T. Olson, and N. Panayotou. Grain-boundary structure effects on intergranular stress corrosion cracking of alloy X-750. *Acta Materialia*, 44(12):4685–4695, dec 1996.

[25] D.G Brandon. The structure of high-angle grain boundaries. *Acta Metallurgica*, 14(11):1479–1484, 1966.

[26] David L. Olmsted, Stephen M. Foiles, and Elizabeth a. Holm. Survey of computed grain boundary properties in face-centered cubic metals: I. Grain boundary energy. *Acta Materialia*, 57(13):3694–3703, aug 2009.

[27] Dieter Wolf. Structure and Energy of Grain Boundaries. *Handbook of Materials Modelling*, pages 1953–1983, 2005.

[28] V. Randle. Grain boundary engineering: an overview after 25 years. *Materials Science and Technology*, 26(3):253–261, mar 2010.

[29] Valerie Randle. The coincidence site lattice and the 'sigma enigma'. *Materials Characterization*, 47(5):411–416, 2001.

[30] Valerie Randle. 'Special' boundaries and grain boundary plane engineering. *Scripta Materialia*, 54(6):1011–1015, 2006.

[31] M Shimada, H Kokawa, Z.J Wang, Y.S Sato, and I Karibe. Optimization of grain boundary character distribution for intergranular corrosion resistant 304 stainless steel by twin-induced grain boundary engineering. *Acta Materialia*, 50(9):2331–2341, may 2002.

[32] E.M. Lehockey, A.M. Brennenstuhl, and I. Thompson. On the relationship between grain boundary connectivity, coincident site lattice boundaries, and intergranular stress corrosion cracking. *Corrosion Science*, 46(10):2383–2404, oct 2004.

[33] Christopher a. Schuh, Mukul Kumar, and Wayne E. King. Analysis of grain boundary networks and their evolution during grain boundary engineering. *Acta Materialia*, 51(3):687–700, feb 2003.

[34] C. A. Schuh, M. Kumar, and W. E. King. Universal features of grain boundary networks in FCC materials. *Journal of Materials Science*, 40(4):847–852, 2005.

[35] Megan Frary and Christopher A. Schuh. Grain boundary networks: Scaling laws, preferred cluster structure, and their implications for grain boundary engineering. *Acta Materialia*, 53(16):4323–4335, 2005.

[36] David L. Olmsted, Elizabeth a. Holm, and Stephen M. Foiles. Survey of computed grain boundary properties in face-centered cubic metals-II: Grain boundary mobility. *Acta Materialia*, 57(13):3704–3713, aug 2009.

[37] M I Mendelev, C Deng, C a Schuh, and D J Srolovitz. Comparison of molecular dynamics simulation methods for the study of grain boundary migration. *Modelling and Simulation in Materials Science and Engineering*, 21(4):045017, jun 2013.

[38] M. Winning, G. Gottstein, and L.S. Shvindlerman. Migration of grain boundaries under the influence of an external shear stress. *Materials Science and Engineering: A*, 317(1-2):17–20, oct 2001.

[39] M. Winning, G. Gottstein, and L.S. Shvindlerman. On the mechanisms of grain boundary migration. *Acta Materialia*, 50(2):353–363, jan 2002.

[40] B. Schönfelder, G. Gottstein, and L.S. Shvindlerman. Comparative study of grain-boundary migration and grain-boundary self-diffusion of [001] twist-grain boundaries in copper by atomistic simulations. *Acta Materialia*, 53(6):1597–1609, apr 2005.

[41] D.A. Molodov, J. Swiderski, G. Gottstein, W. Lojkowski, and L.S. Shvindlerman. Effect of pressure on grain boundary migration in aluminium bicrystals. *Acta Metallurgica et Materialia*, 42(10):3397–3407, oct 1994.

[42] Kathleen C. Alexander and Christopher a. Schuh. Exploring grain boundary energy landscapes with the activation-relaxation technique. *Scripta Materialia*, 68(12):937–940, jun 2013.

[43] Kathleen C. Alexander and Christopher A. Schuh. Towards the reliable calculation of residence time for off-lattice kinetic Monte Carlo simulations. *Modelling and Simulation in Materials Science and Engineering*, Submitted, 2016.

[44] S. Plimpton. Fast Parallel Algorithms for Short - Range Molecular Dynamics. *Journal of Computational Physics*, 117(June 1994):1–19, 1995.

[45] GT Barkema and Normand Mousseau. The activation - relaxation technique: an efficient algorithm for sampling energy landscapes. *Computational materials science*, 20:285–292, 2001.

[46] H Jo'nsson, G Mills, and K.W. Jacobson. Nudged Elastic Band Method for Finding Minimum Energy Paths of Transitions. In *Classical and Quantum Dynamics in Condensed Phase Simulations*, chapter 16, pages 385–404. World Scientific, 1998.

[47] Graeme Henkelman; Hannes Jo'nsson. Improved tangent estimate in the nudged elastic band method for finding minimum energy paths and saddle points. *Journal of Chemical Physics*, 113(22):9978–9985, 2000.

[48] Daniel Sheppard, Rye Terrell, and Graeme Henkelman. Optimization methods for finding minimum energy paths. *The Journal of chemical physics*, 128(13):134106, apr 2008.

[49] Aiichiro Nakano. A space-time-ensemble parallel nudged elastic band algorithm for molecular kinetics simulation. *Computer Physics Communications*, 178(4):280–289, feb 2008.

[50] D. Rusin. Holes on a sphere, 1994.

[51] J F Nye. *Physical Properties of Crystals*, volume 607. 1957.

[52] Y. Mishin, M. Mehl, D. Papaconstantopoulos, a. Voter, and J. Kress. Structural stability and lattice defects in copper: Ab initio, tight-binding, and embedded-atom calculations. *Physical Review B*, 63(22):224106, may 2001.

[53] Rajendra R. Zope and Y. Mishin. Interatomic potentials for atomistic simulations of the Ti-Al system. (July):46, 2003.

[54] Guillaume Vérité, F. Willaime, and Chu Chun Fu. Anisotropy of the Vacancy Migration in Ti, Zr and Hf Hexagonal Close-Packed Metals from First Principles. *Solid State Phenomena*, 129(July 2015):75–81, 2007.

[55] Rodolfo Ariel Perez, Hideo Nakajima, and Fanny Dyment. Diffusion in α-Ti and Zr. *Materials Transactions*, 44(1):2–13, 2003.

[56] D. J. Oh and R. a. Johnson. Simple embedded atom method model for fec and hcp metals. *Journal of Materials Research*, 3(03):471–478, 1988.

[57] Graeme J. Ackland. Theoretical study of titanium surfaces and defects with a new many-body potential. *Philosophical Magazine A*, 66(6):917–932, 1992.

[58] De Grande, E.J. Savino, and N. Smetnianski. Point-defect anisotropic diffusion in strained HCP metals. *Physical Review B*, 35(12):6064–6073, 1987.

[59] C H Woo and C B So. The effect of stress on point defect diffusion in hcp metals and irradiation creep. *Philosophical Magazine A*, 80(6):1299–1318, 2000.

[60] X. W. Zhou, H. N G Wadley, R. a. Johnson, D. J. Larson, N. Tabat, A. Cerezo, a. K. Petford-Long, G. D W Smith, P. H. Clifton, R. L. Martens, and T. F. Kelly. Atomic scale structure of sputtered metal multilayers. *Acta Materialia*, 49(19):4005–4015, 2001.

[61] Abdulrafiu Tunde Raji, Sandro Scandolo, Riccardo Mazzarello, Schadrack Nsengiyumva, Margit Härting, and David Thomas Britton. Pseudopotential Study of Vacancies and Self-Interstitials in Hcp Titanium. *Philosophical Magazine*, 89(20):1629–1645, 2009.

[62] P. P. Tung and a. W. Sommer. Dislocation energetics in alpha titanium. *Metallurgical Transactions*, 1(4):947–953, 1970.

[63] W. Schilling. Self-interstitial atoms in metals. *Journal of Nuclear Materials*, 69-70:465–489, 1978.

[64] Timofey Frolov, David L Olmsted, Mark Asta, and Yuri Mishin. Structural phase transformations in metallic grain boundaries. *Nature communications*, 4(May):1899, 2013.